# Automated Error Assessment in Spherical Near-Field Antenna Measurements

by

Patrick Pelland, B. A. Sc.

A thesis submitted to the Faculty of Graduate and Postdoctoral Studies in partial fulfillment of the requirements for the degree of Master of Applied Science in Electrical and Computer Engineering

Ottawa-Carleton Institute for Electrical and Computer Engineering

School of Information Technology and Engineering

Faculty of Engineering

University of Ottawa

# Abstract

This thesis will focus on spherical near-field antenna measurements and the methods developed or modified for the work of this thesis to estimate the uncertainty in a particular far-field radiation pattern. We will discuss the need for error assessment in spherical near-field antenna measurements. A procedure will be proposed that, in an automated fashion, can be used to determine the overall uncertainty in the measured far-field radiation pattern of a particular antenna. This overall uncertainty will be the result of a combination of several known sources of error common to SNF measurements. This procedure will consist of several standard SNF measurements, some newly developed tests, and several stages of post-processing of the measured data. The automated procedure will be tested on four antennas of various operating frequencies and directivities to verify its functionality. Finally, total uncertainty data will be presented to the reader in several formats.

# Acknowledgements

I am very grateful for the guidance of my supervisors Dr. Derek McNamara and Dr. D. J. Janse van Rensburg. The research presented in this thesis would not have been possible without their tireless assistance.

I would also like to thank the Canadian Space Agency for supporting this work and for allowing use of its antenna test facilities in Ottawa.

# Publications

P. Pelland, D. J. Janse van Rensburg, D. A. McNamara, L. Shafai, S. Mishra, M. Gavrilovic, “Some Detailed Implementation Aspects of an Automated Error Assessment Scheme for Antenna Spherical Near-Field Measurements”, Proc. Antenna Measurement Techniques Association (AMTA) Annual Symp., 2010.

P.Pelland, J. Ethier, D.J. Janse van Rensburg, D. A. McNamara, L. Shafai, S. Mishra, "Towards Routine Automated Error Assessment in Antenna Spherical Near-Field Measurements", Proc. 4th European Conf. Antennas & Propagation (*EuCap 2010*), April 2010, Barcelona, Spain.

# Table of Contents

# List of Figures

# List of Tables

# CHAPTER 1: Introduction

## 1.1 PRELIMINARY REMARKS

Antennas will continue to be key components in the plethora of systems that rely on the launching and reception of electromagnetic waves. The measurement of the radiation pattern performance of antennas is essential both during their development and prior to their deployment. There is a large body of literature on antenna measurements [1,2,3,4]. Such measurements can be classified into far-field measurement techniques and near-field measurement techniques. It is most often the far-field radiation pattern (and quantities derived from it) of an antenna that are the actual goal. Far-field measurement techniques require the antenna under test (AUT) and the acquisition probe to be separated by a distance sufficiently large that the electromagnetic fields radiated by the AUT are locally plane at the location of the probe. Far-field measurement techniques provide the far-field radiation patterns directly. Near-field measurement techniques use an acquisition probe that can in principle be located at any distance from the AUT. Mathematical formulations (we will simply call these the near-field to far-field transformations) firmly grounded in electromagnetic theory are then used to predict the far-field radiation patterns from the measured data acquired in the near-field of the AUT. Near-field measurements have several advantages over direct far-field ones, but perhaps most important is that they can always be done indoors, a reality that brings real-estate cost and security benefits. Practical[1] near-field measurement techniques can in turn be divided into three classes: planar near-field testing, cylindrical near-field testing and spherical near-field testing. The classes are named according to the shape of the surface surrounding the AUT over which the acquisition probe samples the data. This thesis is concerned with the spherical near-field method only.

[1] We use the word "practical" since in theory one can use a surface of any shape surrounding the AUT. This fact appears to be rediscovered by someone ever few years. However, it is difficult to design data acquisition scanners for arbitrary surfaces! Also, very computationally efficient near-field to far-field transformations (a must in practice) are only available for the three surfaces mentioned.

## 1.2 EXISTING SPHERICAL NEAR-FIELD ANTENNA MEASUREMENT ERROR QUANTIFICATION

No measurement technique is perfect. Thus when we perform such measurements we would like to know what the measurement uncertainties are. We of course can never determine what the actual errors are. If we did then we could simply adjust the measured result accordingly and they would be error free. Instead we identify the sources of error in a particular measurement techniques (these are the so-called "error terms" that will dominate much of the discussion of this thesis) and then find ways to estimate the uncertainty contribution due to each such error term. Nevertheless, in antenna engineering practice people loosely talk about "estimating the error". But engineers know what is meant. In summary, we understand that in the strict sense the term “measurement error” implies an undesired quantity that is quantified and can subsequently be corrected for. The term “measurement uncertainty” implies an undesired quantity that is estimated or bounded, but cannot be corrected for. In this thesis, as in practice, the term “measurement error” is often used when referring to either of these cases.

Errors in spherical near-field antenna measurements have been studied [5-11] for the last fifteen years. However, there has not been a scheme available through which SNF measurement uncertainty can be estimated in a routine fashion. This thesis therefore develops a new measurement process that permits an assessment of spherical near-field (SNF) measurement errors based on a set of tests that can be done as part of any SNF measurement. The purpose is to achieve a test system that can, in an automated fashion, derive error bars for a measured radiation pattern and related quantities.

## 1.3 OVERVIEW OF THE THESIS

Chapter 2 provides a brief overview of existing work on error assessment in SNF antenna measurements. This literature review introduces the type of work being done toward fully understanding the potential sources of error in SNF measurements. A proposed 18-term error budget, meant to fully quantify all sources of error in SNF measurements, is

outlined, and a fairly detailed description of each error term is given. Much of this information comes from the existing literature, but here we clarify several issues, adapt certain error terms so that they become more directly applicable to SNF measurements (since much of the earlier error assessment work has been for planar near-field measurements), supply missing pieces of information that have been obtained through the actual work done for this thesis, and determine which existing tests for existing tests for the evaluation of particular individual error terms can be made use of (since this thesis places an emphasis on the automation of SNF error assessment, and so pre-existing tests that support this goal are exploited).

Chapter 3 contains all of the technical details required to implement an automated error assessment process for any SNF environment. A list of definitions, and some terminology crucial to understanding errors in SNF measurements as treated in this thesis, is provided. Implementation details are given for each contributing error term, based on the analysis in Chapter 2. This clarifies exactly how a particular error term is evaluated and which measurements it makes use of for this evaluation. A set of measurements is proposed that is sufficient to extract all uncertainty information for the eighteen error terms presented in Chapter 2. We discuss the order in which these data sets should be acquired to minimize the overall time to complete an error assessment while still providing reasonable estimates of the errors in the quantities being measured. This order is especially important to allow resumption of data set acquisition should any single step prove to be temporarily problematic. We describe the relative importance of the error assessment data sets, which ones need to be acquired only some of the time, which are AUT-dependent, and so on. Finally the four different antenna types that are used to demonstrate the utility of the error assessment developed here are identified.

Chapter 4 exercises the automated error assessment procedure on each of the identified antenna types. These antennas have been selected so as to cover different frequency ranges and pattern types (eg. high gain pencil beam slotted waveguide array; medium gain horn antenna; low gain broad beam microstrip patch antenna, shaped beam ringed horn antenna). The experimental results for these antenna types is discussed for each of

the eighteen terms in turn, thereby providing increased insight into the significance of each such term. The implementation of such automated error assessment through the development of scripting code is also described.

Finally, some general conclusions are reached in Chapter 5, and the research reported herein put into perspective.

## 1.4 REFERENCES FOR CHAPTER 1


[1] E.S.Gillespie. "Measurement of Antenna Radiation Characteristics on Far-Field Ranges", Chap.32 in : Y.T.Lo & S.W.Lee (Edits.), *Antenna Handbook,* Vol. 4 (Van Nostrand Reinhold, 1993).

[2] J.Appel-Hansen, "Near-Field Far-Field Antenna Measurements", Chap.33 in : Y.T.Lo & S.W.Lee (Edits.), *Antenna Handbook,* Vol. 4 (Van Nostrand Reinhold, 1993).

[3] J.Appel-Hansen, E.S.Gillespie, T.G.Hickman & J.D.Dysion, "Antenna Measurements", Chap. 8 in : A.W.Rudge, K.Milne, A.D.Olver & P.Knight (Edits.), *The Handbook of Antenna Design,* Vol. 2 (Peter Peregrinus Ltd., 1986).

[4] D.Slater, *Near-Field Antenna Measurements* (Artech House Inc., 1991).

[5] D.J Janse van Rensburg, S. Mishra, G. Seguin, "Simulation of Errors in Near-Field Facilities", Proc. Antenna Measurement Techniques Association (*AMTA*) Annual Symp., pp. 336 – 340, 1995.

[6] A. Newell, G. Hindman, "Quantifying the Effect of Position Errors in Spherical Near-Field Measurements", Proc. Antenna Measurement Techniques Association (*AMTA*) Annual Symp., pp. 145 – 149, 1998.

[7] A. Newell, G. Hindman, "The Effect of Measurement Geometry on Alignment Errors in Spherical Near-Field Measurements", Proc. Antenna Measurement Techniques Association (*AMTA*) Annual Symp., pp. 274 – 279, 1999.

[8] D. Hess, "An Expanded Approach to Spherical Near-Field Uncertainty Analysis", Proc. Antenna Measurement Techniques Association (*AMTA*) Annual Symp., 2002.

[9] A. Newell, "Estimating the Uncertainties due to Position Errors in Spherical Near-Field Measurements", Proc. Antenna Measurement Techniques Association (*AMTA*) Annual Symp., 2003.

[10] M. Francis, R. Wittmann, "Uncertainty Analysis for Spherical Near-Field Measurements", Proc. Antenna Measurement Techniques Association (*AMTA*) Annual Symp., 2003.

[11] G. Hindman, A. Newell, "Simplified Spherical Near-Field Accuracy Assessment", Proc. Antenna Measurement Techniques Association (*AMTA*) Annual Symp., 2006.

# CHAPTER 2: Review of Error Assessment in Antenna Measurements

## 2.1 INTRODUCTORY REMARKS

This chapter will provide a brief overview of existing antenna measurement techniques and discuss the concept of error assessment in spherical near-field (SNF) antenna measurements. In Section 2.2 review existing antenna measurement techniques, with an emphasis on SNF antenna measurements. Next, in Section 2.3, a brief discussion of existing research into error assessment in SNF antenna measurements will be presented. This literature review will provide the reader with an introduction to the type of work being done toward fully understanding the potential sources of error in SNF measurements. A proposed 18-term error budget, meant to fully quantify all sources of error in SNF measurements, will then be outlined in Section 2.4. In Section 2.5 the reader will find a detailed description of each error term from the proposed budget, in turn. Much of the information in Section 2.5 comes from a thorough literature review of error assessment in antenna measurements, while the remainder is based on the experience gained by the author while engaged in the work of this thesis. This section will also include the methods used by various other authors to evaluate a particular error term in order to determine if it will be possible to make use of any existing evaluation techniques. Since this thesis places an emphasis on the automation of SNF error assessment, pre-existing tests that support this goal will be favoured. Finally, some concluding remarks will be presented in Section 2.6.

## 2.2 ANTENNA MEASUREMENT TECHNIQUES

As the design of microwave antennas leads to more advanced, complex radiating structures, a need for more and more precise measurements of the antenna's radiation characteristics arises. Furthermore, as electromagnetic simulation software packages become more powerful and accurate at calculating the radiation characteristics of a particular antenna, the systems used to verify the functionality of these antennas must similarly evolve. This need has been most apparent within the space industry, where very

tight specifications must be met in order to obtain appropriate functionality in such an environment [1, p.1]. We next outline some existing antenna measurement techniques, along with some terminology specific to SNF antenna measurements.

### 2.2.1 Far-Field Antenna Measurements

The radiation from a transmitting antenna can be divided in to three regions, as shown in Figure 2-1. First, in the reactive near-field region, the energy decays very rapidly with distance. In the second region, the radiative near-field region, the average energy density remains fairly constant at varying distances from the antenna, although some localized energy fluctuations are present [2]. The angular dependence of the electromagnetic field radiated from a transmitting antenna in the first two regions changes gradually with distance. The boundary between the reactive near-field region and the radiative near-field region is not distinct and the change from one region to another is gradual. The boundary between these two regions is typically within one to three wavelengths away from the transmitting antenna. However, at large distances from the antenna, known as the antenna's "far-field" region, the angular distribution of the energy does not vary with distance and the power level decays according to the inverse square law with respect to distance [2]. In other words, the radiated far-field of a particular antenna is a locally plane wave propagating radially outward from the antenna. The performance of an antenna in the radiating far-field region is of great importance.

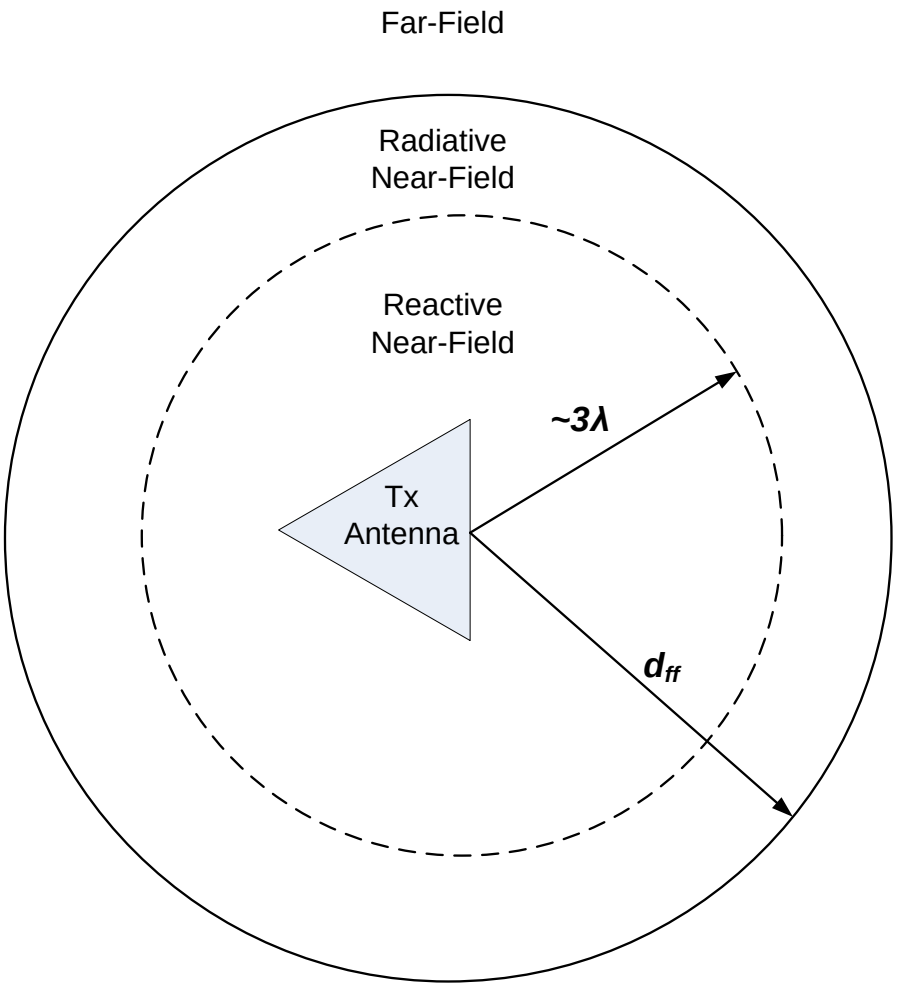


**Figure 2-1: Diagram Outlining the Three Radiation Regions for a Transmitting Antenna**

The far-field antenna range was the original antenna measurement technique. This measurement technique consists of placing the antenna under test (AUT) at a distance far away from a probe antenna, such that the probe will receive electromagnetic energy in the AUT's far-field region. This ample AUT to probe separation ensures that the plane wave condition is met before acquiring measurement data. The boundary separating the radiative near-field region from the far-field region is typically considered to be

$$d_{FF} = \frac{2D^2}{\lambda} \tag{2.2-1}$$

where D is the largest dimension of the AUT's radiating aperture [3]. This distance is also known as the "minimum far-field distance", as shown in Figure 2-1.

Since the dimensions and operating frequency of a particular antenna determine the minimum far-field distance, $d_{FF}$, one can immediately understand a fundamental difficulty in using far-field measurements universally. For example, a parabolic reflector with a diameter of 1 m operating at 5 GHz requires a minimum measurement distance of 33 m. By increasing the reflector size to 1.5 m, the minimum far-field distance becomes 75 m. Because of the large distances required to characterize many antennas, the first far-field measurement systems were installed outdoors.

These outdoor ranges are highly susceptible to varying weather conditions, including heavy rain, snow, wind, wildlife intrusions and more. These natural phenomena can negatively affect the measured pattern of a particular antenna. Additionally, security can be a major concern for these types of systems since a large portion of equipment, hardware and cables must be installed away from a primary indoor facility. Finally, the cost of land required to install and maintain a conventional outdoor far-field range tends to be much higher than newer indoor ranges, as will be discussed shortly.

Far-field ranges are also implemented in standard anechoic chambers of varying size, although one must understand the limitations in antenna size and test frequency before installing such a range. Finally, another type of far-field range is what is known as an indoor compact range. A compact range makes use of a large parabolic reflector used to convert incoming electromagnetic waves into plane waves, thereby reducing the required measurement distance to obtain far-field patterns. While these compact ranges offer excellent performance, the facility cost tends to be very high due to the complex nature of the range and cost of the reflector. Since conventional far-field measurement techniques provide so many limitations, near-field antenna measurement techniques have become commonplace, offering increased accuracy, lower costs and smaller facilities that can more readily handle larger antennas with higher operating frequencies.

### 2.2.2 Near-Field Antenna Measurements

In the 1960's D. M. Kerns of the National Bureau of Standards in the United States published work toward developing what is known as scattering matrix theory [4]. This is a greatly generalized version of the scattering matrix theory used in multiport networks. His work comprises the theoretical basis for near-field antenna measurements. In essence, scattering matrix theory allows one to represent the field transmitted by a particular AUT in terms of a spectrum of waves. These wave spectra can take many forms:

- plane waves, used in planar near-field (PNF) measurements
- cylindrical waves/modes for cylindrical near-field (CNF) measurements
- spherical waves/modes for spherical near-field (SNF) measurements.

Using scattering matrix theory allows one to measure the radiation of an AUT in the near-field region and perform a transformation to obtain far-field patterns. Measurements are completed on a near-field scan surface, with the geometry of the scan surface depending on the type of near-field system in use. After many years of development and industry evaluation, near-field testing has become the preferred approach for characterizing antennas. These systems are capable of measuring sidelobes as low as 50 dB down from the pattern peak and can provide sub-milliradian alignment accuracies [2]. However, the different types of near-field systems also have individual weaknesses and strengths, as will be outlined below. It should also be noted that near-field antenna measurement schemes make the assumption that multiple reflections and reactive coupling between the probe and AUT are small enough to neglect [5]. While this is not rigorously the case in practice, some methods of estimating and compensating for the effects of multiple reflections on far-field patterns exist.

#### *A. Planar Near-Field Measurements*

PNF measurements were the first of the near-field measurement geometries to become commonplace in the industry. In a PNF scan, the field measuring probe will typically measure field values at specified positions on an XY grid, while the AUT is placed at a

fixed measurement distance from the probe along the z-axis. A sketch of this measurement geometry, along with a typical probe scan pattern is shown in Figure 2-2. In this figure, the probe measures the field at several points along a line in Y, a vertical cut, before stepping to the next position in X and repeating the vertical cut. Once vertical cuts have been completed for all positions in X, the full set of near-field data can be transformed to the far-field using plane wave expansion theory. This geometry has the advantage of keeping the AUT stationary throughout the scan, which can be beneficial in some circumstances.

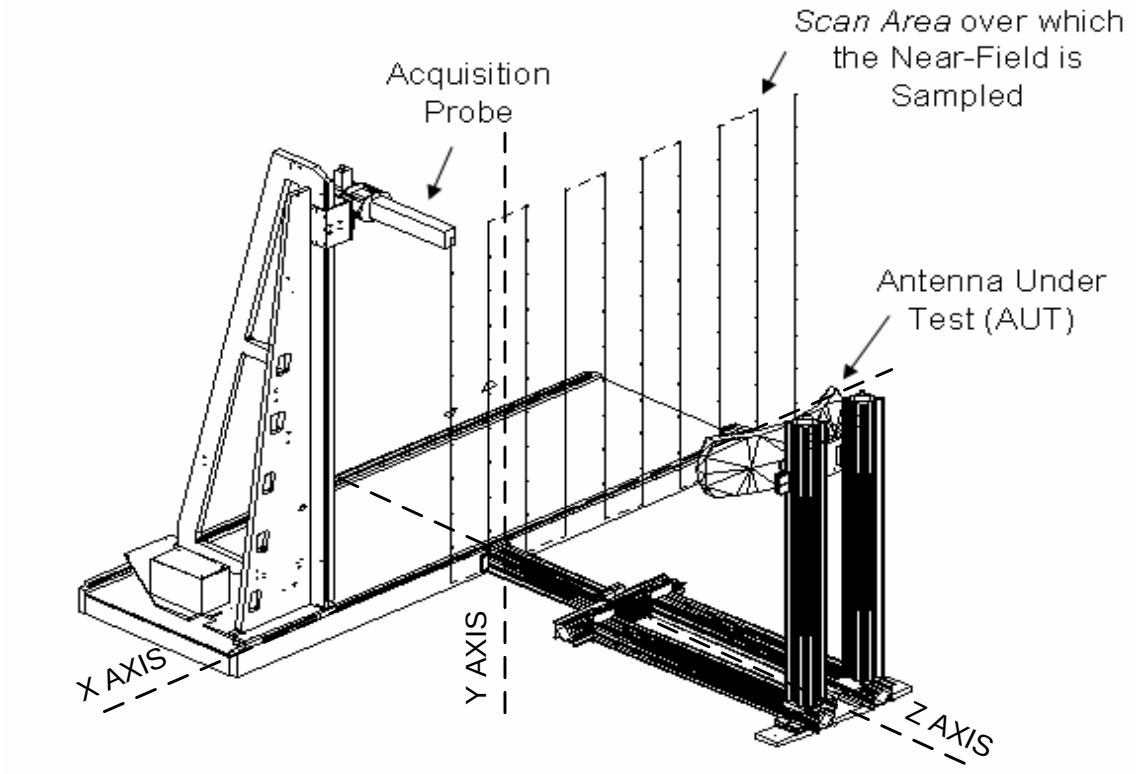


**Figure 2-2: Typical Planar Near-Field Measurement System (Adapted from a Diagram Courtesy of Nearfield Systems Inc.)**

A fundamental requirement for rigorously applying scattering matrix theory is that a closed measurement surface be used to enclose all radiating elements of the AUT. In a PNF measurement, the term "closed measurement surface" implies that the scan plane be infinitely long in both X and Y. However, since this is clearly not practical in a measurement system, one must use a finite scan plane sufficiently large to capture most of the AUT's radiation. Since low gain antennas have broad radiation patterns the PNF

measurement system is inadequate at capturing most of the radiated power for such AUT's. Because of this, PNF systems are best suited for antennas with a directivity of 15 dBi of greater. The fast measurement speed and low system cost make the PNF system an appropriate option for a wide range of problems, provided the AUT has sufficiently high directivity.

### *B. Cylindrical Near-Field Measurements*

The next type of near-field system to be discussed is the CNF system. Similar to a PNF measurement, the CNF range allows fields to be measured over an open measurement surface in the AUT's near-field region. Figure 2-3 shows a typical CNF measurement geometry and cylindrical scan surface. The AUT is mounted on top of an azimuth-axis rotator at the center of this scan surface and the probe is translated along the Y-axis for a full vertical cut. Next, the AUT is rotated in azimuth by a specified amount and the probe performs a second vertical cut. Once vertical cuts have been completed for all azimuth positions, cylindrical mode theory can be used to transform the near-field grid data to the far-field. Again, since an open measurement window was used, only antennas with very little energy radiating in the regions not enclosed by the measurement surface should be considered for CNF scans.

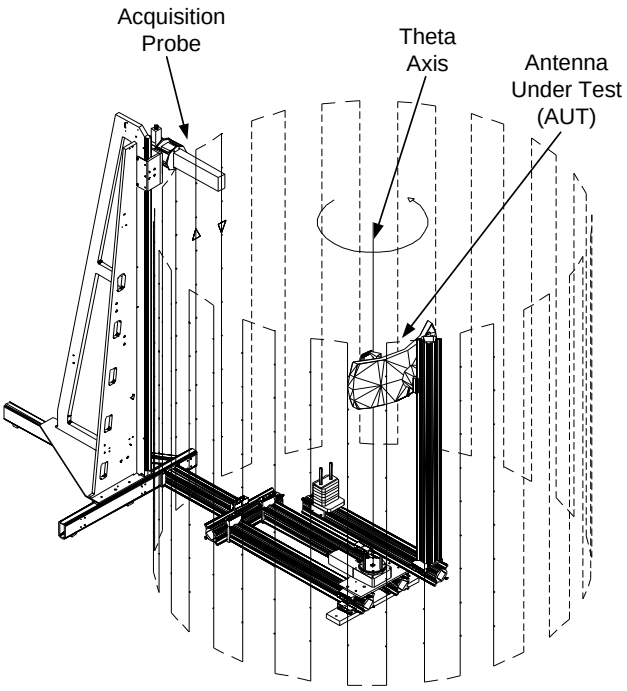


**Figure 2-3: Typical Cylindrical Near-Field Measurement System (Adapted from a Diagram Courtesy of Nearfield Systems Inc.)**

### *C. Spherical Near-Field Measurements*

The SNF geometry is of special interest, since this thesis is primarily involved in error analysis for this type of near-field system. One of the fundamental requirements for an SNF system is that data be acquired on a spherical surface enclosing the AUT. A typical SNF system is shown in Figure 2-4. The AUT can be seen at the origin of the measurement sphere, mounted on two separate positioners. Together, these positioners must allow the AUT to rotate in such a way that the probe can record field values over the entire measurement sphere. For the measurement geometry depicted in Figure 2-4, the AUT will first perform a complete azimuth cut. In other words, the AUT, along with the entire structure that the AUT is mounted on, will rotate a full 360˚ and return to its starting position. Next, the AUT will rotate a specified amount in $\phi$ and repeat the 360˚ azimuth cut. Once azimuth cuts have been completed for all $\phi$ positions, spherical mode theory can be used to transform the spherical near-field measured data to a far-field pattern.

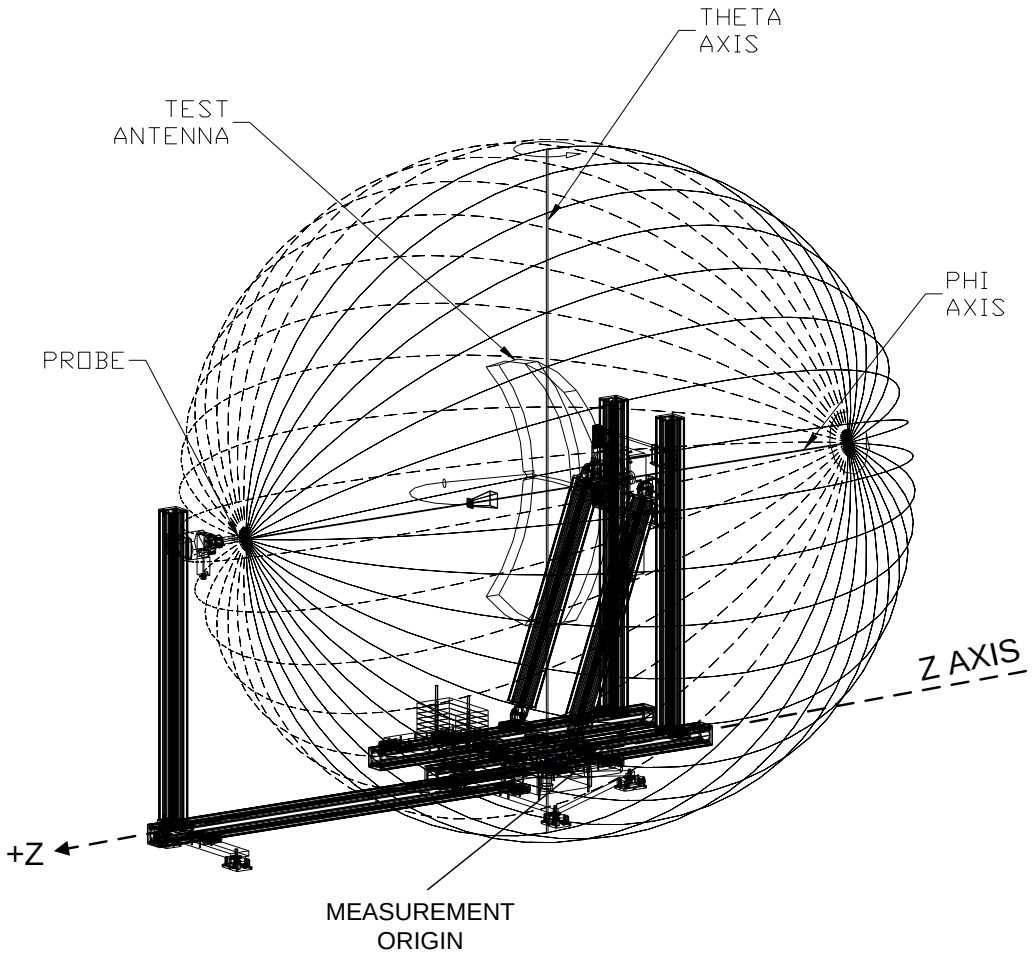


**Figure 2-4: Typical Spherical Near-Field Measurement System (Adapted from a Diagram Courtesy of Nearfield Systems Inc.)**

This type of near-field system has several advantages over conventional far-field, PNF and CNF systems. First, since a closed scan surface is used in a SNF measurement, the truncation approximations made for CNF and PNF measurements are no longer present. Because of this, the SNF system can more universally meet different types of antenna measurement requirements. While there are SNF systems that employ open measurement windows for various reasons, these are outside of the scope of this work. These systems provide the best sidelobe performance since fields are measured in all directions, with the exception of the mounting structure blocking the AUT's backward radiation.

### 2.2.3 Spherical Near-Field Antenna Measurement Notation

***A. 180-Phi Data Set***

This refers to the resulting data set acquired using a SNF measurement where the AUT rotates 360˚ in $\theta$ but only 180˚ in $\phi$. This means that the AUT will illuminate all four walls of the chamber during the measurement. For a 180-Phi measurement acquired with M sampling points in $\theta$ and N sampling points in $\phi$, data will be measured at the following points:

$$\theta_m = -180° + (m-1)\left(\frac{360}{M-1}\right); \quad m = 1,2,...,M \tag{2.2-2}$$

$$\phi_n = (n-1)\left(\frac{180}{N-1}\right); \quad n = 1,2,..., N \tag{2.2-3}$$

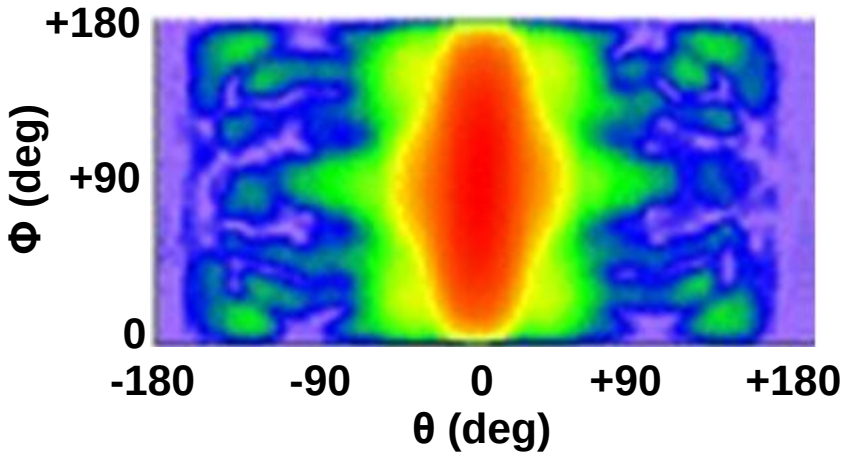


**Figure 2-5: Example of a 180-Phi SNF Acquisition (After [6])**

Figure 2-5 shows a near-field amplitude distribution for an arbitrary measurement using the 180-Phi sampling strategy, where the $\theta$-axis rotates a full 360˚.

***B. 360-Phi Data Set***

This refers to the resulting data set acquired using a SNF measurement where the AUT only rotates 180˚ in $\theta$ and 360˚ in $\phi$. This now means that the AUT will no longer "see" one of the chamber's walls (the wall illuminated by the AUT at $\theta$ = 180˚). For a 360-Phi

measurement acquired with M sampling points in $\theta$ and N sampling points in $\phi$, data will be measured at the following points:

$$\theta_m = (m-1)\left(\frac{180}{M-1}\right); \quad m = 1,2,...,M \tag{2.2-4}$$

$$\phi_n = (n-1)\left(\frac{360}{N-1}\right); \quad n = 1,2,...,N \tag{2.2-5}$$

where $\theta_m$ and $\phi_n$ do not correspond to the same sampling points as in (2.2-2) and (2.2-3). Figure 2-6 shows the near-field amplitude distribution acquired using the 360-Phi sampling strategy, where the $\phi$-axis now rotates 360˚.

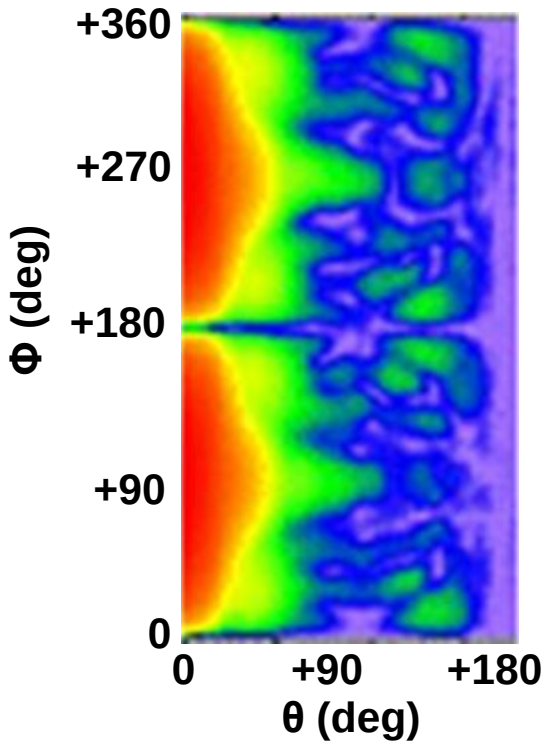


**Figure 2-6: Example of a 360-Phi SNF Acquisition (After [6])**

### *C. Redundant Theta/Phi Data Set*

This refers to the resulting data set acquired using a SNF measurement where the AUT rotates a full 360˚ in both θ and $\phi$. The AUT will illuminate all 4 walls of the chamber during the course of the scan. Since both axes rotate a full 360˚, two complete AUT data

subsets are contained within the redundant data set. For a redundant measurement acquired with M sampling points in $\theta$ and N sampling points in $\phi$, data will be measured at the following points:

$$\theta_m = -180° + (m-1)\left(\frac{360}{M-1}\right); \quad m = 1,2,...,M \tag{2.2-6}$$

$$\phi_n = (n-1)\left(\frac{360}{N-1}\right); \quad n = 1,2,...,N \tag{2.2-7}$$

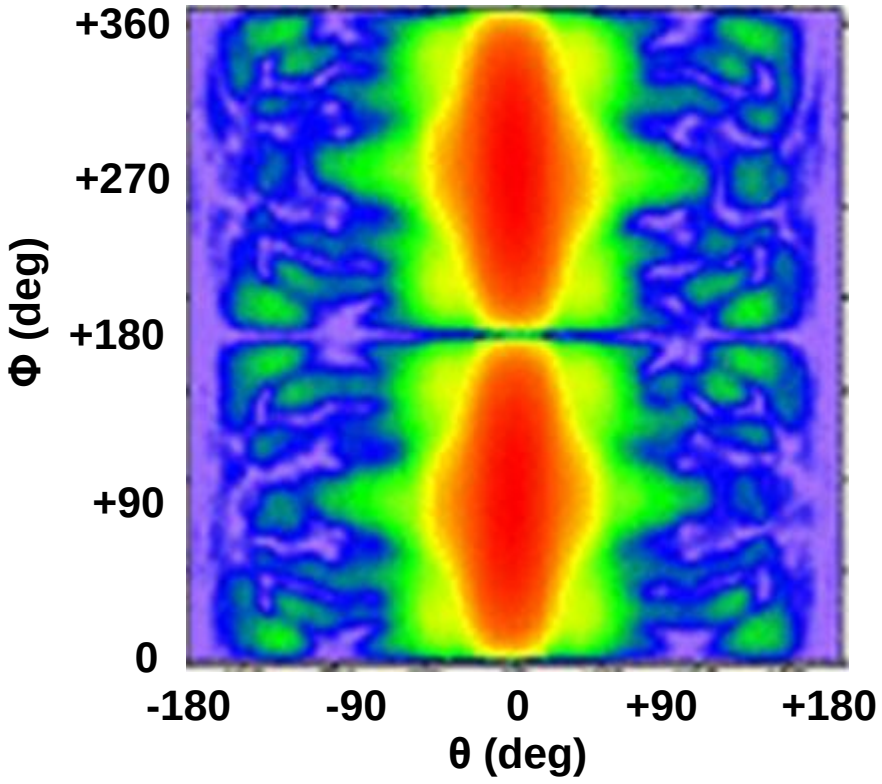


**Figure 2-7: Example of a Redundant Theta/Phi SNF Acquisition (After [6])**

By averaging the two subsets (180-Phi and 360-Phi), one may acquire what is known as a "redundant theta/phi" data set. Making use of these three different sampling strategies will aid the automated error assessment process, as will be seen in the handling of several error terms. Figure 2-7 shows that near-field data is, in fact, acquired redundantly when using the redundant theta/phi sampling strategy.

**Table 2-1: Summary of Spherical Near-Field Sampling Strategies**

| Terminology | Description |
|---|---|
| 180-phi Scan | Measurement sphere acquired with AUT rotation of $0^\circ \leq \phi \leq 180^\circ$, $-180^\circ \leq \theta \leq 180^\circ$. |
| 360-Phi Scan | Measurement sphere acquired with AUT rotation of $0^\circ \leq \phi \leq 360^\circ$, $0^\circ \leq \theta \leq 180^\circ$. |
| Redundant Scan | Measurement sphere acquired with AUT rotation of $0^\circ \leq \phi \leq 360^\circ$, $-180^\circ \leq \theta \leq 180^\circ$. This will produce two complete AUT data sets, which can be averaged to produce a single, redundant radiation pattern. |

## 2.3 ERROR ASSESSMENT IN ANTENNA MEASUREMENTS

A number of papers have been written on the numerous error contributions in antenna measurements in general. Furthermore, there has been a considerable amount of published material focusing on error assessment in near-field measurements in particular. This section will deal primarily with error assessment work performed using SNF measurement systems since this is the primary focus of this work. This section is by no means a complete literature review on error assessment in spherical near-field measurements, but contains the lasting work completed in the last number of years and which forms the basis of the work of the present thesis.

### 2.3.1 Existing Spherical Near-Field Error Assessment Literature

To start, reference [7] discusses the simulation of mechanical and electrical errors associated with SNF measurements. The authors have included a total of ten terms in their error assessment budget. Provision for chamber reflections and equipment-related uncertainty can be added to the analysis, but requires experimental rather than simulation data. The procedures and software developed there may be easily converted for use in other near-field measurement systems. Reference [8] discusses how one can estimate the error associated with several antenna parameters. The authors of [8] utilize only six alignment error quantities, as opposed to the ten error terms introduced in [7].

Next, a discussion on the alignment of spherical near-field rotators using electrical measurements is discussed in [9]. It shows how it is impractical to use mirrors for AUT alignment in an SNF setup. An alternative is to perform repeated measurements of the AUT and use these results to improve alignment with each new measurement. In the end, a series of electrical tests to align and check the alignment of a spherical near-field rotator was successfully implemented and tested.

Reference [10] presents a discussion of a discrepancy in the literature where two papers showed conflicting conclusions regarding error in SNF measurement. The conclusion was that theta-scans that pass through the poles (which use 180–Phi sampling strategies) produce phase errors in a plus and minus sense that tend to cancel in the on-axis direction. On the other hand, theta-scans that do not pass through the poles (360-Phi scan) do not have this cancelling effect. This means that measurements acquired using the 180-Phi sampling strategy will tend to have lower on-axis measurement uncertainty than the 360-Phi sampling strategy. Hence, the sampling strategy of a measurement is critical in reducing errors in SNF measurements.

Next, an exhaustive error budget is proposed in [11], where an attempt is made to mimic the 18-term error budget associated with PNF measurements as originally proposed by the National Institute of Standards Technology (NIST) in the USA. The authors of [11]

propose a 30-term error budget principally to obtain a qualitative understanding of the entire problem, and so do not provide quantitative verification through measurement or simulation. However, they attempt to convert the conventional NIST 18-term error budget originally developed for planar measurements to something more applicable to SNF measurements. Reference [12] similarly discusses a method to characterize the performance of SNF chambers, and establishes an 18-term error budget along the same lines as the NIST 18-term budget. Unlike [11], the errors can actually be determined using the tests proposed in [12]. A 20-term error budget is proposed in [13]. The approach is theoretical, its authors intending it to be of a "foundational" nature that future authors could use as a basis. The same authors consider more specific estimates of measurement error in the near-field, and their effects on the far-field, in a follow up paper [14].

Reference [15] concentrates on the measurement uncertainties due to probe theta/phi position errors. The author points out that previous to [15] there was a reliance on the results of PNF uncertainty guidelines to predict SNF uncertainties, in the sense that minimum probe position errors are specified to keep error quantities below acceptable thresholds. Hence, he derives more specific expressions (algorithms if you will) for these probe position errors. He uses a simulation approach, quite similar to [7], and quotes measurement uncertainties for some standard antennas.

Reference [16] discusses the use of self-comparison testing in SNF measurements. It uses an over-determined set of measurements which helps to qualify various near-field related sources of error including positioner alignment, chamber reflections and errors introduced by truncation. An eight-step process that identifies errors and repeats the measurement to correct for these errors is used.

A theoretical examination at the effects of reflections in SNF chambers is considered in [17], which proposes measuring the near-field over two spheres, separated by a quarter-wavelength. Reference [18] discusses the use of two sets of measurements from two different chambers, and compares the uncertainty to validate conventional assumptions.

The estimation of measurement error due to the imperfect polarization properties of probes is discussed in [19] for all three conventional types of near-field measurements, including SNF. Finally, [6] describes an algorithm that can be used to assess SNF chamber performance.

### 2.3.2 Automated Error Assessment in Spherical Near-Field Measurements

While error analysis in spherical near-field antenna measurements has been an ongoing area of research for quite some time, it remains a very tedious process for chamber operators. Fully quantifying all sources of error in a particular chamber requires a great deal of time, precision and technical knowledge about the various sources of error. Because of this, there is seldom any discussion regarding the uncertainty in a particular measurement when quoting far-field pattern data.

Therefore, the primary goal for this thesis is to provide all of the details necessary to implement an automated error assessment procedure for any SNF chamber. This includes the automatic acquisition of all required near-field measurements, as well as all the post-processing required to fully quantify all error terms. The purpose is to achieve a test system that would, in an automated fashion, derive error bars for a measured radiation pattern. Ideally, this automated process will minimize chamber occupancy while providing reasonable engineering estimates of the errors in the quantities being measured. Additionally, this process should be formulated in a way that it can eventually be adapted to other antenna measurement range geometries such as planar near-field, cylindrical near-field and far-field ranges.

## 2.4 SOURCES OF ERROR IN SPHERICAL NEAR-FIELD MEASUREMENTS

After performing an exhaustive review of the existing SNF error assessment literature, the NIST 18-term error budget analysed in [12] was chosen as the best starting point toward developing the automated process. It is the author's opinion that the NIST 18-term budget quantifies all significant sources of error in SNF antenna measurements and supersedes the other error assessment budgets studied. While this budget was originally developed for use in planar near-field measurements, it can be easily adapted to spherical near-field measurements with some changes, as will be discussed next.

First, one should realize that the effects of data truncation (NIST budget error term #9) will not be present for most SNF measurements. This error term deals directly with the errors caused by the finite scan plane used in the planar near-field measurement. Since SNF measurements typically use a closed sphere, the effects of truncation are eliminated. However, if one wishes to truncate the measurement sphere to save time, error term #9 should reflect this. Because of this, data truncation will not be removed from the proposed budget, but will be listed as "not applicable" for most cases in later chapters of this thesis.

Next, error terms #10 & #11 should be updated for use in a SNF error assessment budget. When the NIST budget was developed for planar measurements, these error terms dealt with imperfections in the planar scan surface. Namely, error term #10 dealt with XY-position errors, while error term #11 handled Z-position errors. The authors of [12] lump error terms #10 & #11 into a single term called *"*XYZ Position Errors*"*. However, the process used in [12] to estimate the uncertainty due to these error terms is a poor adaptation from the planar test case. Since it compares measurements acquired using different scanning geometries, this method will include various other sources of error, including room scattering, which tends to swamp the errors associated with error terms #10 & #11. In order to increase the applicability to SNF measurements, these error terms must account for imperfections in the measurement sphere rather than imperfects in the planar scan surface, as is the case for PNF measurements. As an alternative, error term

#10 has been renamed to “Sphere Radius Errors” and error term #11 has been renamed to “Sphere $\theta/\phi$ Errors”. The details of these error terms will be outlined in Sections 2.5.10 and 2.5.11.

Finally, it should be noted that when using the modified NIST 18-term budget, one will find that some sources of error will have different levels of contribution to the overall measurement uncertainty than they do in the planar case. For example, in planar measurements, one finds the effects of the probe’s pattern to be quite significant away from the main beam of the AUT’s pattern. However, since the AUT is always illuminated by the probe pattern’s peak in SNF measurements, the effects of the probe’s pattern on the resulting AUT pattern are almost negligible. As another example, system phase errors are predominantly caused by the flexing of cables in planar measurements, while imperfections in the SNF system’s multiple rotary joints tend to dominate this error term. Table 2-2 gives a summary of the error terms in the modified NIST 18-term error budget used in the work of this thesis.

**Table 2-2: Modified NIST 18-Term Error Budget for SNF Measurements**

| # | Error Term | Description |
|---|---|---|
| 1 | Probe Relative Pattern | Errors introduced by imperfections in probe correction model. |
| 2 | Probe Polarization | Errors introduced by non-zero probe cross-polarization levels. |
| 3 | Probe Gain | Measured AUT gain uncertainty due to probe gain uncertainty. |
| 4 | Probe Alignment | Measurement errors introduced by imperfect probe alignment. |
| 5 | Normalization Constant | Measured gain uncertainty introduced during the replacement of the AUT with the SGH for gain measurements. |
| 6 | AUT/SGH Impedance Mismatch | Measured gain uncertainty introduced by differences in SGH/AUT impedance mismatches. |
| 7 | AUT Alignment | Uncertainty introduced due to imperfect AUT alignment. |
| 8 | Data Point Spacing | Errors introduced due to the finite number of sampling points used in the NF measurement. |
| 9 | Data Truncation | Errors introduced through the use of an open measurement region. |
| 10 | Sphere Radius Errors | Measurement errors introduced by uncertainty in the measurement sphere radius. |
| 11 | Sphere $\theta/\phi$ Errors | Measurement errors introduced by the non-orthogonality and non-intersection errors of the measurement $\theta$ and $\phi$ axes. |
| 12 | Higher Order Coupling | Errors introduced by the reactive coupling and multiple reflections between the probe and AUT. |
| 13 | Receiver Amplitude Non-Linearity | Errors introduced by the non-linear amplitude response of the receiver. |
| 14 | System Phase Errors | Errors caused by the unwanted variable electrical path length due to rotary joint imperfections. |
| 15 | Receiver Dynamic Range | Errors caused by the receiver's limited dynamic range. |
| 16 | Room Scattering | Errors introduced by reflections in a non-ideal scattering environment. |
| 17 | Cable Leakage | Errors introduced by unwanted radiation from cables. |
| 18 | Repeatability and Random Errors | Errors associated with system repeatability. |

## 2.5 DETAILED DESCRIPTIONS OF THE ERROR TERMS

In this section, all eighteen error terms in the modified NIST 18-term error budget as presented in Table 2-2 will be studied in detail. A brief description of each source of error will be provided, along with some suggestions on how to determine the effects of that particular source of error on the resulting far-field pattern.

### 2.5.1 Error Term #1: Probe Relative Pattern

In near-field measurements, it is necessary to compensate for the effects of the probe's pattern on the final AUT radiation pattern. In an ideal sense, one would like to measure the near-field quantities at an infinitesimal point in space – this is of course impossible. The best one can do is have a measuring probe where its pattern is known (recall that pattern refers to both transmit and receive) and a probe compensation technique is used to approximately determine the AUT field at a point in space.

In SNF measurements, the probe pattern correction is less important than for other near-field measurement setups. The reasoning for this is that in SNF measurements only the region illuminated by the AUT that is in common with the SNF probe is of concern. Since the probe's amplitude pattern tends to be quite constant across the region illuminated by the AUT, one finds that probe correction has a very minimal effect on normalized AUT patterns for SNF measurements. Figure 2-8 illustrates the concept of uncertainty in the probe relative pattern for SNF measurements. It shows that while there is noticeable amplitude taper in the probe's radiation pattern, the region illuminating the AUT is quite flat. The black, curved line represents the nominal amplitude pattern illuminating the AUT, while the irregular red line represents the same probe pattern with errors introduced to it. Since the probe correction process uses the nominal pattern for correction, the probe pattern error will directly affect the AUT pattern amplitude. The arrows between the actual probe pattern amplitude and the nominal probe pattern amplitude represent the amplitude error in the probe's pattern for this particular example. When purchasing a probe for use in SNF systems, one will typically be provided with nominal probe pattern data, but no measure of the pattern's uncertainty.

Nevertheless, it is important to measure this error quantity for completeness. If the applied probe pattern model is perfect, no error is introduced in the antenna measurement. However, in practice this is of course not the case.

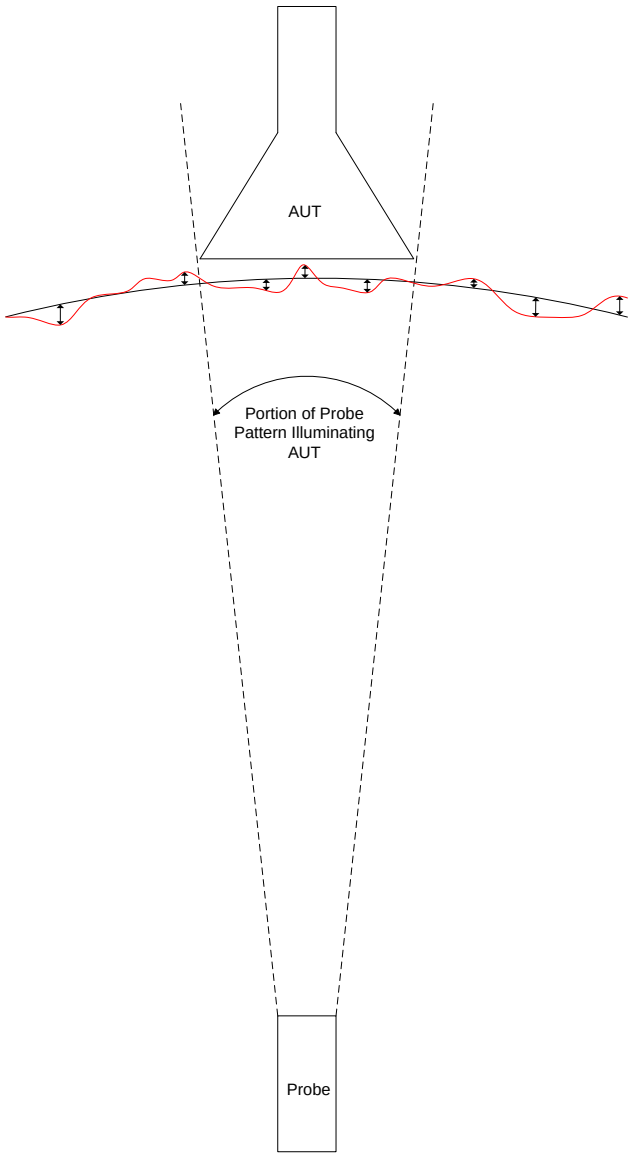


**Figure 2-8: Graphical Representation of the Uncertainty in Probe Relative Pattern**

A method suggested by [12] involves applying probe correction using the probe pattern of the probe with the next lowest operating band. This applied off-frequency calibration will obviously produce results that are grossly in error and thus gives an ample upper bound to the error associated with the probe antenna pattern.

An alternative method for estimating error term #1 involves comparing the probe corrected far-field pattern to a far-field pattern acquired without making use of the probe correction process. This method will obviously yield the upper bound in uncertainty for error term #1. However, since the amplitude of the probe's pattern is quite flat across the region illuminating the AUT, as shown in Figure 2-8, omitting probe correction for SNF measurements should not have a major impact on the resulting far-field pattern. This method has the added benefit of simplifying the probe pattern analysis since choosing whether or not to apply probe correction is a simple matter and is ideally suited for automation as it is a purely post-processing procedure. Again, since this error term typically has a very minor impact on the total measurement uncertainty for SNF systems, even over-estimating its effect on far-field pattern results will not have a noticeable impact on the overall pattern uncertainty.

### 2.5.2 Error Term #2: Probe Polarization

A near-field probe is ideally perfectly linear or circularly polarized. While this condition is nearly satisfied in practice, there is nevertheless some non-zero cross-polarization level that introduces measurement error. Given a probe's co-to-cross polarization ratio, one may determine the measurement uncertainty due to the probe's non-zero cross-polarization level. Reference [19] provides an easy method for determining the pattern error-to-signal ratio (discussed in Section 3.2.3) for this term:

$$Error / S_{MAIN}(\theta,\phi) \cong -(P(\theta,\phi) + p'(\theta,\phi)) + 20\log_{10}\left|1 - 10^{(X_{AUT}(\theta,\phi) - X_{AUT,\,no\,PC}(\theta,\phi))/20}\right| \quad (2.5\text{-}1)$$

$$Error / S_{CROSS}(\theta,\phi) \cong (P(\theta,\phi) + p''(\theta,\phi)) + 20\log_{10}\left|1 - 10^{(A_{AUT}(\theta,\phi) - A_{AUT,\,no\,PC}(\theta,\phi))/20}\right| \quad (2.5\text{-}2)$$

where $Error/S_{MAIN}(\theta,\varphi)$ is the error-to-signal ratio for the co-polarized field and $Error/S_{CROSS}(\theta,\varphi)$ is the error-to-signal ratio for the cross-polarized field component. The terms in the above expressions are defined as:

$P(\theta,\varphi)$ is the main polarization ratio (MPR) of the AUT,

$$P(\theta,\phi) = 20\log_{10}\left(\frac{A_{AUT}(\theta,\phi)}{X_{AUT}(\theta,\phi)}\right) \tag{2.5-3}$$

$p'(\theta,\varphi)$ is the MPR for Probe 1 (or probe position 1 for a single probe setup)

$$p'(\theta,\phi) = 20\log_{10}\left(\frac{A_{Probe1}(\theta,\phi)}{X_{Probe1}(\theta,\phi)}\right) \tag{2.5-4}$$

$p''(\theta,\varphi)$ is the MPR for Probe 2 (or probe position 2 for a single probe setup)

$$p''(\theta,\phi) = 20\log_{10}\left(\frac{A_{Probe2}(\theta,\phi)}{X_{Probe2}(\theta,\phi)}\right) \tag{2.5-5}$$

$X_{AUT,\ no\ PC}(\theta,\phi)$ is the true cross-pol measured field value without applying probe correction.

$X_{AUT}(\theta,\phi)$ is the cross-pol measured field value after applying probe correction.

$A_{AUT,\ no\ PC}(\theta,\phi)$ is the true co-pol measured field value without applying probe correction.

$A_{AUT}(\theta,\phi)$ is the co-pol measured field value after applying probe correction.

$A_{Probe1}(\theta,\phi)$ is the co-pol amplitude of Probe 1 (or probe position 1 for a single probe setup).

$X_{Probe1}(\theta,\phi)$ is the cross-pol amplitude of Probe 1 (or probe position 1 for a single probe setup).

$A_{Probe2}(\theta,\phi)$ is the co-pol amplitude of Probe 2 (or probe position 2 for a single probe setup).

$X_{Probe2}(\theta,\phi)$ is the cross-pol amplitude of Probe 2 (or probe position 2 for a single probe setup).

The determination of this term requires a full knowledge of the probe's co-to-cross polarization performance in all directions. However, approximate values are often selected for several of the required terms above, based on experience and/or knowledge of the probe's properties. It is reasonable to assume that if the AUT and probe cross-pol levels are both low, this error will be negligible away from the main beam.

### 2.5.3 Error Term #3: Probe Gain

To perform the near-field to far-field transformation, knowledge of the probe's gain is required. While the relative pattern of the probe is accounted for in error term #1, it lacks a measure of the uncertainty associated with the probe's gain. This gain includes (naturally) the efficiency of the probe. However, this probe gain is only known with a particular uncertainty. This information would be provided by the probe supplier, with the probe gain uncertainty leading to uncertainty in the measured AUT gain.

The simplest method of quantifying this uncertainty is to quote probe gain uncertainty from the probe's most recent calibration. If this information is not available, one may simply quote the uncertainty to be +/- 0.3 dB, which is typical of an uncalibrated probe. If this uncertainty is too large for a particular setup, one may wish to have the probe calibrated to reduce its gain uncertainty. It should be noted that unlike most error terms, this error term will apply to gain measurements only and will not affect the resulting far-field pattern. If information regarding realized gain in all directions is required, this error term should be included in the final budget for the calculated gain in every direction. However, gain information is typically only requested for the main beam, in which case probe gain uncertainty will only appear in a tabulated peak gain uncertainty budget.

### 2.5.4 Error Term #4: Probe Alignment

This is the error associated with the deviation of the near-field probe alignment relative to the inwards pointing normal of the measurement sphere. It is said that for broad beam probes such as an open-ended waveguide (OEWG) probe, this error term is negligible [12, Table 1]. Moreover, it is stated in [12] that any error associated with this term, however small, is included in the estimation of error term #1: probe relative pattern.

> "*For broadbeam probes like the Open Ended Waveguide (OEWG) probe used here, the effects of probe alignment will be negligible and are considered covered in the estimate of error term #1, Probe Relative Pattern." [12]*

Fortunately, we have solid knowledge of how to estimate error term #1.

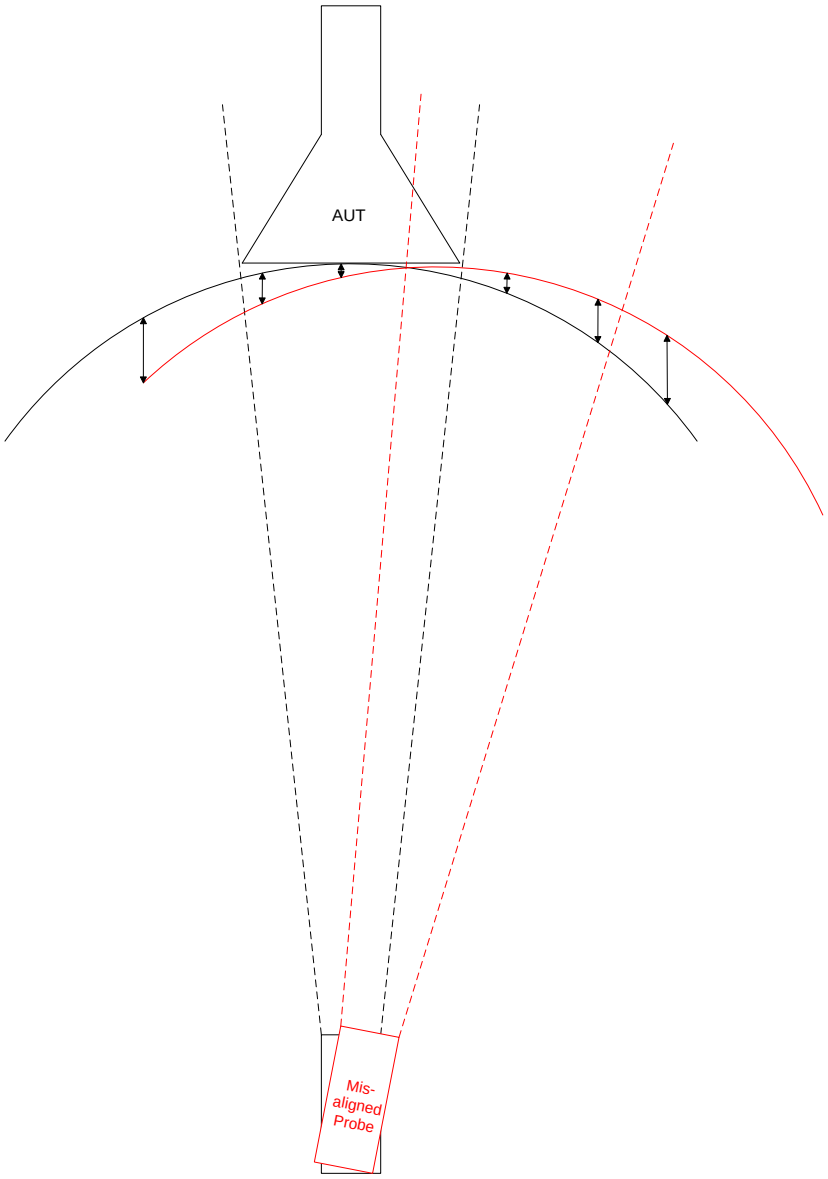


**Figure 2-9: Graphical Representation of Probe Misalignment (Shown Exaggerated for Clarity)**

Reference [20] alludes to the fact that this error term is mostly covered by error term #1: probe relative pattern and error term #2: probe polarization – both of which are well understood. However, Figure 2-9 was included here to help the reader fully understand what a probe misalignment refers to. Similar to Figure 2-8, the black dashed line represents the region of the probe's pattern illuminating the AUT for a well-aligned probe. Again, the black, curved line represents the amplitude distribution of the probe for

the well aligned case, with an exaggerated taper for emphasis. Next, we see the effects of introducing a misalignment to the probe by rotating it so that its pattern peak no longer lies along the Z-axis, as highlighted in red. The arrows between the red and black curved lines represent the amplitude error introduced by a probe misalignment. With this misalignment introduced, the probe correction process will now assume that the probe is well aligned and that its pattern peak lies along the Z-axis, producing a probe misalignment error in the resulting AUT radiation pattern.

While this problem appears to be quite significant, it is found in practice and in the literature ([12] and [20]) that a small probe misalignment will have a minor impact on AUT radiation patterns for SNF systems. For evaluation of this error term it is recommended that one aligns the probe as accurately as possible using typical alignment methods, as detailed in [21, 22]. Beyond this, simply quoting this error term as already included in error term #1 should suffice. Nevertheless error term #4 is retained explicitly.

### 2.5.5 Error Term #5: Normalization Constant

This error term applies to gain measurements only, as it relates to the uncertainties introduced during the physical removal of the AUT and installation of the SGH (or removal of the SGH and installation of the AUT). This error term can be considered a measure of how repeatable the connection feeding the test antenna is. When one removes the AUT to measure the standard gain horn, the position and amount of flex in the cable feeding the AUT/SGH may be altered. This small change in cable positioning can directly alter measured field values, and subsequently affect the measured gain. This error term will also be affected by the introduction or removal of adapters used to connect the cable feeding the AUT/SGH.

A possible evaluation method for this error term involves removing the cable feeding the AUT and immediately reconnecting it. This cable disconnection and reconnection simulates the changes in cable positioning and connector torque introduced when the AUT is replaced with the SGH. By recording the amplitude before and after this process,

one can estimate the amplitude uncertainty due to error term #5. Performing this test multiple times and taking an average is also a possible approach. Unfortunately, this approach is undesirable as it detracts from the automation aspect of the work of this thesis.

An alternative approach is to simply record the on-axis amplitude immediately before beginning a measurement and immediately upon completion of the measurement. By computing the difference in the recorded amplitude, one may estimate the effects due to this error term since cable positioning may have changed between the two points. Additionally, connectors may loosen or tighten slightly over the course of a measurement. If this approach tends to provide results that are simply too optimistic, one should revert to the evaluation method suggested in the above paragraph, although it will introduce additional user intervention steps into the automated error assessment procedure.

### 2.5.6 Error Term #6: AUT/SGH Impedance Mismatch

This term provides an estimate of uncertainty due to a difference in impedance mismatch between the standard gain horn and AUT. From [23]:

> *"Impedance mismatch factor occurs because of non-perfect impedance matches between the SGA and switching/cable network, and between the AUT and its switching/cable network."*

After measuring the complex input reflection coefficients of the generator, SGH and AUT one can use [24]

$$U_{mismatch} = 10\log_{10}\left(\frac{(1-|\Gamma_{SGH}|^2)\,|1-\Gamma_G\Gamma_{AUT}|^2}{(1-|\Gamma_{AUT}|^2)\,|1-\Gamma_G\Gamma_{SGH}|^2}\right)[dB] \qquad (2.5\text{-}6)$$

to determine $U_{mismatch}$, the gain uncertainty for error term #6. $\Gamma_G$, $\Gamma_{SGH}$, and $\Gamma_{AUT}$ refer to the input reflection coefficients of the generator, standard gain horn and AUT,

respectively. This uncertainty will apply to absolute gain measurements only since the difference in mismatch between the AUT and SGH will not affect pattern measurements in any way. Since this process is well established, the user may wish to simply quote a conservative uncertainty. More details relating to the evaluation of this error term as it applies to this thesis can be found in Section 3.3.6.

### 2.5.7 Error Term #7: AUT Alignment

This measurement uncertainty is caused by the mechanical misalignment of the AUT relative to a range reference. This error term is only relevant when performing boresight measurements, in other words whenever one wants to determine the beam peak direction referenced to the antenna's geometry; it is otherwise set to zero. For the purpose of the automated error assessment procedure to be developed in this thesis the analysis of this error term will be omitted. However, if one wished to quantify this error term a proposed error estimation procedure is as follows:

1. AUT misalignment results in the measurement sphere being rotated.
2. The AUT must be aligned manually, and as such, the manual method has an associated uncertainty. This uncertainty would be measured in angular deviation, in degrees or radians and should be noted when the AUT is initially setup and aligned. The details of this uncertainty depend on the alignment method.
3. Post measurement, the measured data is numerically rotated by the angular deviation as determined in step 2.
4. The rotated data is then compared to the final measured data, the difference between them being the error signal (uncertainty) due to AUT alignment.

### 2.5.8 Error Term #8: Near-Field Sampling Density

Error term # 8 involves the errors introduced by the finite number of sampling points used in the near-field measurement. This concept has ties to the well known sampling theorem, in that constructing far-field data from measured near-field data requires that the

sampling points be spaced at a minimum of a half wavelength. This ensures, theoretically, that all information will be captured. In practice however, one finds that as narrower data point spacing is used the computed far-field values will continue to change slightly.

To measure the uncertainty due to data point spacing, one needs two sets of measured data: one measured using the Nyquist sampling criteria and one measured using a higher sampling density. The difference between the two resulting far-field patterns will provide insight into the effects of the chosen near-field sampling density since the two measurement sets should theoretically be identical.

Before beginning a typical spherical near-field antenna measurement one must ensure sufficiently dense sampling in θ and $\phi$. Namely, one must ensure that [1, p.189]

$$\Delta\theta, \Delta\phi \leq \frac{2\pi}{2N+1} \qquad N = kr_0 + 10 \tag{2.5-7}$$

where $r_o$ is the minimum radius fully enclosing the radiating parts of the AUT (also called the maximum radial extent) and $k = 2\pi/\lambda$. This ensures that a sufficient number of spherical modes will be included in the near-field to far-field transformation process in order to fully quantify all sources of energy radiating from the AUT. Therefore, a set of near-field data acquired using

$$\Delta\theta, \Delta\phi = \frac{2\pi}{2N+1} \tag{2.5-8}$$

will be used in this thesis as the normal density data set when performing analysis for error term #8. All measurements in this automated error assessment (or any spherical near-field antenna measurement for that matter) should satisfy this sampling criterion. As previously stated, to determine the uncertainty associated with finite data point spacing, one can compare a scan taken with Δθ and $\Delta\phi$ calculated using the above expression to a scan acquired with a higher sampling density.

### 2.5.9 Error Term #9: Near-Field Measurement Truncation

This error term involves uncertainty relating to the truncation of the spherical measurement surface and will not be applicable to most uncertainty budgets. As outlined in Section 2.4, an SNF scan uses a closed measurement surface, so no data truncation is inherent in this type of measurement unless the user intentionally truncates the spherical scan surface in order to reduce testing time. However, it is useful to include a discussion on truncation in SNF measurements as it provides an excellent understanding of the effects of data truncation in a particular chamber/AUT setup.

The method used to determine this error term is quite simple but ironically requires a full sphere measurement to determine.. First, one must acquire a full sphere of data using any sampling strategy (180-phi, 360-phi, redundant). Next, near-field data from a truncated "window" can be extracted from the full sphere data. This truncated near-field data can then be transformed to far-field data by simply entering field values of zero for the truncated region and performing the near-field to far-field transform using this modified near-field data. Lastly, the two far-field patterns are compared and the difference will become the error level due to the effects of truncation.

When performing the near-field to far-field transformation with a truncated data set, one must ensure that the amplitude of the excluded region is sufficiently lower than the main beam amplitude region to avoid altering the pattern too drastically to be meaningful. For obvious reasons, one should exclude the region of the near-field data acquired with the AUT facing the chamber's back wall. For example, suppose a directive antenna is measured in a SNF environment with the main beam at boresight, $(\theta, \phi) = (0^\circ, 0^\circ)$ using a 180-phi measurement. If the operator wished to reduce chamber occupancy time by 25%, the 360˚ measurement span in θ should be reduced to 270˚. Since the AUT's main beam is aligned to boresight, the portions of the near-field data that should be set to zero are

$$135^\circ \leq \theta \leq 180^\circ, \; -180^\circ \leq \theta \leq -135^\circ \qquad (2.5\text{-}9)$$

In other words, the $\phi$-cuts acquired over the portions of the sphere described above will be discarded prior to performing the transform.

### 2.5.10 Error Term #10: Sphere Radius Errors

As discussed in Section 2.4, error terms #10 and #11 of the NIST 18-term budget were modified to increase their applicability to SNF measurements. Error terms #10 and #11 originally combined to describe the imperfections in the planar scan surface used in PNF measurements, these modified error terms should handle imperfections in the spherical scan surface used in the new SNF measurement.

Error term #10 deals with the uncertainty in the measurement sphere radius. When performing a SNF measurement, one measures the distance from the aperture of the probe to the measurement origin (intersection of $\theta$ and $\phi$ axes shown in Figure 2-4) and the near-field to far-field transform is performed using this radius. However, there is invariably some uncertainty in this measured distance. Therefore, this error term can be handled by simply performing the near-field to far-field transform with a perturbed measurement sphere radius and comparing the resulting far-field pattern to the far-field pattern acquired using the sphere radius as it was measured. The measurement sphere radius should not be confused with the maximum radial extent, $r_0$, described in Section 2.5.8. The measurement radius describes the actual AUT to probe separation, while $r_0$ is simply the radius of a circle centered on the origin that fully encloses the AUT.

### 2.5.11 Error Term #11: Sphere Theta/Phi Errors

Error term #11 actually includes two distinct sources of error relating to the measurement scan surface (sphere for SNF measurements). The first of these sources of error is an axis non-intersection error between the measurement sphere's $\theta$ and $\phi$ axes. In an SNF system, a fundamental requirement is that the two axes of rotation intersect at the origin of the measurement sphere. If this condition does not hold, one will find errors in the resulting measured data [25].

The second source of error deals with the orthogonality of the θ and $\phi$ axes. Similar to axis non-intersection errors, if the θ and $\phi$ axes are not perfectly orthogonal to each other, the resulting far-field data will contain errors. From [25]:

> *"When a phi/theta SNF test system is constructed using two rotary positioners, it is required that the two axes intersect in a point and are orthogonal. These conditions are fundamental in that if they are not met, the coordinate system being described is not truly spherical and the assumptions implicit in the spherical wave transformation are violated."*

Reference [25] uses measured data for a half wavelength dipole AUT acquired in an SNF range to demonstrate the effects of axis non-intersection errors. By artificially introducing a $0.1\lambda$ error in the intersection of the θ and $\phi$ axes in the near-field data, the author of [25] was able to confirm that the introduction of an axis non-intersection error directly affected the resulting far-field pattern. Once this was confirmed, analysis of the measured near-field data was used to develop a method of correcting for axis non-intersection.

While the measured near-field amplitude appears to be unaffected, the measured near-field phase seems to be very sensitive to $\theta/\phi$ axis non-intersection. The author of [25] observes that an axis non-intersection distance *b* will introduce a sinusoidal phase error in the measured near-field data as a function of θ and will be independent of $\phi$. He also provides a method for estimating *b* using a coordinate system transformation. From there, the amplitude of this sinusoidal variation in the near-field phase is found to be proportional to *b* and can be corrected for using

$$Phase\ \ Correction = bk\sin\theta \tag{2.5-10}$$

Once the near-field phase pattern is corrected using the phase correction outlined above, one can simply compare the far-field patterns produced using the raw near-field data to

the far-field patterns obtained using the axis non-intersection corrected near-field data. The resulting difference pattern should provide a good measure of axis non-intersection error in a particular set of measured data.

Reference [25] provides details into the handling of $\theta/\phi$ axis non-intersection errors, but no information is provided toward handling $\theta/\phi$ non-orthogonality errors. While the latter is a well known source of error for SNF measurements [26, 27], no information is provided in the literature on a method of estimating its effects on the resulting far-field patterns. Since a study into the effects of axis non-orthogonality is a research project in itself, error term #11 will handle $\theta/\phi$ axis non-intersection only for the purpose of this thesis. It will be assumed that the axis non-orthognality will have minimal impact on the resulting far-field pattern.

### 2.5.12 Error Term #12: Higher Order Coupling

Error term #12 is associated with the errors due to the higher order coupling between the probe and AUT. The errors arise due to the unwanted fields that couple back and forth between the probe and antenna which alter the measurement results. These unwanted fields are a result of all higher order coupling. This includes all coupling between the probe and AUT except for the desired $1^{st}$ order coupling. As discussed in Section 2.2.2, near-field theory does not address probe/AUT higher order coupling, so one must devise a method of estimating the uncertainty due to error term #12. Therefore, an understanding of the effects of higher order probe/AUT coupling on a measured pattern is required.

A typical measurement is made over the entire sphere, and a second measurement over a sphere with quarter wavelength radius change is performed. In order to acquire the second data set, either the AUT or the probe may be shifted along the z-axis. By *increasing* the probe-to-AUT separation, one may be confident that any conditions required regarding the minimum probe-to-AUT separation are still being satisfied. However, one should note that moving either the probe or AUT may introduce additional alignment uncertainties. Since the uncertainty associated with probe alignment is much

less severe than that associated with the AUT (see *2.5.4*), the best option is to shift the probe rather than the AUT. However, if a particular chamber does not allow for probe movement, care must be taken when moving the AUT as to not swamp the uncertainty associated with higher order coupling by AUT alignment uncertainties. An automated translation procedure could possibly mitigate this source of error since the tolerances of position motors would be well known and potentially controlled. An automated translation feature also eliminates the need for user-intervention in performing the second measurement.

In reference [12] the probe / AUT error term is found to be one of the largest sources of error. Private communication [28] with the authors of [12] reveal that this was due to the use of a chamber with poor absorber on the walls.

In order to obtain the quarter of a wavelength change in sphere radius, a spacer was introduced and as a result of poor chamber performance and manual reconfiguration. The cause of the large error was more due to range reflections and configuration changes than actual distance change [28].

In general, SNF ranges have low error contribution due to unwanted probe / AUT coupling since the probe and AUT have significant physical (and electrical) separation. However, in planar near-field (PNF) measurement setups, the probe / AUT coupling becomes significant due to the required proximity of the two devices during the measurement session. This required proximity is the trade-off used to minimize the size of scan plane while still minimizing truncation errors.

We therefore conclude that the value for the error term #12 quoted in [12] is not typical of SNF measurements. Clearly, care must be taken in the translation to minimize other unrelated sources of error from swamping the error term (namely #12) that one is trying to estimate. Also, since the chamber plays a significant role in this error measurement (though it ideally shouldn't) it will likely always be estimated slightly larger than its true value. That being said, it is not such a terrible thing since it at least does not

underestimate the errors associated with an antenna measurement, although gross overestimation of any uncertainty term is not useful either.

### 2.5.13 Error Term #13: Receiver Amplitude Non-Linearity

This error term requires knowledge of the receiver's non-linearity profile. Using this information, one may simply apply a set of corrections to the measured pattern to account for any amplitude non-linearity. By comparing this corrected dataset to the uncorrected measured data, the uncertainty for this term can be found.

This error term is due to non-linear effects of the receiver used to capture field information. Non-linear is a term that implies that the response of a system is a function of the amplitude of the input signal to that system. This means that a measured field quantity has an associated uncertainty because the response of the attached receiver must be altered to account for this non-linearity.

The method one uses to determine the altered response involves the knowledge of the receiver's non-linearity profile or a continuous transfer function that corrects all measured values given their measured amplitude. One would actually compute the uncertainty by measuring the difference between the uncorrected and corrected data sets. For the purpose of this thesis, a script was developed specifically for the receiver being used in testing to help handle this error term. The correction is performed based on the linearity calibration data of the receiver. Measured amplitude values are adjusted, based on their absolute power levels and this technique therefore allows one to assess the overall impact of the receiver non-linearity on the measurement [29].

This is purely a post-processing approach, only requiring a single data set with which to estimate the uncertainty. Interestingly, the amount of error associated with this error term can be controlled by the amount of power being fed to the AUT or probe (whichever is transmitting), since this would control the amplitude of the received signals.

### 2.5.14 Error Term #14: System Phase Errors

In general, system phase errors are introduced in near-field systems by the moving parts in the measurement setup. In PNF measurement systems, system phase errors are predominantly caused by the flexing of cables. On the other hand, in SNF systems the cables are not appreciably flexed and phase errors are typically introduced by the rotary joints on the multiple rotators in the system.

If the antenna range is well aligned, one can rotate the phi and probe polarization angles in tandem, keeping AUT and probe co-polarized, thereby technically measuring the same observation point of the AUT, but clearly running through all possible rotary joint positions. The maximum peak-to-peak variation between measurements is the worst-case error due to phase errors caused by rotary joints.

One should note that the above mentioned method for estimating the effects of system phase errors will possibly include a multitude of other on-axis sources of error. For example, as the AUT's phi axis and the probe's polarization axis rotate in tandem, the effects of room scattering on the measured near-field values may not remain constant over the full 360 degrees of rotation. Furthermore, it seems critical that the antenna range be well aligned since any misalignment will actually result in a multitude of different points being measured and thus error #14 may be greatly overestimated. That being said, overestimating error isn't necessarily a bad thing unless the errors swamp all other errors. Finally, it should also be stated that this method of analysis will not address the system phase errors associated with the system's theta rotary joint. In the interest of automation, this will be considered a limitation of this process until further research is conducted to devise a test to analyse these effects, which is outside of the scope of this thesis.

### 2.5.15 Error Term #15: Receiver Dynamic Range

This error term considers the errors introduced by the receivers' dynamic range, i.e. its ability to handle very large differences in measured values.

The most common method used to measure receiver dynamic range is to place an attenuator in the receiving path, thereby reducing received power levels and compare the resulting data set to an un-attenuated data set. However, this approach detracts from the theme of automated error assessment, and as such is a less desirable approach (albeit simple to understand and apply).

An alternative measurement presented in [12] for assessing this error term makes use of the SNR of the near-field signal on-axis and uses this value as the error signal associated with the receiver's limited dynamic range. In other words, the error level at all points becomes $-SNR_{dB}(\theta = 0, \phi = 0)$. With a normalized pattern peak of 0 dB, the calculated SNR tells one how far below the pattern peak the noise floor is. The noise floor can be considered the error signal for this term. From this, one may find the error-to-signal ratio and pattern uncertainty. There are different approaches to calculating the SNR in a measurement system. The method used for the results in this thesis will be presented in section 4.15.

### 2.5.16 Error Term #16: Room Scattering

A significant source of error in a spherical near-field setup is the contribution due to room scattering. This is caused by imperfect absorbers, the probe/AUT mounts, mechanical rotators or any other scattering objects that cause the environment to deviate from the free-space requirement.

A common method to measure the errors introduced by room scattering involves moving the AUT to different positions and measuring the antenna pattern. These changes in AUT location should be electrically large enough to cause a significant change in room scattering. If the room were perfect and scattering completely suppressed, the change in position would not change the measured field values. However, since the amount of scattering is direction dependent, one certainly sees some change in measured values after moving the AUT. The problem that arises with this approach is that moving the

AUT invariably introducing alignment errors that mask the true amount of uncertainty due to room scattering. This method for estimating room scattering also presents the added drawback of being difficult to automate.

An alternative approach is to utilize a redundant theta/phi data set as the basis for room scattering error estimation [12]. The AUT points in different directions in the chamber during each measurement set, and the differences between the computed far-field values can be attributed to chamber performance. This approach has the advantage of simplifying automation since the AUT does not need to be removed from the setup between measurements. The redundant measurement data is also used for other error term estimations.

So to quantify the effects of room scattering in an automated sense, one may wish to compare a 360-phi scan to a 180-phi scan. Since these two scans will have reflection contributions from different parts of the chamber, a comparison of the two should yield an ample upper bound to the error associated with room scattering. It should be noted that both of the 180-Phi and 360-Phi data can be extracted from the redundant data set so only one measurement is required here. However, one should note that this method will typically overestimate errors associated with room scattering since the 180-phi/360-phi scans will contain reflections from different parts of the chamber. Because the AUT points in different directions within the chamber for 180-phi/360-phi scans, estimation of error term #16 in this way will also be inaccurate if the AUT alignment is poor, with the bad alignment swamping the effects of room scattering.

An alternative approach to quantifying the uncertainty associated with room scattering is to compare a redundant scan to either its 180-phi subset or its 360-phi subset. Since the redundant measurement is essentially an average of the 180-phi and 360-phi subsets, one finds that the room scattering errors are mostly averaged out. We will see in Section 3.2.1 that a redundant measurement will be used to provide the quoted AUT radiation pattern. While some of the effects of room scattering are averaged out, we still wish to know the effects of what is left of the room scattering. Therefore, this comparison should yield

more realistic uncertainties than if one was to compare the 180-phi dataset to the 360-phi dataset. This method, like the previously discussed method, has the added benefit of aiding the automation process as it relies solely on one redundant measurement. When choosing the data subset used for comparison (180-phi or 360-phi) with the redundant sphere data, the data acquired using the measurement geometry typically employed in a particular SNF chamber should be selected.

### 2.5.17 Error Term #17: Cable Leakage

In an SNF antenna measurement, unwanted cable radiation also has impact (albeit minor) on measured quantities and will thus introduce an uncertainty of its own.

The estimation approach here is straightforward. By disconnecting the cable feeding the transmitting antenna and loading it with a 50Ω load, one can measure a full sphere of cable leakage data. With a full sphere of cable leakage data recorded, there are two methods of quoting measurement uncertainty associated with error term #17.

i) By comparing the cable leakage radiation pattern with any of the AUT's radiation patterns (provided they were performed using identical settings) one can quickly determine the error-to-signal ratio and thus measurement uncertainty, as will be explained in Section 3. As an example, one may wish to measure a 180-Phi dataset for a particular AUT. Upon completion, the cable feeding the transmitting antenna can be removed, the cable loaded with 50Ω and the 180-Phi measurement performed again. Because these patterns were acquired using identical settings the difference signal can easily be converted to a measurement uncertainty. This method has the advantage of quoting the most recent and accurate cable leakage uncertainties. However, this option may prove time consuming and unnecessary since this error term is actually AUT-independent. This method also requires two user-intervention steps (AUT disconnection and reconnection) and is undesirable with respect to full automation.

ii) One may wish to save measurement and processing time by simply applying a full sphere uncertainty profile due to cable leakage to a particular AUT's radiation pattern directly. For example, if a radiation pattern was acquired for a particular AUT one may wish to use a look-up table containing cable leakage information specific to the chamber and test frequency of interest. Therefore, the look-up table must contain a full sphere of measurement uncertainty data for the measurement frequency. It should be noted, however, that this full sphere of uncertainty data must have been acquired using option *i,* above. Therefore, a periodic cable leakage analysis should be performed to ensure up-to-date look-up tables.

We note that cables tend to flex during antenna measurements, the cable leakage data may vary depending on the sampling strategy used (180-Phi, 360-Phi, redundant). Therefore, a good approach is to perform a double sphere leakage pattern and extract the 180-phi and 360-phi subsets for analysis. The worst-case uncertainty of the two can then become the quoted uncertainty. In the future, look-up table updates can be hastened by measuring only the 180-phi or 360-phi sphere which produced the greatest uncertainty for this error term.

### 2.5.18 Error Term #18: Repeatability and Random Errors

This error term is essentially the system repeatability and can be easily evaluated by performing two identical measurements one after another. By comparing the resulting patterns, one can extract the uncertainty due to system repeatability. It is useful to note that regardless of how small the uncertainty due to system repeatability is, it will be present in every other error term that requires two measurements for comparison. Therefore, if the uncertainty due to system repeatability is significant, several other error terms will be swamped by the effects of poor system repeatability. Therefore, if the system repeatability is very poor one may wish to set error term #18 to zero as its effect is

already included in several other error terms, although a poor system repeatability is a major concern in itself.

## 2.6 CONCLUDING REMARKS

The chapter began with a review of antenna measurement techniques. Some terminology and expressions related to different types of SNF datasets, and which will be frequently referred to later, is provided in Section 2.2. Previous research on SNF antenna measurement uncertainty assessment was reviewed in Section 2.3, followed by a discussion on the need for an assessment approach that can be automated. Section 2.4 summarized an existing near-field antenna measurement 18-term error budget that has been adapted by others for the SNF case. Some terminology changes were made for clarity. Details of each error term are presented in Section 2.5. Some of this material on error assessment in antenna measurements was either only accessible in fragmented form in the literature, or as knowledge possessed by individuals but not written down anywhere. Its collation here served as the basis for the refinement of two of the error terms into a form better suited for SNF purposes, and the introduction of some new tests (measurements) that are described in context in Chapter 3. In Chapter 3 details essential to the implementation of an automated SNF error assessment scheme will be described, followed by verification of the procedure through its application to four different antenna types in Chapter 4.

## 2.7 REFERENCES FOR CHAPTER 2


1. J.E. Hansen. *Spherical Near-Field Antenna Measurements*. London: Peter Peregrinus Ltd, 1988.
2. Near-Field Systems Inc. (2006). *Near-Field 101*. [Online]. Available: http://www.nearfield.com/theory.htm
3. C.A. Balanis. Antenna Theory: Analysis and Design, 3rd ed. Wiley Interscience, 2005.
4. D. M. Kerns and E. S. Dayhoff, "Theory of Diffraction in Microwave Interferometry", J. Res. Natl. Bur. Stand. 64B, 1-13 (1960).
5. A. Newell. (NSI, 2009). *Near Field Antenna Measurement Theory, Planar, Cylindrical and Spherical.* [Online]. Available: http://nearfield.com/Nearfield_Antenna_Test_Theory.pdf
6. G. Hindman, A. Newell, "Mathematical Absorber Reflection Suppression (MARS) for Anechoic Chamber Evaluation and Improvement", Proc. Antenna Measurement Techniques Association (AMTA) Annual Symp., 2008. *(CD-Rom)*
7. D.J. Janse van Rensburg, S. Mishra, G. Seguin, "Simulation of Errors in Near-Field Facilities", Proc. Antenna Measurement Techniques Association (AMTA) Annual Symp., pp. 336 – 340, 1995.
8. A. Newell, G. Hindman, "Quantifying the Effect of Position Errors in Spherical Near-Field Antenna Measurements", Proc. Antenna Measurement Techniques Association (AMTA) Annual Symp., pp. 145 – 149, 1998.
9. A. Newell, G. Hindman, "The Alignment of Spherical Near-Field Rotator using Electrical Measurements", Proc. Antenna Measurement Techniques Association (AMTA) Annual Symp., pp. 131 – 136, 1997.
10. A. Newell, G. Hindman, "The Effect of Measurement Geometry on Alignment Errors in Spherical Near-Field Measurements", Proc. Antenna Measurement Techniques Association (AMTA) Annual Symp., pp. 274 – 279, 1999.
11. D. Hess, "An Expanded Approach to Spherical Near-Field Uncertainty Analysis", Proc. Antenna Measurement Techniques Association (AMTA) Annual Symp., 2002. *(CD-Rom)*

12. G. Hindman, A. Newell, “Simplified Spherical Near-Field Accuracy Assessment”, Proc. Antenna Measurement Techniques Association (AMTA) Annual Symp., 2006. *(CD-Rom)*
13. M. Francis, R. Wittmann, “Uncertainty Analysis for Spherical Near-Field Measurements”, Proc. Antenna Measurement Techniques Association (AMTA) Annual Symp., 2003. *(CD-Rom)*
14. R. Wittmann, M. Francis, “Spherical-Scanning Measurements: Propagating Errors through the Near to Far-Field Transformation”, Proc. Antenna Measurement Techniques Association (AMTA) Annual Symp., 2004. *(CD-Rom)*
15. A. Newell, “Estimating the Uncertainties due to Position Errors in Spherical Near-Field Measurements”, Proc. Antenna Measurement Techniques Association (AMTA) Annual Symp., 2003. *(CD-Rom)*
16. G. Hindman, A. Newell, “Spherical Near-Field Self-Comparison Measurements”, Proc. Antenna Measurement Techniques Association (AMTA) Annual Symp., 2004. *(CD-Rom)*
17. M. Francis, J. Guerrieri, K. MacReynolds, R. Wittmann, “Estimating Multiple-Reflection Uncertainties in Spherical Near-Field Measurements”, Proc. Antenna Measurement Techniques Association (AMTA) Annual Symp., 2004. *(CD-Rom)*
18. A. Newell, G. Hindman, “Planar and Spherical Near-Field Range Comparison with -60 dB Residual Error Level”, Proc. Antenna Measurement Techniques Association (AMTA) Annual Symp., 2007. *(CD-Rom)*
19. A. Newell, “Cross Polarization Uncertainty in Near-Field Probe Correction”, Proc. Antenna Measurement Techniques Association (AMTA) Annual Symp., 2008. *(CD-Rom)*
20. A. Newell, “Error Analysis Techniques for Planar Near-Field Measurements”, IEEE Transactions on Antennas and Propagation, Vol. 36, No. 6, pp. 754 – 768, June 1988.
21. S. W. Zieg, “A Precision Optical Range Alignment Technique”, Proc. Antenna Measurement Techniques Association (AMTA) Annual Symp., Paper No. 14, pp. 1 - 20, 1982.

22. J. Demas, (Feb, 2010), *"Spherical Scanner Alignment Procedures"*, NSI Application Note, *Internal Document.*
23. Near-Field Systems Inc., (May, 2005), "*NSI 2000 Operating Manual*", NSI.
24. D. J. van Rensburg, (Nov, 2010), *"Correcting for SNF Axis Non-Intersection Errors"*, NSI Application Note, *Internal Document.*
25. D. J. van Rensburg, (Nov, 2010), *"Impedance Mismatch Error"*, NSI Application Note, *Internal Document.*
26. D. J. Janse van Rensburg, S. R. Mishra, P. J. Wood, G. Séguin, "Compensation for Transverse Antenna Offset in Spherical Near-Field Antenna Measurements", ICEAA Conference Proceedings, Torino, Italy, Sept. 1995.
27. D. J. Janse van Rensburg, S. R. Mishra, G. Séguin, "Simulation of Errors in Near-Field Facilities", Proc. Antenna Measurement Techniques Association (AMTA), Williamsburg, Virginia, USA, Nov. 1995.
28. G. Hindman, Nearfield Systems Inc., 19730 Magellan Dr., Torrance, CA, 90502, USA. *Private Communication*.
29. P. Pelland, D. J. van Rensburg, D. A. McNamara, L. Shafai, S. Mishra, M. Gavrilovic, "Some Detailed Implementation Aspects of an Automated Error Assessment Scheme for Antenna Spherical Near-Field Measurements", Proc. Antenna Measurement Techniques Association (AMTA) Annual Symp., 2010.

# CHAPTER 3: Error Term Evaluation Requirements

## 3.1 INTRODUCTION

In this chapter the reader will find all of the technical details required to implement an automated error assessment process for any SNF environment. First, in Section 3.2, a list of definitions and some terminology crucial to understanding errors in SNF measurements will be provided. It will also discuss the concept of the spherical near-field "truth model", the measurement with respect to which all measurement uncertainties will be referenced. Next, in Section 3.3, implementation details will be provided for the determination of each error term, based on the analysis in Section 2.5. After reading this section it should be clear to the reader exactly how a particular error term is evaluated and which measurements it makes use of for this evaluation. Based on the evaluation requirements discussed in Section 3.3, a list of proposed measurements will be presented in Section 3.4. This set of measurements is sufficient to extract all uncertainty information for the eighteen error terms presented in Section 2.4. This set of measurements will be optimized to reduce overall test times while still providing reasonable estimates of the errors in the quantities being measured. Finally, the reader will be presented with some concluding remarks in Section 3.5. The latter section will set the stage for Chapter 4, as a list of antennas that will be used to test the automated error assessment procedure will be presented.

## 3.2 USEFUL DEFINITIONS AND NOTATION

Before proceeding with evaluation requirements specific to individual error terms, one must become familiar with some terminology relating to SNF measurement uncertainty. Since this thesis attempts to fully quantify all sources of amplitude uncertainty in SNF measurements, there will be no mention of phase uncertainty at any point. However, many of the comparisons shown in Section 3.3 can provide insight into the sources of phase errors. This chapter will also only discuss co-polarized amplitude uncertainty. Unless stated otherwise, the word "amplitude" refers to the un-normalized, co-polarized amplitude of the far-field pattern. However, the methods used to evaluate the co-

polarized amplitude uncertainty are all valid for the cross-polarized component of the far-field pattern. Two terms that will be referenced quite often throughout this chapter are explained below:

- $M_i$ refers to the $i^{th}$ complete spherical near-field measurement acquired for the purpose of the error assessment process. Once error term evaluation requirements have been outlined for all eighteen error terms in Section 3.3, a complete, ordered list of the required measurements will be presented to the reader in Section 3.4.

- $A_i(\theta,\phi)$ refers to the un-normalized, co-polarized amplitude of the far-field pattern in the direction $(\theta,\phi)$ in dB, computed using the measured near-field data of the corresponding measurement $M_i$. The only exception is the use of $A_5(\phi)$ in Section 3.3.14.

### 3.2.1 Quoted AUT Radiation Pattern

In Chapter 2, the reader was presented with details to help understand all sources of error in SNF measurements. The ultimate goal of this thesis is to utilize this information and determine the overall amplitude uncertainty of a particular AUT radiation pattern. This error assessment process does not attempt to reduce the effects of the various sources of errors presented in Table 2-2, but to instead simply identify them. Once all errors have been estimated using the evaluation processes found in Section 3.3 one must select a "truth model" which will be considered the final, quoted AUT radiation pattern. This quoted AUT radiation pattern should be acquired in such a way that the effects of the various sources of error are minimized as much as possible without any additional post-processing. In the end, the amplitude uncertainty will be taken with respect to the chosen quoted AUT radiation pattern.

The authors of [1] suggest three criteria for selecting a "truth model":

1. Measure data with minimal positional errors by using a slower scan speed than is typically employed in a particular SNF chamber.

2. Average out errors that are highly dependent on the chosen sampling strategy by using a redundant measurement.
3. Apply a reflection suppression technique similar to that of [2].

As previously stated, this automated error assessment process does not attempt to reduce the amplitude uncertainty of a particular radiation pattern. Because of this, in this thesis no reflection suppression technique will be used in the quoted AUT radiation pattern as the effects of room scattering must be included in the final uncertainty budget. The quoted AUT radiation pattern will be computed using a redundant measurement taken at slow scan speed[2] and this measurement will be saved as $M_1$. The amplitude of the quoted AUT radiation pattern will be denoted $A_1(\theta,\phi)$ or $S(\theta,\phi)$, for reasons that will become obvious in Section 3.2.4.

### 3.2.2 Error Signal Evaluation

The first step toward computing the far-field amplitude uncertainty for a particular error term is to estimate that term's error signal level. The error signal level is defined as the difference in amplitudes of two otherwise (in the ideal case) identical radiation patterns and can be computed using

$$Error(\theta,\phi) = 20\log_{10}\left|10^{A_p(\theta,\phi)/20} - 10^{A_q(\theta,\phi)/20}\right| \quad [dB] \tag{3.2-1}$$

In other words, this equation computes the difference between the far-field amplitude obtained via measurements $M_p$ and $M_q$. Recall that $A_p(\theta,\phi)$ refers to the co-polarized amplitude of the $p^{th}$ far-field pattern in the direction $(\theta,\phi)$ in dB; determined by performing the near-field to far-field transformation on measurement $M_p$.

[2] The slow scan speed used in the quoted AUT radiation pattern corresponds to 3˚/second for this particular SNF system, whereas a normal scan speed is 10˚/second.

Next,

$$Error_n(\theta,\phi) = 20\log_{10}\left|10^{A_i(\theta,\phi)/20} - 10^{A_j(\theta,\phi)/20}\right| \quad [dB] \tag{3.2-2}$$

is used to estimate the error signal level specific to the $n^{th}$ error term, where $n$ refers to one of the eighteen error terms listed in the modified NIST budget outlined in Table 2-2 of Section 2.4. The subscripts $i$ and $j$ refer to measurements $M_i$ and $M_j$, the two measurements required to evaluate the effects of a particular error term. For example, recall from Section 2.5.1 that the error associated with the probe's pattern can be estimated by comparing two far-field patterns acquired with and without probe correction. In this particular example, the error signal for error term #1 can be computed using

$$Error_1(\theta,\phi) = 20\log_{10}\left|10^{A_{PC}(\theta,\phi)/20} - 10^{A_{noPC}(\theta,\phi)/20}\right| \quad [dB] \tag{3.2-3}$$

where $A_{noPC}(\theta,\phi)$ is the far-field amplitude of an arbitrary measurement in the direction $(\theta,\phi)$ without, and $A_{PC}(\theta,\phi)$ is the amplitude of the far-field pattern acquired with probe correction.

### 3.2.3 Error-to-Signal Ratio Evaluation

Once an error signal level has been determined using equation (3.2-2), the error-to-signal ratio can be determined using equation (3.2-4)

$$Error(\theta,\phi)/S(\theta,\phi) = \left\{Error(\theta,\phi) - S(\theta,\phi)\right\} \quad [dB] \tag{3.2-4}$$

In this expression, the term $S(\theta,\phi)$ indicates the un-normalized, calculated far-field signal amplitude of the quoted AUT radiation pattern in the direction $(\theta,\phi)$ in dB. Recall from Section 3.2.1 that the quoted AUT radiation pattern refers to the far-field amplitude acquired via measurement $M_1$, so that $S(\theta,\phi) = A_1(\theta,\phi)$. At this point, it is clear that the evaluation of the error-to-signal ratio specific to the $n^{th}$ error term will take the form [3, p. C-1]

$$Error(\theta,\phi)/S(\theta,\phi)_n = \left\{Error_n(\theta,\phi) - S(\theta,\phi)\right\} \quad [dB] \tag{3.2-5}$$

### 3.2.4 Pattern Amplitude Uncertainty Evaluation

Finally, once the error-to-signal ratio of a source of error has been determined, the expression

$$U(\theta,\phi) = \pm 20\log_{10}(1-10^{[Error(\theta,\phi)/S(\theta,\phi)]/20}) \quad [dB] \tag{3.2-6}$$

may be used to determine the resulting amplitude uncertainty [3, p. C-1]. Expression (3.2-6) clearly shows that if an error-to-signal ratio is sufficiently low, the resulting pattern amplitude uncertainty will also be low.

Finally, the contribution of the $n^{th}$ error term to the uncertainty in the quoted AUT radiation pattern can be found as

$$U_n(\theta,\phi) = \pm 20\log_{10}(1-10^{[Error(\theta,\phi)/S(\theta,\phi)_n]/20}) \quad [dB] \tag{3.2-7}$$

### 3.2.5 Method of Error Term Combination

Once all amplitude uncertainties have been determined with respect to the quoted AUT radiation pattern, they must be combined in such a way that they provide insight into the overall pattern amplitude uncertainty. While the chosen method of combining the various error terms varies from publication to publication, [4] suggests that the particular method employed is not important. However, it is important that one remains consistent and always provides the rationale as to why a particular combination scheme was selected.

For the purposes of the error assessment process discussed here, the root-sum-of-squares (RSS) combination scheme will be used. In such an RSS analysis, which will be the approach used in this thesis, each of the eighteen computed uncertainties is first squared. They are then added together and the square root of this sum is taken to determine the overall amplitude uncertainty, as

$$U_{total}(\theta,\phi) = \sqrt{\sum_{1}^{18} U_n(\theta,\phi)^2} \quad dB \tag{3.2-8}$$

This RSS total uncertainty is the overall estimated uncertainty of the SNF measurement. RSS analysis is appropriate when there are several sources of uncertainty and the uncertainties are only loosely correlated, as is being assumed here. RSS analysis is most appropriate for use with worst-case estimates. Since we desire to simply estimate the effects of the various sources of error, such a worst-case approach is acceptable here. Experience has shown that in these cases the RSS method yields the most reasonable result [5]. Of course nothing should be so over-estimated in the worst case direction that the error assessment process ceases to be useful.

## 3.3 ERROR TERM EVALUATION REQUIREMENTS

In this section, the reader will be presented with all of the details required to determine the measurement uncertainty of all eighteen error terms. Based on the discussions presented in Section 2.5, specific expressions will be provided to determine the impact of each source of error, in turn. These expressions will also present specific requirements relating to the SNF measurement setup used in the various error term evaluations. All of these requirements will permit the selection of a standardized set of measurements which can be acquired automatically in the SNF chamber. This set of measurements will be selected in such a way as to reduce the overall test time, while still providing a complete picture of the amplitude uncertainty in the quoted AUT radiation pattern. Table 3-1 below summarizes the various methods suggested in Section 2.5 to estimate the effects of all eighteen error terms. In what follows, Section 3.3 discusses the procedure relevant to the $n^{th}$ error term.

**Table 3-1: Summary of Error Term Evaluation Methods**

| # | Error Term | Evaluation Method |
|---|---|---|
| 1 | Probe Relative Pattern | Compare probe corrected far-field pattern to the uncorrected far-field pattern. |
| 2 | Probe Polarization | Use the equations found in Section 2.5.2 based on the measured field values. |
| 3 | Probe Gain | Quote a probe gain uncertainty based on the probe calibration status, included in gain budgets only. |
| 4 | Probe Alignment | Included in error terms #1 and #2. |
| 5 | Normalization Constant | Record the on-axis amplitude at the start and end of any measurement and set $U_5$ to the difference. |
| 6 | AUT/SGH Impedance Mismatch | Use (2.5-6) to estimate the AUT gain uncertainty based on SGH/AUT impedance mismatch. |
| 7 | AUT Alignment | This error term is not applicable for the purposes of this thesis. |
| 8 | Data Point Spacing | Compare a dataset acquired using the sampling outlined in (2.5-8) to one acquired using narrower sampling density. |
| 9 | Data Truncation | Compare a far-field pattern obtained using an un-truncated dataset to one obtained using an open near-field measurement surface. |
| 10 | Sphere Radius Errors | Compute the far-field pattern using perturbed probe scan radius and compare to the far-field pattern obtained with the actual, measured probe scan radius. |
| 11 | Sphere $\theta/\phi$ Errors | Compare axis non-intersection corrected far-field pattern to the uncorrected far-field pattern. |
| 12 | Higher Order Coupling | Compare two scans acquired with a quarter wavelength difference in the probe to AUT distance. |
| 13 | Receiver Amplitude Non-Linearity | Compare amplitude non-linearity corrected far-field pattern to the uncorrected far-field pattern. |
| 14 | System Phase Errors | Rotate the AUT and probe in tandem, remaining co-polarized throughout the scan. Note the peak-to-peak field variation. |
| 15 | Receiver Dynamic Range | Note the on-axis SNR value of a measurement. The error level at all points is then set to $-SNR_{dB}$. |
| 16 | Room Scattering | Compare the resulting far-field patterns acquired using two measurements taken with different scan geometries. |
| 17 | Cable Leakage | Perform a leakage analysis using one of the methods outlined in Section 2.5.17. |
| 18 | Repeatability and Random Errors | Compare the resulting far-field patterns of two identical scans, taken back-to-back. |

### 3.3.1 Error Term #1: Probe Relative Pattern

To determine the effects of this error term, the probe-corrected far-field values of the quoted radiation pattern, $M_1$, are compared to the uncorrected far-field values of the measurement $M_1$. The probe correction process accounts for the probe's gain, so the difference between the two normalized patterns becomes the error signal for this term, as

$$Error_1(\theta,\phi) = 20\log_{10}\left|10^{[A_1(\theta,\phi)-\max\{A_1\}]/20} - 10^{[A_{1a}(\theta,\phi)-\max\{A_{1a}\}]/20}\right| \quad (3.3\text{-}1)$$

where $A_{1a}$ refers to the uncorrected far-field amplitude from measurement $M_1$. Then the error-to-signal ratio of error term #1 can be computed using

$$Error/S(\theta,\phi)_1 = Error_1(\theta,\phi) - S(\theta,\phi) \quad (3.3\text{-}2)$$

and the associated amplitude uncertainty of $A_1$ due to error term #1 can be estimated as

$$U_1(\theta,\phi) = \pm 20\log_{10}(1-10^{[Error(\theta,\phi)/S(\theta,\phi)_1]/20}) \quad (3.3\text{-}3)$$

### 3.3.2 Error Term #2: Probe Polarization

In Section 2.5.2 a set of equations was presented which can be used to estimate the errors introduced by the non-zero cross-polarization levels of the probe. In order to perform these calculations, several amplitude patterns must be stored:

- $A_1(\theta,\phi)$: The co-polarized far-field amplitude (dB) resulting from performing the near-field to far-field transformation on the $M_1$ dataset (with probe correction).
- $X_1(\theta,\phi)$: The cross-polarized far-field amplitude (dB) resulting from performing the near-field to far-field transformation on the $M_1$ dataset (with probe correction).
- $p'(\theta,\phi)$: The main polarization ratio of the SNF probe (dB). If this information is not provided, one may wish to use simulated co-to-cross polarization ratios for the probe. In fact, this information is typically not provided by the probe manufacturer.

- $X_{1a}(\theta,\phi)$: The true, measured cross-polarized far-field amplitude (dB) resulting from performing the near-field to far-field transformation on the $M_1$ dataset without probe correction.

Using the amplitude patterns listed above and the expression

$$Error/S(\theta,\phi)_2 = -A_1(\theta,\phi) + X_1(\theta,\phi) - p'(\theta,\phi) + 20\log_{10}\left|1-10^{(X_1(\theta,\phi)-X_{1a}(\theta,\phi))/20}\right| \quad \textbf{(}3.3\text{-}4)$$

one may estimate the error-to-signal ratio for this error term. Then the associated amplitude uncertainty of $A_1$ due to error term #2 can be estimated using

$$U_2(\theta,\phi) = \pm 20\log_{10}(1-10^{[Error(\theta,\phi)/S(\theta,\phi)_2]/20}) \quad (3.3\text{-}5)$$

### 3.3.3 Error Term #3: Probe Gain

Recall from Section 2.5.3 that this error term applies to gain measurements only and it simply set by the user based on the probe's calibration status. For an un-calibrated probe, a conservative probe gain uncertainty of roughly 0.3 dB is typically chosen. However, since this error term is often found to dominate the gain uncertainty budget, one may wish to have a particular probe calibrated to reduce the uncertainty to 0.1 dB say.

$$U_3 = \begin{cases} 0.1\,dB, & calibrated\ probe \\ 0.3\,dB, & uncalibrated\ probe \end{cases} \quad (3.3\text{-}6)$$

### 3.3.4 Error Term #4: Probe Alignment

Recall from Section 2.5.4 that it is recommended that one aligns the probe as accurately as possible using typical alignment methods. Beyond this, the minor effects of probe misalignment will already be accounted for in the evaluation of error terms #1 and #2. Therefore, no unique evaluation requirements will be included in the error assessment process to account for the effects of probe misalignment.

### 3.3.5 Error Term #5: Normalization Constant

Using the evaluation method discussed in Section 2.5.5, one may estimate the uncertainty associated with error term #5. Recall that this error term applies to absolute gain measurements only, as it relates to connector/cable repeatability between the AUT and SGH setups. Also recall that should the automated approach for the evaluation of this term provide estimates that are too optimistic, one should revert to the manual approach of disconnecting/reconnecting the feed cable and noting the amplitude variation.

### 3.3.6 Error Term #6: AUT/SGH Impedance Mismatch

As outlined in Section 2.5.6, the differences in mismatch between the AUT input port and the SGH input port will introduce some uncertainty in the measured gain of the AUT. Using expression (2.5-6), one may compute the uncertainty based on the measured reflection coefficient of the AUT and SGH input ports. Since an accurate measurement of these values often requires placing a network analyzer in the test range, one may simply wish to estimate this uncertainty value based on simulation. In this case, conservative values may be used in place of measured reflection coefficients for expression (2.5-6).

### 3.3.7 Error Term #7: AUT Alignment

In Section 2.5.7 it was stated that this term only applies when one wishes to determine the beam peak direction referenced to the antenna's geometry. As discussed there, in most cases this term will be set to zero and labeled as "not applicable". However, if one wished to assess this error term, the far-field pattern from $M_1$ is rotated using the method proposed in Section 2.5.7 and the resulting, rotated far-field amplitude, $A_{1b,}$ can be compared to $A_1$ to estimate the error signal level for this term. Expressions

$$Error_7(\theta,\phi) = 20\log_{10}\left|10^{A_1(\theta,\phi)/20} - 10^{A_{1b}(\theta,\phi)/20}\right| \tag{3.3-7}$$

$$Error/S(\theta,\phi)_7 = Error_7(\theta,\phi) - S(\theta,\phi) \tag{3.3-8}$$

and

$$U_7(\theta,\phi) = \pm 20\log_{10}(1-10^{[Error(\theta,\phi)/S(\theta,\phi)_7]/20}) \quad (3.3\text{-}9)$$

are used to determine the error signal level, the error-to-signal ratio, and the amplitude uncertainty of $A_1$ due to error term #7, respectively.

### 3.3.8 Error Term #8: Near-Field Sampling Density

In Section 2.5.8, it was stated that the evaluation of error term #8 required that a comparison be made between two measurements taken with different sampling densities. In particular, one set of data should be acquired using the recommended Nyquist sampling rate (regular density scan) given by (2.5-8) and the other using a higher sampling density (high density scan).

Interestingly, if one has the ability to manipulate near-field data after acquiring it, this error term can be evaluated using only a single measurement to reduce total acquisition time. After performing a high density scan, one may simply extract only the near-field points that correspond to a regular density scan and save this data as if it had been acquired using a regular density measurement. In other words, the near-field to far-field transformation will now be performed on two datasets: the measured high density scan and the extracted regular density subset of that scan.

Since the regular density scan used for comparison will be extracted from the high density scan, one must take care to ensure that all points corresponding to a typical, regular density scan is actually included in the high density acquisition. To ensure this it is recommended that the high density measurement be acquired with precisely twice the sampling density recommended by (2.5-8). This double density scan will obviously then include all points required for the extraction of the regular density subset.

Thus far in the discussion only the measurement that produces the quoted AUT radiation pattern has been mentioned, namely $M_1$. Since this measurement uses the recommended Nyquist sampling rate, a second measurement, $M_2$, will be proposed to evaluate the

uncertainty associated with error term #8. This measurement will use twice the sampling rate determined from (2.5-8), namely

$$\Delta\theta, \Delta\phi = \frac{\pi}{2N+1} \tag{3.3-10}$$

Once measurement $M_2$ has been completed, the near-field to far-field transformation can be used to compute $A_2$. Next, the regular density subset of the near-field data points obtained via measurement $M_2$ is extracted. Using this extracted, regular density subset of $M_2$, the near-field to far-field transformation is performed to obtain $A_{2a}$. At this point, the error signal level due to the chosen near-field data point spacing can be computed using

$$Error_8(\theta,\phi) = 20\log_{10}\left|10^{A_2(\theta,\phi)/20} - 10^{A_{2a}(\theta,\phi)/20}\right| \tag{3.3-11}$$

Thereafter the error-to-signal ratio of error term #8 can be computed using

$$Error/S(\theta,\phi)_8 = Error_8(\theta,\phi) - S(\theta,\phi) \tag{3.3-12}$$

and the associated amplitude uncertainty of $A_1$ due to error term #8 can be estimated using

$$U_8(\theta,\phi) = \pm 20\log_{10}(1 - 10^{[Error(\theta,\phi)/S(\theta,\phi)_8]/20}) \tag{3.3-13}$$

### 3.3.9 Error Term #9: Near-Field Measurement Truncation

Recall from Section 2.5.9 that the evaluation of this error term will not normally be required for most SNF error assessments. Since an SNF measurement typically requires that near-field data be acquired over a closed surface, data truncation is not inherently present and should be listed as "not applicable" in the overall error budget. However, if one wished to determine the effects that truncating the measurement window has on the resulting far-field pattern, the expressions below can be used to this end.

First, a truncated subset of the near-field data points acquired using measurement $M_2$ will be extracted. All of the excluded near-field amplitude values are then set to zero. The far-

field pattern is then computed using the near-field to far-field transformation on the truncated dataset. The amplitude of the resulting far-field pattern is saved as $A_{2b}$. Next, the error signal is found by calculating the difference between the far-field amplitude of the truncated dataset, $A_{2b}(\theta,\phi)$ and the amplitude of the un-truncated dataset, $A_2$, as

$$Error_9(\theta,\phi) = 20\log_{10}\left|10^{A_2(\theta,\phi)/20} - 10^{A_{2b}(\theta,\phi)/20}\right| \quad (3.3\text{-}14)$$

As the next step the error-to-signal ratio of error term #9 can be computed using

$$Error/S(\theta,\phi)_9 = Error_9(\theta,\phi) - S(\theta,\phi) \quad (3.3\text{-}15)$$

and the associated amplitude uncertainty of $A_1$ due to error term #9 estimated via

$$U_9(\theta,\phi) = \pm 20\log_{10}(1 - 10^{[Error(\theta,\phi)/S(\theta,\phi)_9]/20}) \quad (3.3\text{-}16)$$

### 3.3.10 Error Term #10: Sphere Radius Errors

In order to estimate the amplitude uncertainty due to uncertainty in the value of the measured SNF scan sphere radius, the method proposed in Section 2.5.11 can be used. First, the far-field amplitude from $M_1$ is computed using the measured scan radius to produce the far-field amplitude, $A_1$. Next the value of the measurement radius is changed by a small amount in simulation and the near-field to far-field transformation is performed to produce a far-field pattern containing errors associated with error term #10, $A_{1c}$. This change in the SNF scan sphere radius is simulated and as such does not require any physical setup changes. By comparing the two far-field patterns, one can estimate the impact of small errors in the measured scan radius using

$$Error_{10}(\theta,\phi) = 20\log_{10}\left|10^{A_1(\theta,\phi)/20} - 10^{A_{1c}(\theta,\phi)/20}\right| \quad (3.3\text{-}17)$$

The error-to-signal ratio of error term #10 can be computed using

$$Error/S(\theta,\phi)_{10} = Error_{10}(\theta,\phi) - S(\theta,\phi) \quad (3.3\text{-}18)$$

and the associated amplitude uncertainty of $A_1$ due to error term #10 estimated from

$$U_{10}(\theta,\phi) = \pm 20\log_{10}(1-10^{[Error(\theta,\phi)/S(\theta,\phi)_{10}]/20}) \tag{3.3-19}$$

### 3.3.11 Error Term #11: Sphere Theta/Phi Errors

Section 2.5.11 indicated that this error term includes two distinct sources of error: measurement sphere $\theta/\phi$ axis non-intersection and $\theta/\phi$ axis non-orthogonality. For the purpose of this automated error assessment procedure, only the errors associated with the non-intersection of the measurement spheres $\theta$ and $\phi$ axes will be estimated.

In order to estimate the impact that $\theta/\phi$ axis non-intersection will have on the radiation pattern amplitude of a particular AUT, the near-field to far-field transformation must be completed on measurement data that contains this type of error. Since, as explained in Section 3.2.1, no post-processing is performed on the quoted AUT radiation pattern used for this thesis, the effects of $\theta/\phi$ axis non-intersection errors will be present in $A_1$. Next, the phase correction of expression (2.5-10) in Section 2.5.11 can then be applied to the near-field data in order to correct for the effects of $\theta/\phi$ axis non-intersection errors. After computing the near-field to far-field transformation, the resulting far-field amplitude pattern can be saved as $A_{1d}$. By comparing the two far-field patterns, one can estimate the effects of error term #11 using

$$Error_{11}(\theta,\phi) = 20\log_{10}\left|10^{A_1(\theta,\phi)/20} - 10^{A_{1d}(\theta,\phi)/20}\right| \tag{3.3-20}$$

The error-to-signal ratio of error term #11 can be computed using

$$Error/S(\theta,\phi)_{11} = Error_{11}(\theta,\phi) - S(\theta,\phi) \tag{3.3-21}$$

and the associated amplitude uncertainty of $A_1$ due to error term #11 estimated via

$$U_{11}(\theta,\phi) = \pm 20\log_{10}(1-10^{[Error(\theta,\phi)/S(\theta,\phi)_{11}]/20}) \tag{3.3-22}$$

### 3.3.12 Error Term #12: Higher Order Coupling

In Section 2.5.12, the concept of comparing two scans taken λ/4 apart was discussed as a suitable method to estimate the effects of reactive coupling and multiple reflections between the probe and AUT. Up to this point in the discussion only two measurements have been proposed: the quoted AUT radiation pattern, $M_1$, and the double density scan, $M_2$. Since both of these scans have been acquired at the same probe-to-AUT separation, a new measurement is proposed whereby the probe-to-AUT separation is increased by λ/4 at the lowest test frequency. For reasons that will become clear when the complete list of measurements is presented in Section 3.4, this scan will be saved as $M_6$.

In order to ensure that only the effects of higher order coupling between the probe and AUT are being extracted from this test, all test parameters must be identical to that for the selected scan to which we compare $M_6$ (aside from the probe-to-AUT separation). In order to reduce total acquisition time, it is recommended that $A_6$, the far-field amplitude obtained via $M_6$, be compared to either $A_{2a}$ (far-field pattern computed using the regular density subset of $M_2$), $A_{1a}$ (far-field pattern computed using the 180-Phi subset of $M_1$) or $A_{1b}$ (far-field pattern computed using the 360-Phi subset of $M_1$). For the purposes of this thesis, it will be compared to $A_{2a}$, so that

$$Error_{12}(\theta,\phi) = 20\log_{10}\left|10^{A_{2a}(\theta,\phi)/20} - 10^{A_6(\theta,\phi)/20}\right| \tag{3.3-23}$$

It should be emphasized again that apart from the λ/4 difference in probe-to-AUT separation, all other test parameters must be identical between the two scans. The error-to-signal ratio of error term #12 can be computed as

$$Error/S(\theta,\phi)_{12} = Error_{12}(\theta,\phi) - S(\theta,\phi) \tag{3.3-24}$$

and the associated amplitude uncertainty of $A_1$ due to error term #12 estimated using

$$U_{12}(\theta,\phi) = \pm 20\log_{10}(1 - 10^{[Error(\theta,\phi)/S(\theta,\phi)_{12}]/20}) \tag{3.3-25}$$

### 3.3.13 Error Term #13: Receiver Amplitude Non-Linearity

Using the method proposed in Sction 2.5.13, the effects of receiver amplitude non-linearity can be estimated. To determine this error signal, one must compare the amplitude data of the "truth model", $A_1$, to the pattern resulting from the near-field to far-field transformation of a near-field dataset corrected for error term #13. This pattern will be denoted $A_{1e}$. By comparing the two far-field patterns, one can estimate the effects of error term #13 through use of

$$Error_{13}(\theta,\phi) = 20\log_{10}\left|10^{A_1(\theta,\phi)/20} - 10^{A_{1e}(\theta,\phi)/20}\right| \tag{3.3-26}$$

The error-to-signal ratio of error term #13 can then be computed using

$$Error/S(\theta,\phi)_{13} = Error_{13}(\theta,\phi) - S(\theta,\phi) \tag{3.3-27}$$

and the associated amplitude uncertainty of $A_1$ due to error term #13 estimated as

$$U_{13}(\theta,\phi) = \pm 20\log_{10}(1 - 10^{[Error(\theta,\phi)/S(\theta,\phi)_{13}]/20}) \tag{3.3-28}$$

### 3.3.14 Error Term #14: System Phase Errors

To determine this error signal, one must simply rotate both the AUT's phi axis and the probe's axis in tandem, of course assuming that the probe and AUT remain co-polarized throughout the test. The recorded near-field amplitude is stored as $A_5(\phi)$. After rotating a full $360^\circ$ in $\phi$, the near-field peak-to-peak amplitude is determined and taken to be the uncertainty at all points due to system phase errors caused by imperfections in the SNF rotary joints. It then follows that the associated uncertainty is

$$U_{14}(\theta,\phi) = \max\{A_5(\phi)\} - \min\{A_5(\phi)\} \tag{3.3-29}$$

Which is in fact independent of $(\theta,\phi)$.

### 3.3.15 Error Term #15: Receiver Dynamic Range

Recall from Section 2.5.15 that the error level for this term is simply set to be the negative of the measured on-axis SNR. The on-axis signal-to-noise ratio tells one how high above the noise floor the on-axis AUT pattern amplitude is. The error signal for this term is

$$Error_{15}(\theta,\phi) = -SNR(0,0) \tag{3.3-30}$$

provided it is referenced to a normalized AUT amplitude peak. Next, the error-to-signal ratio of error term #15 can be computed using

$$Error/S(\theta,\phi)_{15} = Error_{15}(\theta,\phi) - [S(\theta,\phi) - \max\{S(\theta,\phi)\}] \tag{3.3-31}$$

and the associated amplitude uncertainty of $A_1$ due to error term #15 estimated from

$$U_{15}(\theta,\phi) = \pm 20\log_{10}(1 - 10^{[Error(\theta,\phi)/S(\theta,\phi)_{15}]/20}) \tag{3.3-32}$$

### 3.3.16 Error Term #16: Room Scattering

In Section 2.5.16, three possible methods for determining the uncertainty due to room scattering were presented.

***A. Possibility #1***

One may wish to compare a scan acquired using a 180-Phi sampling strategy to a scan acquired using a 360-Phi sampling strategy. In order to accomplish this, one may simply extract the two required datasets from the quoted, redundant AUT measurement, $M_1$. Using the expression

$$Error_{16}(\theta,\phi) = 20\log_{10}\left|10^{A_{1f}(\theta,\phi)/20} - 10^{A_{1g}(\theta,\phi)/20}\right| \tag{3.3-33}$$

the first method discussed for estimating the effects of room scattering can be evaluated. Here, $A_{1f}$ refers to the far-field amplitude obtained via the near-field to far-field transformation on the 180-Phi subset of $M_1$. Likewise, $A_{1g}$ refers to the far-field amplitude obtained via the near-field to far-field transformation on the 360-Phi subset of

$M_1$. Recall from Section 2.5.16 that this method is expected to produce grossly over-estimated uncertainty estimations so will not be presented in the results found in Section 4.16.

***B. Possibility #2***

Alternatively, the possibility of comparing a redundant measurement to a 180-Phi measurement was suggested. Again, the 180-Phi dataset may be extracted from $M_1$ and the resulting far-field pattern is denoted $A_{1f}$. The expression

$$Error_{16}(\theta,\phi) = 20\log_{10}\left|10^{A_1(\theta,\phi)/20} - 10^{A_{1f}(\theta,\phi)/20}\right| \tag{3.3-34}$$

can then be used to estimate the effects of room scattering.

***C. Possibility #3***

Finally, the possibility of comparing a redundant measurement to a 360-Phi measurement was suggested. The effects of room scattering using this method can be estimated via

$$Error_{16}(\theta,\phi) = 20\log_{10}\left|10^{A_1(\theta,\phi)/20} - 10^{A_{1g}(\theta,\phi)/20}\right| \tag{3.3-35}$$

$A_{1g}$ again refers to the amplitude resulting from performing the near-field to far-field transformation on the 360-Phi subset of $M_1$.

Once the error signal level has been determined using expression (3.3-33), (3.3-34) or (3.3-35), the error-to-signal ratio of error term #16 can be computed using

$$Error/S(\theta,\phi)_{16} = Error_{16}(\theta,\phi) - S(\theta,\phi) \tag{3.3-36}$$

and the associated amplitude uncertainty of $A_1$ due to error term #16 estimated by applying

$$U_{16}(\theta,\phi) = \pm 20\log_{10}(1 - 10^{[Error(\theta,\phi)/S(\theta,\phi)_{16}]/20}) \tag{3.3-37}$$

### 3.3.17 Error Term #17: Cable Leakage

Recall that the evaluation of this error term requires an identical scan to $M_1$. However, the cable feeding the AUT is disconnected and loaded with 50Ω to determine the leakage level. The error signal then simply becomes the measured pattern of cable radiation. This leakage measurement will be denoted $M_7$, with the resulting "far-field radiation pattern" of the leakage data becoming the error signal due to cable leakage. In other words

$$E_{17}(\theta,\phi) = A_7(\theta,\phi) \tag{3.3-38}$$

The error-to-signal ratio of error term #17 is computed using

$$Error/S(\theta,\phi)_{17} = Error_{17}(\theta,\phi) - S(\theta,\phi) \tag{3.3-39}$$

and the associated amplitude uncertainty of $A_1$ due to error term #17 estimated using

$$U_{17}(\theta,\phi) = \pm 20\log_{10}(1-10^{[Error(\theta,\phi)/S(\theta,\phi)_{17}]/20}) \tag{3.3-40}$$

### 3.3.18 Error Term #18: Repeatability and Random Errors

This error term is evaluated by simply comparing two identical scans, acquired one directly after another. By comparing the two resulting far-field amplitude patterns, one may estimate the effects of random errors and non-repeatability in the measurements. Therefore, two new scans will be proposed as measurements $M_3$ and $M_4$. The sampling strategy, sampling density and other parameters are not of great concern, provided they are consistent between $M_3$ and $M_4$. However, in the interest of reducing overall measurement acquisition time, these measurements will use the Nyquist sampling rate and hence expression (2.5-8), and will use a single sphere sampling strategy. The expression

$$Error_{18}(\theta,\phi) = 20\log_{10}\left|10^{A_3(\theta,\phi)/20} - 10^{A_4(\theta,\phi)/20}\right| \tag{3.3-41}$$

can be used to determine the error signal level due to random errors, where $A_3$ refers to the amplitude pattern computed using measurement $M_3$. Likewise, $A_4$ denotes the far-field amplitude of $M_4$.

The error-to-signal ratio of error term #18 can be computed using

$$Error/S(\theta,\phi)_{18} = Error_{18}(\theta,\phi) - S(\theta,\phi) \tag{3.3-42}$$

and the associated amplitude uncertainty of $A_1$ due to error term #18 estimated via

$$U_{18}(\theta,\phi) = \pm 20\log_{10}(1-10^{[Error(\theta,\phi)/S(\theta,\phi)_{18}]/20}) \tag{3.3-43}$$

## 3.4 MEASUREMENTS NEEDED FOR ERROR TERM EVALUATION

This section has been included to provide a clear and concise summary of exactly what is needed to determine, based on the 18-term error budget, the uncertainty in the amplitude radiation patterns of an AUT in all directions. The flow chart in Figure 3-1 provides a simple pictorial view of the procedure. The clouds in this diargram contain the NIST 18-term sources of error that each measurement is responsible for analysing. The first column in Table 3-2 identifies the seven independent SNF near-field measurements that are required, from which the radiation patterns in the second column are obtained via near-field to far-field transformation. These are used, as described in the preceding section, to determine the overall uncertainty.

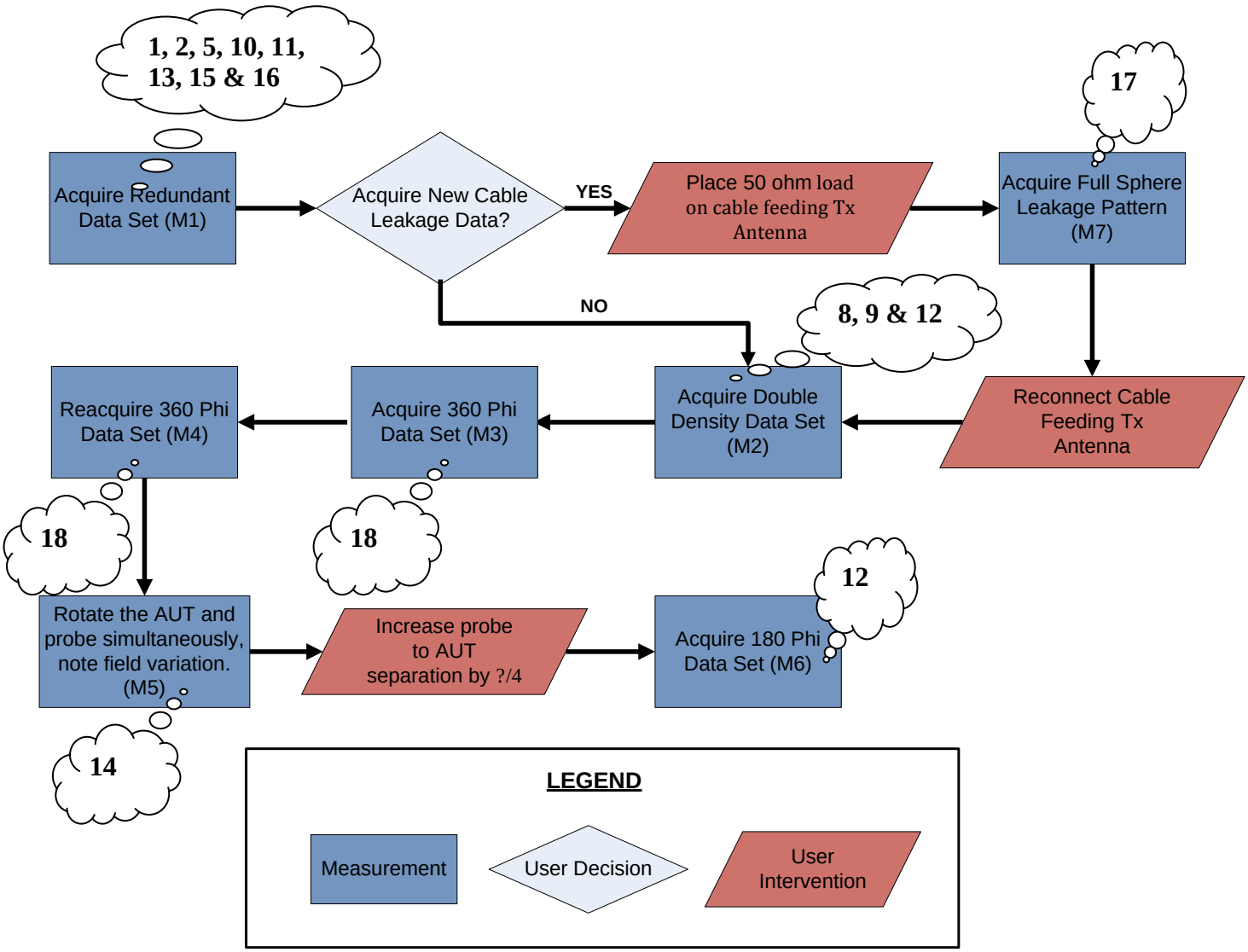


**Figure 3-1: Flow Chart Outlining the Required Set and Ordering of the SNF Measurements Used in this Process**

**Table 3-2: Summary of Required Measurements and Far-Field Amplitude Patterns**

| Meas. | Amp | Sampling Strategy | Scan Speed | Sampling Density | Notes |
|---|---|---|---|---|---|
| $M_1$ | $A_1$ *or* $S$ | Redundant | Slow | Regular | Redundant measurement acquired at slow scan speed. $A_1$ becomes the quoted AUT amplitude pattern. |
| | $A_{1a}$* | Redundant | Regular | Regular | Amplitude pattern resulting from $M_1$ without probe correction applied. |
| | $A_{1b}$* | Redundant | Regular | Regular | Amplitude pattern resulting from $M_1$ after performing the rotation discussed in 3.5.7. |
| | $A_{1c}$* | Redundant | Regular | Regular | Amplitude pattern resulting from $M_1$ with simulated change in the SNF measurement radius. |
| | $A_{1d}$* | Redundant | Regular | Regular | Amplitude pattern resulting from $M_1$ after correcting for $\theta/\phi$ axis non-intersection errors. |
| | $A_{1e}$* | Redundant | Regular | Regular | Amplitude pattern resulting from $M_1$ after correcting for receiver amplitude non-linearity. |
| | $A_{1f}$* | 180-Phi | Regular | Regular | Amplitude pattern resulting from the 180-Phi subset of $M_1$. |
| | $A_{1g}$* | 360-Phi | Regular | Regular | Amplitude pattern resulting from the 360-Phi subset of $M_1$. |
| $M_2$ | $A_2$ | 180-Phi | Regular | Double | Amplitude pattern of the double density measurement, $M_2$. |
| | $A_{2a}$* | 180-Phi | Regular | Regular | Amplitude pattern resulting from the regular density subset of $M_2$. |
| | $A_{2b}$* | 180-Phi** | Regular | Double | Amplitude pattern resulting from the truncated version of $M_2$. |
| $M_3$ | $A_3$ | 360-Phi | Regular | Regular | Amplitude pattern of the first of two repeatability scans, $M_3$. |
| $M_4$ | $A_4$ | 360-Phi | Regular | Regular | Amplitude pattern of the second of two repeatability scans, $M_4$. |
| $M_5$† | $A_5$† | N/A† | Stop Motion† | Double† | Simultaneous rotation of AUT's phi axis and probe, remaining co-polarized throughout the scan. The peak-to-peak variation is noted. |
| $M_6$ | $A_6$ | 180-Phi | Regular | Regular | Amplitude pattern of $M_6$, acquired with a λ/4 increase in probe-to-AUT separation. |
| $M_7$ | $A_7$ | Any | Regular | Regular | Amplitude pattern of the leakage measurement, $M_7$. |

## 3.5 AUTOMATION OF THE ASSESSMENT PROCESS

Software has been developed to automate the error assessment process. It consists of two parts:

### *A. Acquisition Software*

The first part manages the automated data acquisition to gather all the data (that is, carry out measurements M1 through M7 defined in Table 3-2 in the order outlined in the flow chart of Figure 3-1) needed for the uncertainty assessment. The AUT is mounted in the SNF chamber and the standard control software for the SNF system is initiated.

### *B. Processing Software*

The second part carries out the automated processing of the measured data to arrive at the actual uncertainty estimates, as well output the tabular and graphical presentation thereof. Figure 3-2 shows the interface developed specifically for the work of this thesis. Once all automated measurements have been completed as outlined in the flow chart of Figure 3-1, the error assessment operator is prompted with this interface. This piece of software allows one to visualize the uncertainty associated with a particular antenna's radiation pattern in numerous ways, as will be shown in Chapter 4.

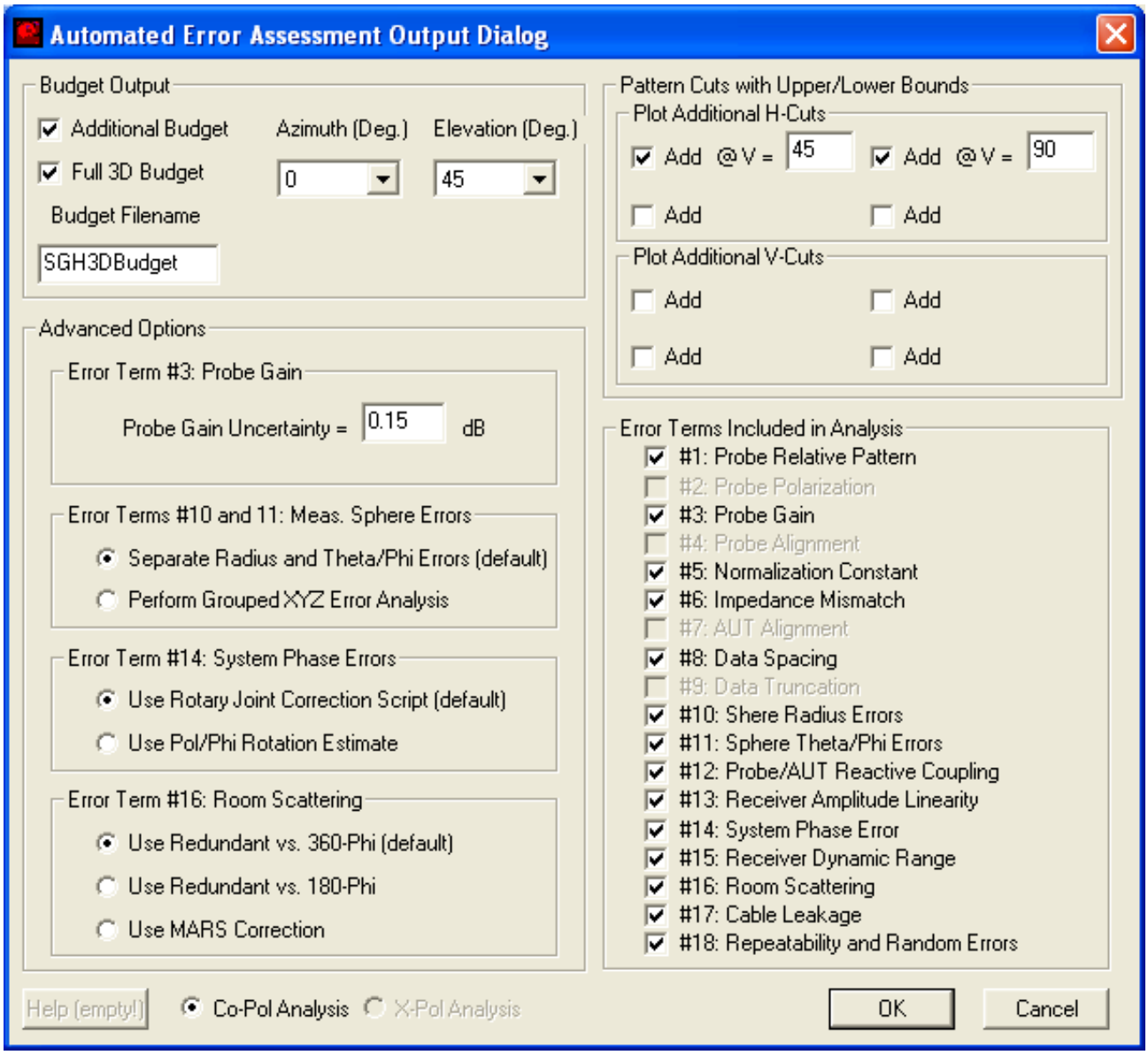


**Figure 3-2: Automated Error Assessment User Interface Developed**

## 3.6 CONCLUDING REMARKS AND NEXT STEPS

In Section 3.2, the reader was presented with a set of definitions and terminology (eg. what is meant by the "quoted AUT pattern" in the error assessment context) crucial to full understanding of how one determines an error signal level for a particular source of error from appropriate measurements. Although the expressions involved are straightforward, they are often not explicitly stated in the literature. Next, in Section 3.3, a set of specific measurements (some of which were already extant, and others which are new) was identified that can be carried out automatically on both an AUT and the test set-up, and used to evaluate the uncertainty contributed by the above error terms. The reasoning behind the selection of these measurements is provided. The order of the measurements has been optimized (and presented in the form of a flow chart detailing what actions are required in an automated process) to minimize the overall time to complete an error assessment. This has been achieved by so defining the set of required measurements that several data sets can simply be extracted as subsets of these key measurements and so need not be separately acquired. The correct ordering of the specific measurements was especially important to permit resumption of data set acquisition should any single step prove to be temporarily problematic. Expressions to compute the uncertainties associated with each error term are also given. Complete details of these measurements, and which error terms they are used evaluate, are provided in tabular form in Section 3.4. This allows the reader to easily see how many measurements are needed for all the necessary data to be acquired, what the measurement settings are, and the type of post-processing required to fully quantify all uncertainty contributions.

Now that the foundation for an automated error assessment has been laid, the process must be tested and verified on a set of antennas. Table 3-3 below identifies the four antennas used to test this process in the 7.3 x 4.9 x 3.6 m anechoic chamber at the main antenna test facilities of the Canadian Space Agency in Ottawa. The antennas of Table 3-3 were chosen so that a mix of directivities and operating frequencies could be used to validate this process.

**Table 3-3: Antennas used to Validate this Process at the Canadian Space Agency**

| AUT | Frequency (GHz) | Max. Directivity (dBi) |
|---|---|---|
| Standard Gain Horn | 1.71 | 14.5 |
| Microstrip Patch | 5.50 | 7.5 |
| Isoflux Horn | 14.25 | 6.9 |
| Slotted Waveguide Array | 9.24 | 28.0 |

Figure 3-3 shows the mounting of the standard gain horn as it was installed in the test range and Figure 3-4 shows the $\phi = 0^{\circ}$ azimuth cut of the quoted AUT radiation pattern for this antenna. This antenna was chosen for testing due to its low operating frequency and popularity in industry.

Next, Figure 3-5 is a photograph of the microstrip patch antenna as it was mounted in the SNF chamber at the Canadian Space Agency's test facilities. This antenna was chosen for its low directivity and 5.5 GHz operating frequency. Figure 3-6 shows the amplitude of the quoted AUT radiation pattern of this antenna. A low gain antenna such as this radiates (or receives) a significant amount of energy across a wide angular sector. Since this antenna has a very broad pattern, the effects of room scattering were found to be severe and is the reason for the radiation pattern's appearance. As discussed in Section 3.2.1, the quoted AUT radiation pattern will not attempt to correct for the various sources of error, but will instead be used to identify them. The radiation pattern of Figure 3-11 was obtained after correcting the same SNF data for the effects of room scattering using the method proposed in [2]. This has been included for the benefit of the reader.

Figure 3-7 shows the X-band slotted waveguide array which was used a high directivity test case while Figure 3-8 shows the $\phi = 0^{\circ}$ azimuth cut of the quoted AUT radiation pattern for this antenna.

Finally, the last antenna used to test this process was the isoflux horn shown in Figure 3-9. This antenna was chosen for its shaped pattern, as will be shown shortly. After determining the far-field pattern from the data acquired using measurement $M_1$ for this

antenna, one finds that the effects of $\theta/\phi$-axis non-intersection had a major impact on the amplitude pattern, which is shown in Figure 3-10 (and is not quite the expected pattern). By correcting for these imperfections in the measurement sphere using the method proposed in Section 2.5.11, the far-field pattern of Figure 3-12 was obtained, which is the correct (and expected) pattern. Again, this figure was included for the benefit of the reader. In the error assessment for this antenna we will not use the corrected data, for the same reasons given for the microstrip patch.

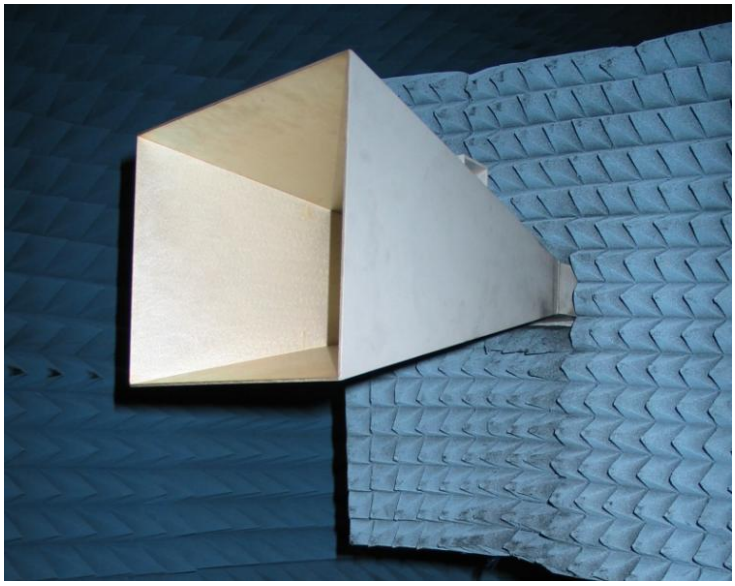

**Figure 3-3: Image of the EMCO 3160 SGH Mounted in the SNF Range**

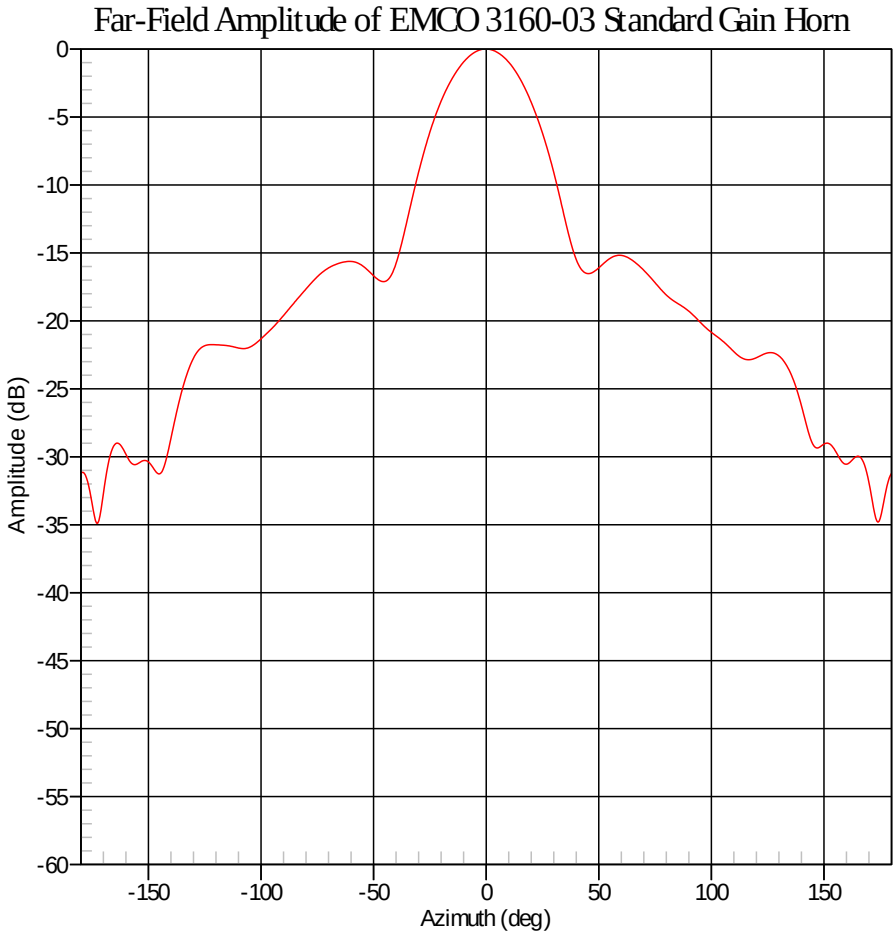


**Figure 3-4: Far-Field $\phi = 0^{\circ}$ Azimuth – Cut of the EMCO Standard Gain Horn**

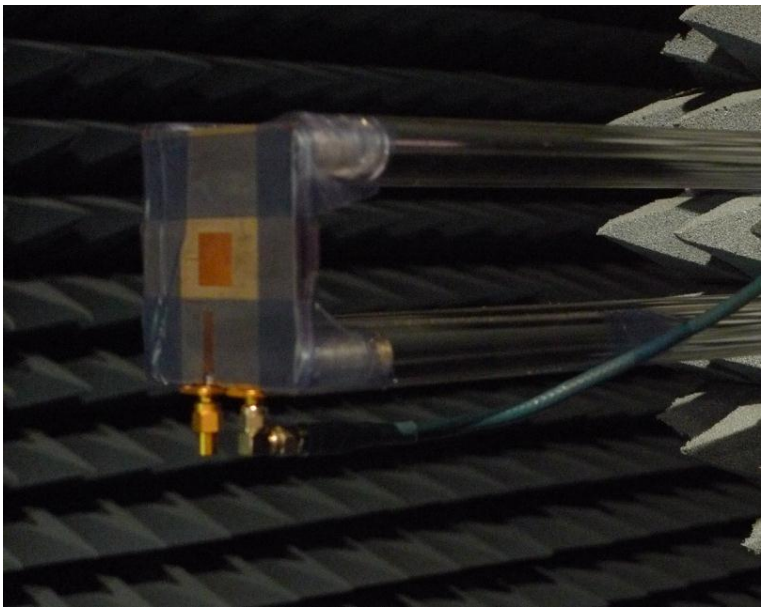

**Figure 3.5: Image of the Microstrip Patch Antenna Mounted in the SNF Range (After [6])**

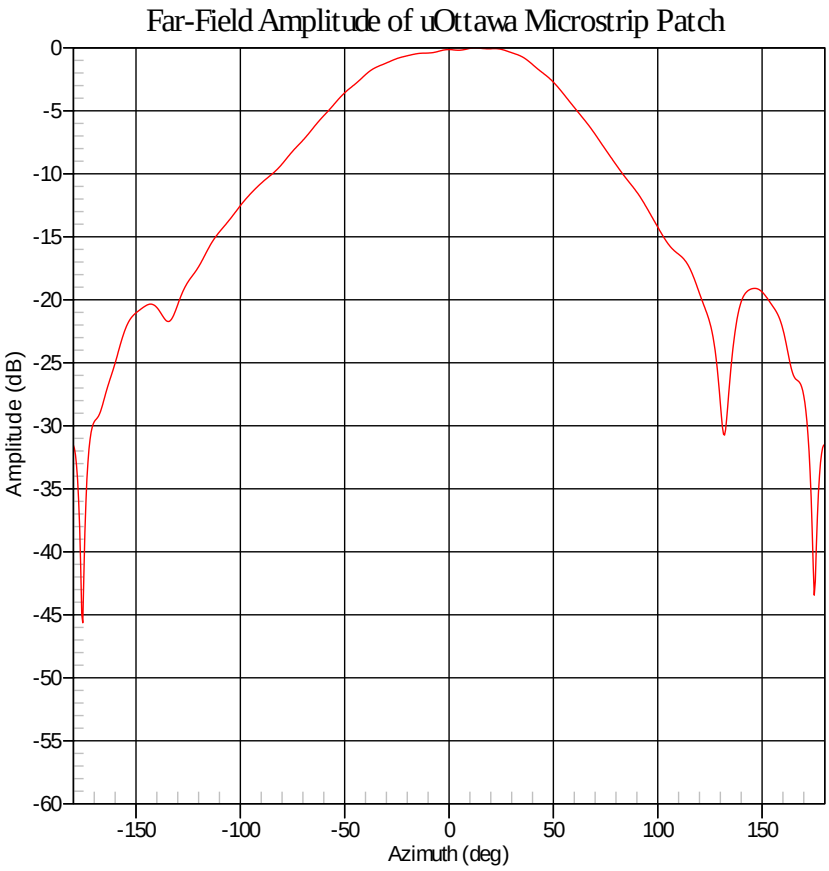


**Figure 3-6: Far-Field $\phi = 0^{\circ}$ Azimuth – Cut of the Microstrip Patch Antenna**

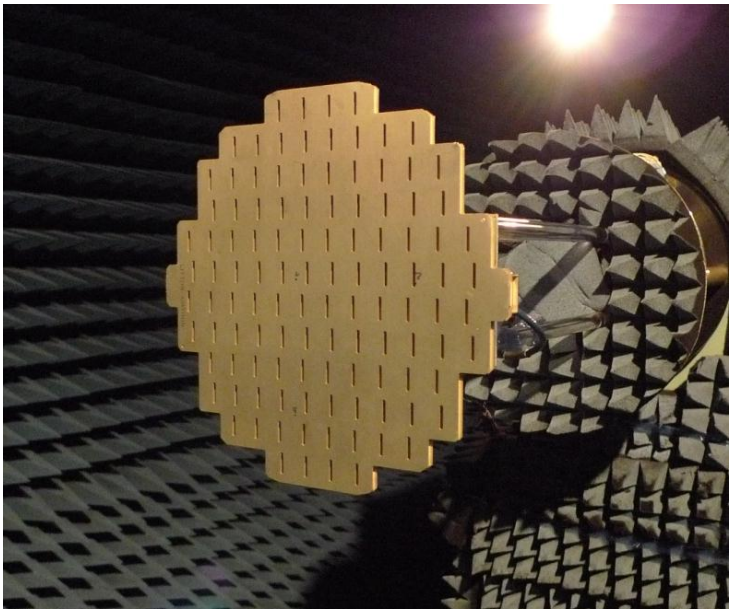

**Figure 3-7: Image of the Slotted Waveguide Array Mounted in the SNF Range**

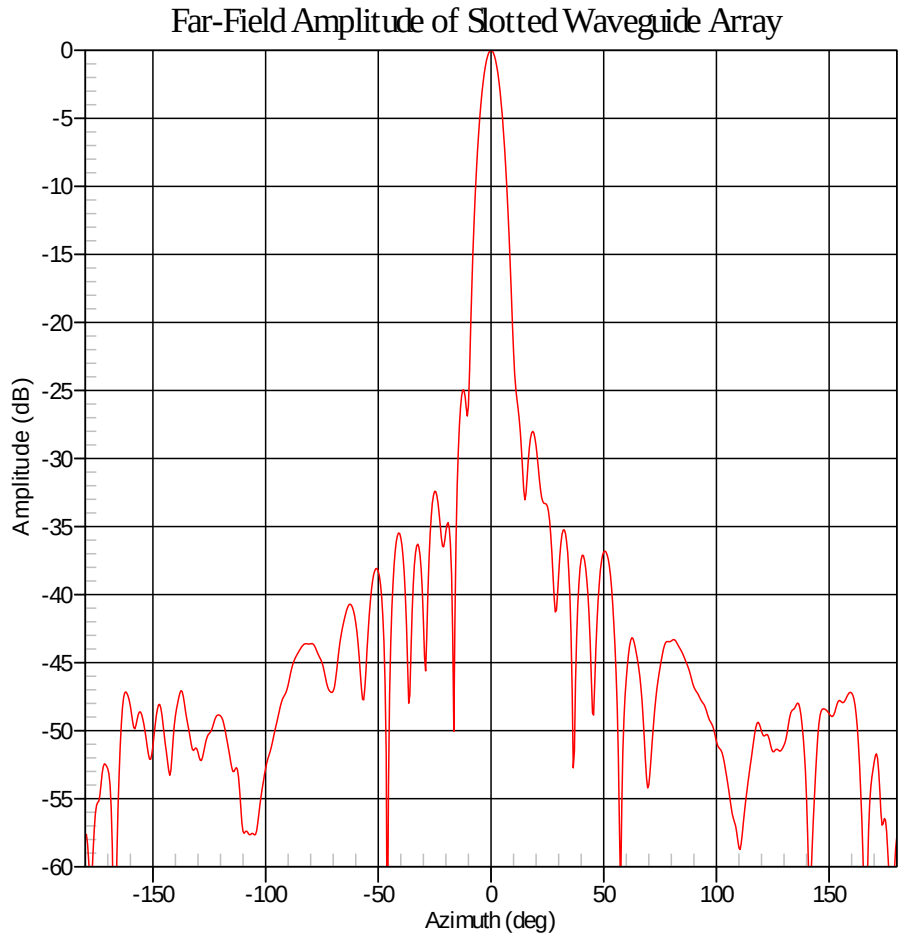


**Figure 3-8: Far-Field $\phi = 0^{\circ}$ Azimuth – Cut of the Slotted Waveguide Array**

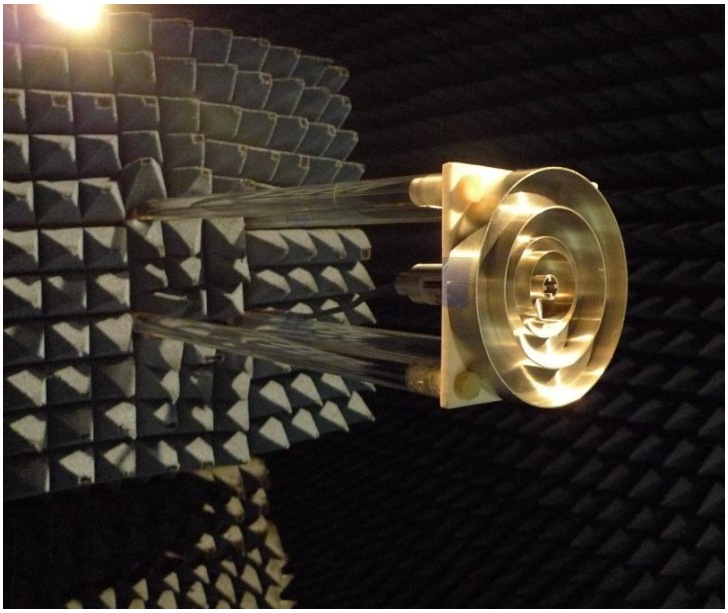

**Figure 3-9: Image of the Isoflux Horn Mounted in the SNF Range**

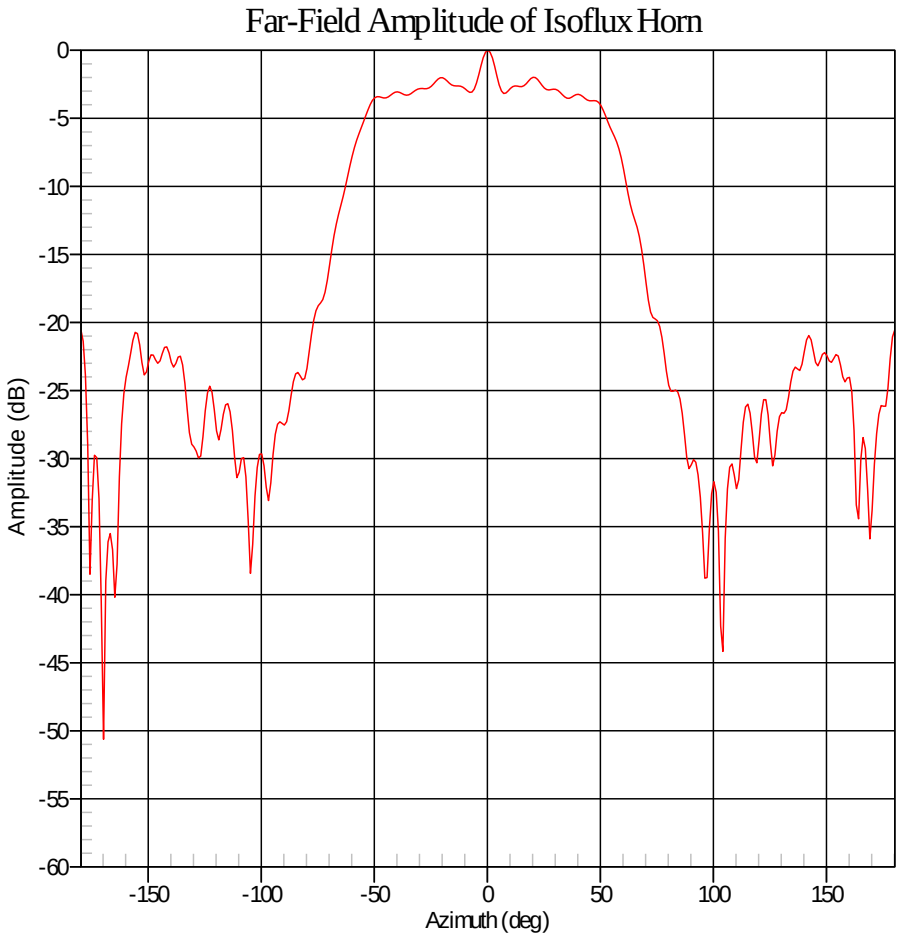


**Figure 3-10: Far-Field $\phi = 0^{\circ}$ Azimuth – Cut of the Isoflux Horn**

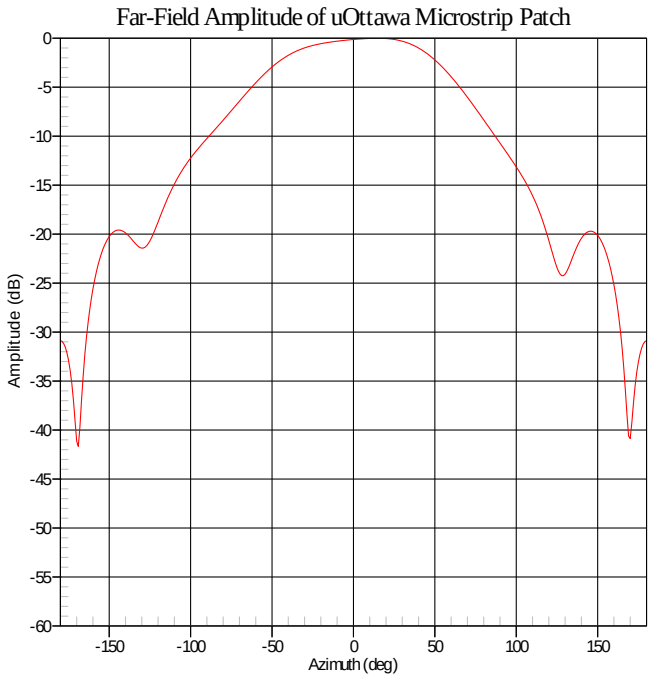


**Figure 3-11: Far-Field $\phi = 0^\circ$ Azimuth – Cut of the Microstrip Patch after Correcting for the Effects of Room Scattering**

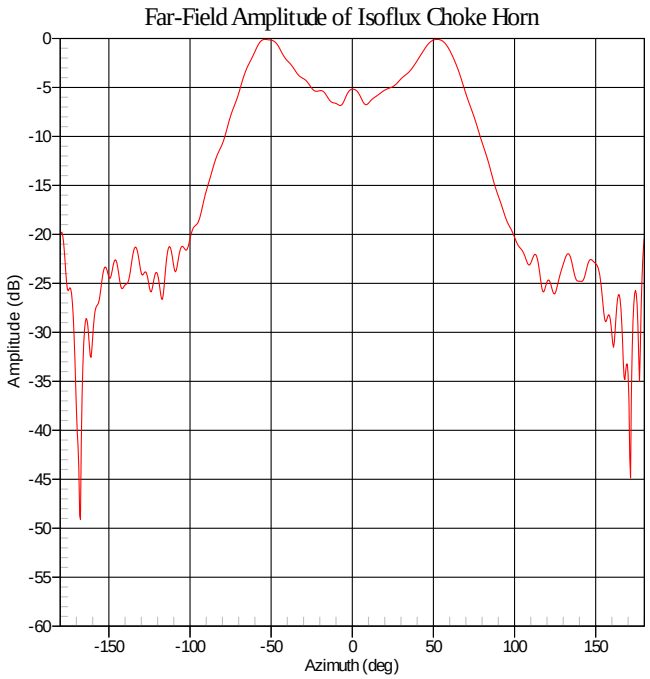


**Figure 3-12: Far-Field $\phi = 0^\circ$ Azimuth – Cut of the Isoflux Horn after Correcting for the Effects of $\theta / \phi$-axis Non-Intersection**

In the chapter that follows each section number corresponds to the numbering of the associated error term in Table 3-1. As such, Chapter 4 will begin by immediately presenting measurement results rather than the usual introductory statements, except for a brief comment on the formatting to be used for the figured in Chapter 4. This is the reason the four AUTs have already been introduced in the present section.

## 3.7 REFERENCES FOR CHAPTER 3


1. G. Hindman, A. Newell, "Simplified Spherical Near-Field Accuracy Assessment", Proc. Antenna Measurement Techniques Association (AMTA) Annual Symp., 2006. *(CD-Rom)*
2. G. Hindman, A. Newell, "Mathematical Absorber Reflection Suppression (MARS) for Anechoic Chamber Evaluation and Improvement", Proc. Antenna Measurement Techniques Association (AMTA) Annual Symp., 2008. *(CD-Rom)*
3. Near-Field Systems Inc.,, "*NSI 2000 Operating Manual*", May 2005.
4. G. Hindman, Nearfield Systems Inc., 19730 Magellan Dr., Torrance, CA, 90502, USA. *Private Communication*.
5. *"What is Accuracy"*, Arbiter Systems, Inc., 1324 Vendels Circle, Ste 121, Paso Robles, CA, 93446, USA.
6. I. Acimovic, D. A. McNamara & A. Petosa, "Dual- Polarized Microstrip Patch Planar Array Antennas with Improved Port-to-Port Isolation", *IEEE Trans. Antennas & Propagation*, Vol.56, No.11, pp.3433-3439, Nov. 2008.
7. D. J. van Rensburg, (2010, Nov), *"Correcting for SNF Axis Non-Intersection Errors"*, NSI, Private Communication.

# CHAPTER 4: Implementation of the Error Assessment Procedure

We next use the automation software of Section 3.5 with each of the four antennas in turn. There is a large amount of data to presented in this chapter, and so it is necessary to streamline its presentation in such a way that the reader can easily navigate to some desired piece of information. We have therefore formatted it so that the first eighteen sections, namely Section 4.1 through Section 4.18, separately deal with each of the terms in the 18-term error budget. Thus Section 4.xx presents results for, and discusses, error term #xx. In each such section the measurement uncertainty results (as output by the automated error assessment process) are presented, for the specific error term, for all four of the antennas identified in Section 3.5. In each section the plots associated with these four antennas are first simply set down in four sub-sections (one for each antenna type), followed by a fifth sub-section that discusses the aforementioned data plots. It is done in this same order in all of the eighteen sections. In practice one need not examine the uncertainties for each individual error term as will be done here. You could run the automated error assessment of the AUT, and then obtain and quote the accumulated uncertainty information. However, even in practice the examination of the individual uncertainties is useful because it allows one to identify which aspects of the measurement setup are responsible for most of the overall uncertainty value. So this can help identify problems with the setup itself. Finally, Section 4.19 describes the accumulated uncertainty assessments and their presentation.

## 4.1 ERROR TERM #1: PROBE RELATIVE PATTERN

### 4.1.1 Standard Gain Horn

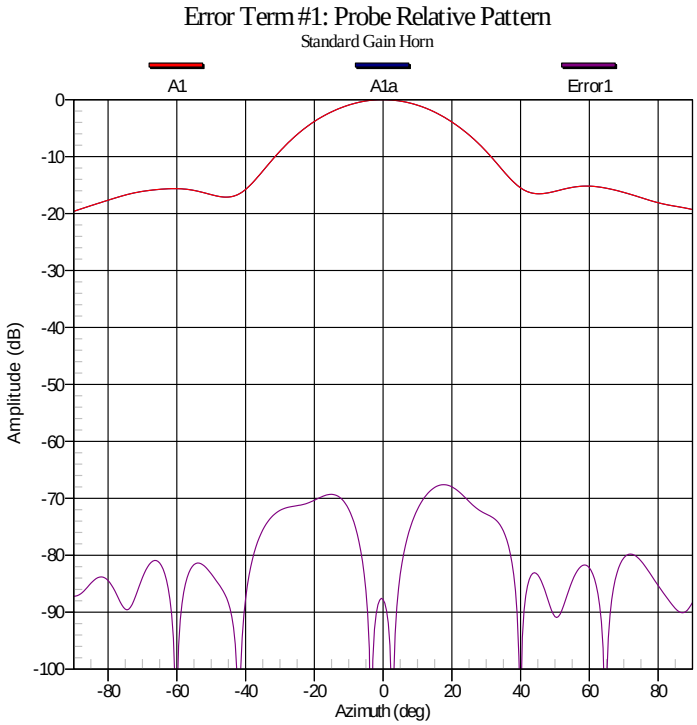


**Figure 4-1: Evaluation of Error Term #1 for the Standard Gain Horn**

### 4.1.2 Microstrip Patch

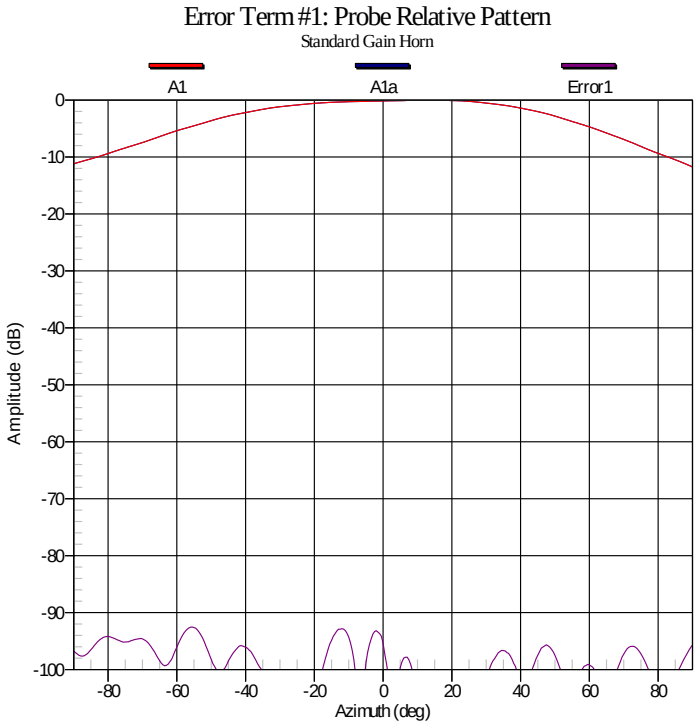


**Figure 4-2: Evaluation of Error Term #1 for the Microstrip Patch**

### 4.1.3 Slotted Waveguide Array

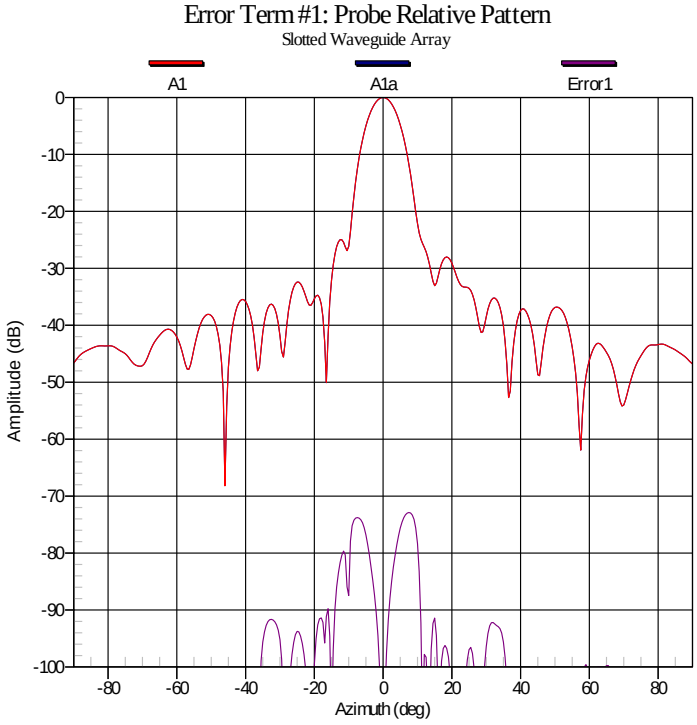


**Figure 4-3: Evaluation of Error Term #1 for the Slotted Waveguide Array**

### 4.1.4 Isoflux Horn

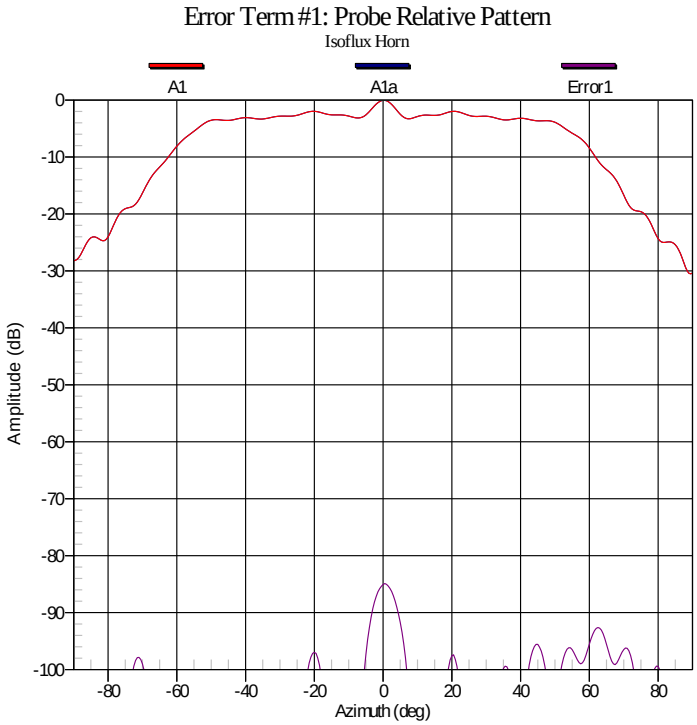


**Figure 4-4: Evaluation of Error Term #1 for the Isoflux Horn**

### 4.1.5 Discussion of Error Term #1

Recall from Section 2.5.1 that this error term is estimated by comparing far-field patterns computed from the same SNF measurement with and without applying probe correction. It was also stated that while the method employed will likely over-estimate the amplitude uncertainty due to error term #1, the resulting uncertainty will still be negligible with respect to the final uncertainty budget. Figures 4-1 through 4-4 show the resulting error signal due to error term #1 using the evaluation method outlined in Section 3.3.1. As expected, the error signal is sufficiently low and will therefore introduce a negligible amplitude uncertainty into the quoted AUT radiation pattern.

For the case of the evaluation of error term #1 for the isoflux antenna (Figure 4-4), one should recall that while the shape of the quoted pattern does not match the "expected pattern" for this antenna, this is being done in the interest of identifying errors, rather than minimizing them. This was explained in Section 3.5.

## 4.2 ERROR TERM #2: PROBE POLARIZATION

### 4.2.1 Standard Gain Horn

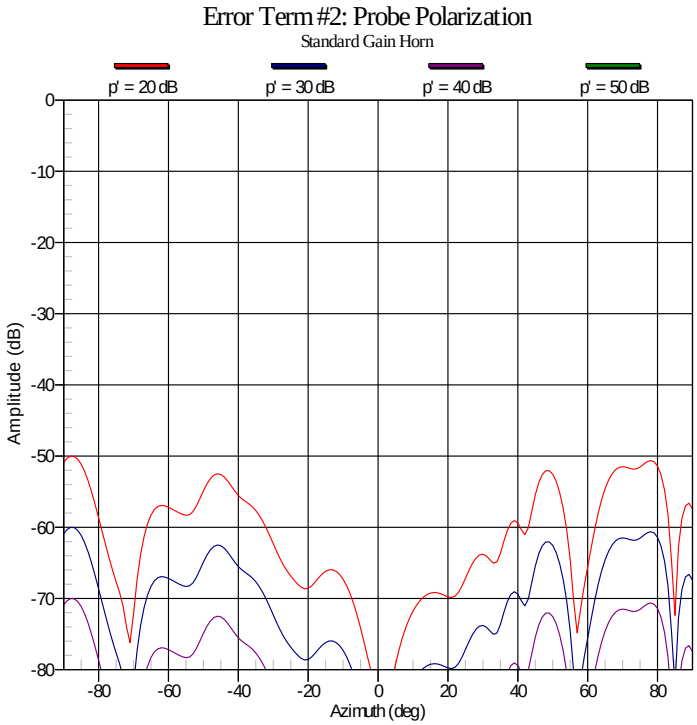


**Figure 4-5: Error-to-Signal Evaluation of Error Term #2 for the SGH**

### 4.2.2 Microstrip Patch

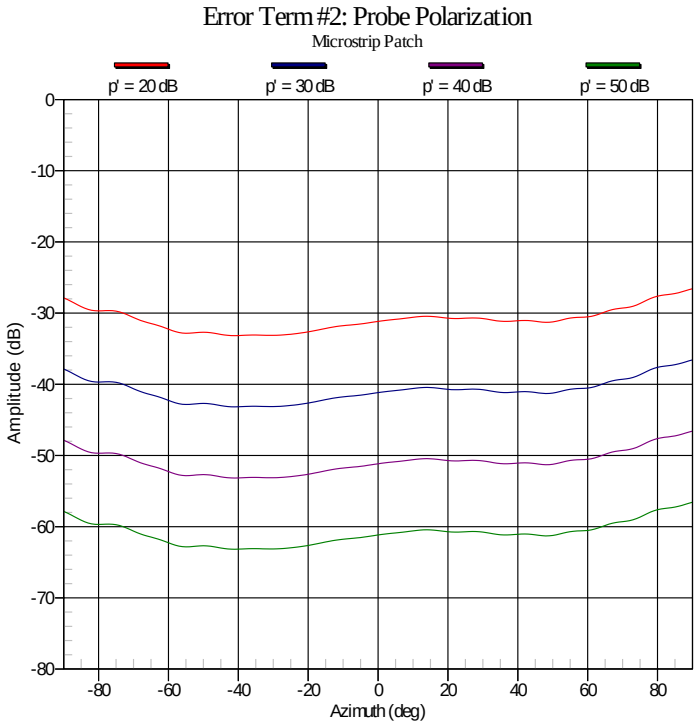


**Figure 4-6: Error-to-Signal Evaluation of Error Term #2 for the Microstrip Patch**

### 4.2.3 Slotted Waveguide Array

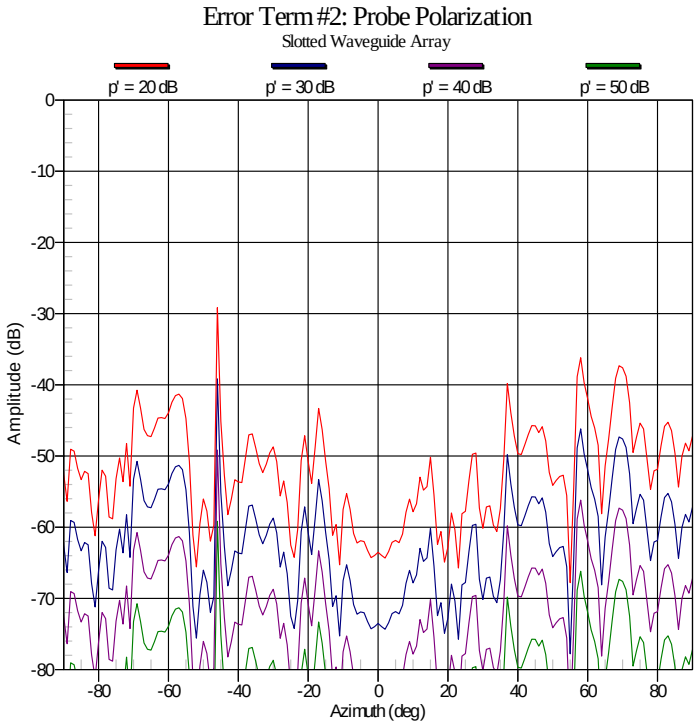


**Figure 4-7: Error-to-Signal Evaluation of Error Term #2 for the Slotted Waveguide Array**

### 4.2.4 Isoflux Horn

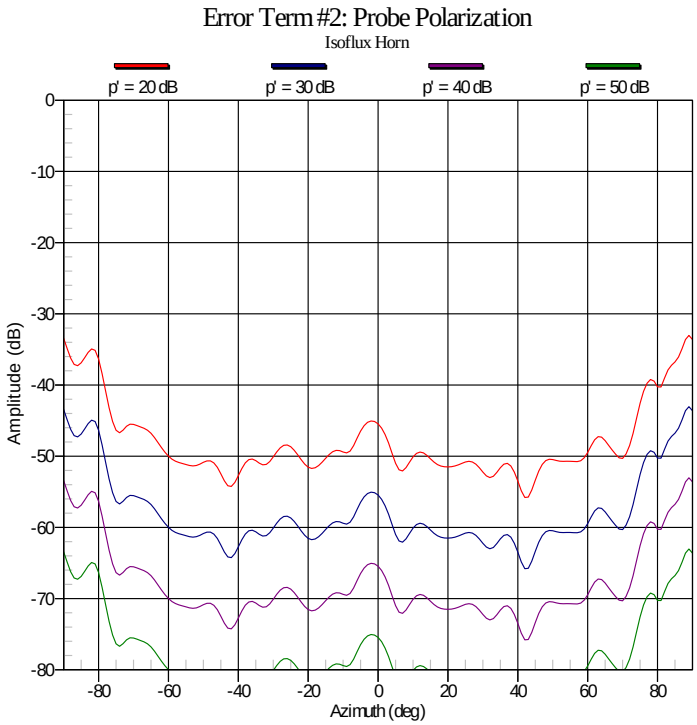


**Figure 4-8: Error-to-Signal Evaluation of Error Term #2 for the Isoflux Horn**

### 4.2.5 Discussion of Error Term #2

In Sections 2.5.2 and 3.3.2 the reader was presented with an equation used to estimate the effects of the non-zero cross-polarization level of the measurement probe used for data acquisition. In order to analyze the effects of this error term, different co-to-cross polarization ratios for the acquisition probe were simulated to determine the effects on the resulting far-field pattern.

Figure 4-5 above shows the error-to-signal ratio introduced to the SGH's far-field pattern for four different probe co-to-cross polarization levels namely $p'(\theta,\phi)$ = [20 dB, 30 dB, 40 dB, 50 dB]. It should be noted here that while the co-to-cross polarization level of the probe will not remain constant for all $(\theta,\phi)$ values in practice, the results presented above assume constant $p'(\theta,\phi)$ for all $(\theta,\phi)$. In reality, one expects a high co-to-cross polarization ratio in the cardinal cuts with decreasing polarization purity away from the cardinal cuts, as with most open waveguide or horn antennas [1]. For the purpose of this thesis, the high co-to-cross polarization ratio of the cardinal cuts will be used since results are only shown for the cardinal cuts of the antennas discussed.

Figures 4-6, 4-7 and 4-8 show the same error-to-signal calculations as outlined above for the microstrip patch, slotted waveguide array and isoflux horn, respectively. The resulting amplitude uncertainty appears to be mostly negligible, except for the microstrip patch. Since the microstrip patch antenna had a lower co-to-cross polarization ratio than the other antennas tested, expression (3.3-4) will yield a much higher amplitude uncertainty in the resulting far-field pattern for the patch. In the final uncertainty budgets presented in the later sections of this chapter, the worst case polarization ratio of the probe will be used, namely $p'(\theta,\phi)$ = 20 dB.

## 4.3 ERROR TERM #3: PROBE GAIN

In Section 3.3.3, it was stated that the uncertainty associated with the near-field probe's gain is typically set by the error assessment operator. For the results shown in this thesis, a probe gain uncertainty of 0.15 dB was chosen. This assumes that the probes used for all measurements presented here have been calibrated not long before their use. Recall that this error term applies to gain measurements only, and so will not be included in general pattern uncertainty budgets in Section 4.19.2.

## 4.4 ERROR TERM #4: PROBE ALIGNMENT

Recall from Sections 2.5.4 and 3.3.4 that this error term will be listed as "not applicable" for the uncertainty budgets presented in this thesis.

## 4.5 ERROR TERM #5: NORMALIZATION CONSTANT

In Section 2.5.5 and 3.3.5, a method for estimating the amplitude uncertainty associated with error term #5 was presented. Table 4-1 summarizes the computed uncertainty due to this source of error. Recall that if one finds the values obtained using this method too optimistic, the manual method proposed in Section 3.3.5 may be used. However, in the interest of automation and for the purpose of this thesis, the results summarized below will be used in the final error budgets.

**Table 4-1: Recorded Amplitude Change for Error Term #5**

| AUT | Amplitude Change (dB) |
|---|---|
| Standard Gain Horn | 0.03 |
| Isoflux Horn | 0.07 |
| Slotted Waveguide Array | 0.16 |
| Microstrip Patch | 0.05 |

## 4.6 ERROR TERM #6: AUT/SGH IMPEDANCE MISMATCH

Since the input reflection coefficients were not measured for the AUT, SGH and cable network, simulated values will be used to estimate this error term using (2.5-6). The results of Table 4-2 show typical amplitude values for the three reflection coefficients

required by (2.5-6). The phases were chosen arbitrarily to simulate an uncertainty for this error term. Using (2.5-6) yields a gain uncertainty of roughly 0.06 dB due to error term #6. This will be the case for all four antennas tested here.

**Table 4-2: Simulated Input Reflection Coefficients for the AUT, SGH and Generator**

| $\Gamma_{SGH}$ [Amp/Phase] | $\Gamma_{AUT}$ [Amp/Phase] | $\Gamma_{GEN}$ [Amp/Phase] |
|---|---|---|
| **-20 dB/0°** | **-20 dB/180°** | **-30 dB/0°** |

## 4.7 ERROR TERM #7: AUT ALIGNMENT

Recall from Sections 2.5.7 and 3.3.7 that this error term will be listed as "not applicable" for the uncertainty budgets presented in this thesis.

## 4.8 ERROR TERM #8: NEAR-FIELD SAMPLING DENSITY

### 4.8.1 Standard Gain Horn

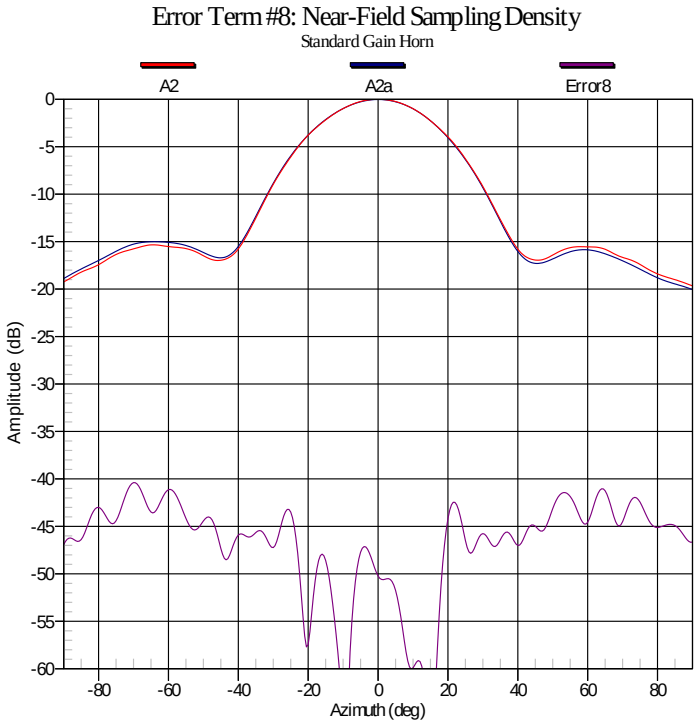


**Figure 4-9: Evaluation of Error Term #8 for the Standard Gain Horn**

### 4.8.2 Microstrip Patch

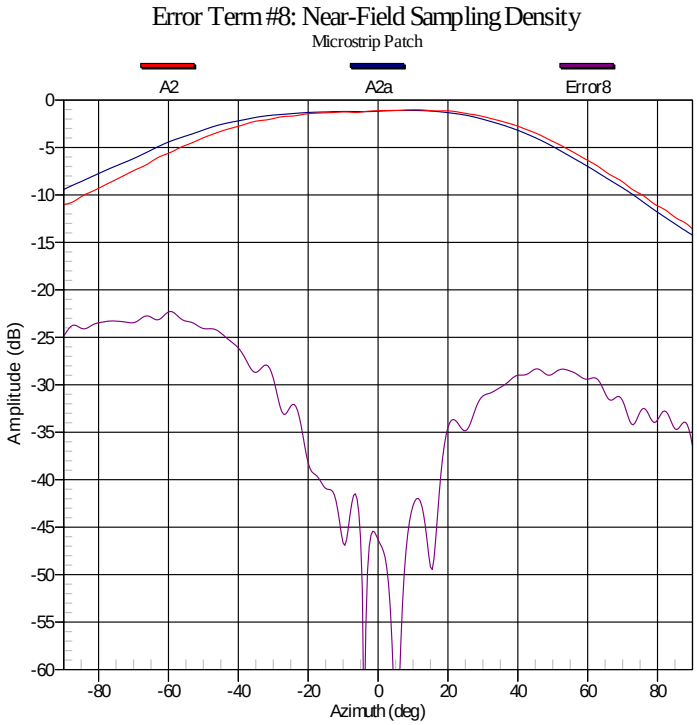


**Figure 4-10: Evaluation of Error Term #8 for the Microstrip Patch**

### 4.8.3 Slotted Waveguide Array

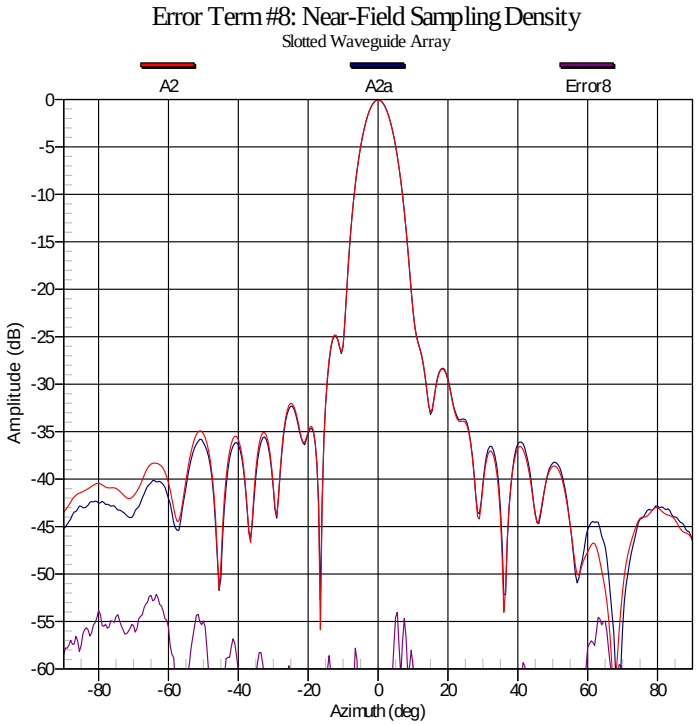


**Figure 4-11: Evaluation of Error Term #8 for the Slotted Waveguide Array**

### 4.8.4 Isoflux Horn

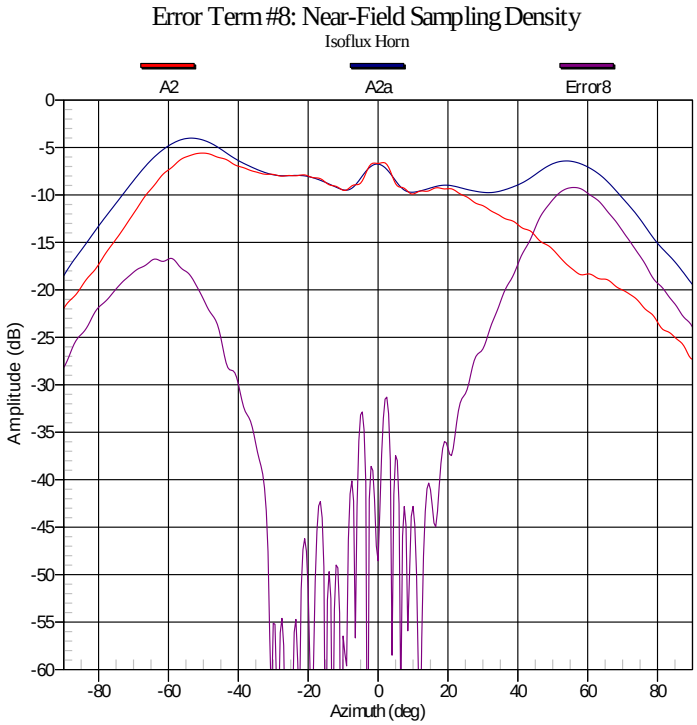


**Figure 4-12: Evaluation of Error Term #8 for the Isoflux Horn**

### 4.8.5 Discussion of Error Term #8

In order to estimate the amplitude errors introduced into the final, quoted AUT radiation pattern due to the finite number of sampling points used in the near-field measurement one may use the method proposed in Section 3.3.8. Namely, the far-field pattern obtained from a double density measurement, $A_2$, can be compared to the far-field pattern calculated by performing the near-field to far-field transformation using the regular density subset of that measurement, $A_{2a}$. When performing the double density measurement using the acquisition software, the value of $r_0$ from (2.5-7) must be increased in order to update the number of spherical modes used in the near-field to far-field transformation. This is a "limitation" imposed on the error assessment process by the particular software used in performing the transformation, rather than a fundamental one. By increasing the value of $r_0$, one is effectively “telling” the transformation software that the antenna has increased in size. In reality, $r_0$ will now include the AUT as well as parts of the mounting and support structures used to hold it in place.

Figure 4-9 above shows the estimated error signal that arises when performing the comparison discussed above for the standard gain horn. While the error level produced in the region of the AUT's main beam is fairly low, it tends to increase near the SGH's sidelobes. Since the value of $r_0$ has been increased, these increased error levels may be due to general scattering introduced by the SGH's mounting structure. A similar discussion can be used to explain the significant error signal resulting from this analysis for the microstrip patch, as shown in Figure 4-10.

For the high gain slotted waveguide array, the effects of increasing $r_0$ are less evident since it will radiate (or receive) less effectively away from its main beam, as shown in Figure 4-11. Therefore, any small amplitude scattering from its support structure will not dominate this error term.

Finally, Figure 4-12 shows the results of this analysis for the isoflux horn. Similar to the large errors introduced in the microstrip patch's far-field pattern, it appears that the effects of general scattering due to an over-sized $r_0$ seem to swamp this error term. By increasing the sampling density (and therefore increasing $r_0$), the general scattering from the isoflux's mounting structure appears to heavily influence the resulting far-field pattern. However, after performing this same analysis on a data set that has been previously corrected to compensate for error term #11, the results of Figure 4-13 are found. Therefore, one can conclude that the method of evaluation for this error term can be affected by $\theta / \phi$-axis non-intersection errors. Care should be taken to minimize these effects as they dominate many error terms. Since the isoflux antenna has large contributions from several of the error terms, final results for this antenna will be presented using the standard set of tests outlined in Section 3.4, without compensation. Additionally, an attempt will be made in Section 4.19.1 to compensate for various error terms to reduce overall pattern uncertainty. As such, we will continue presenting results using uncompensated data for the time being.

Since the error levels estimated using this procedure are not overwhelming (with the exception of the isoflux antenna), the results will be included in the final error budget in Section 4.19.

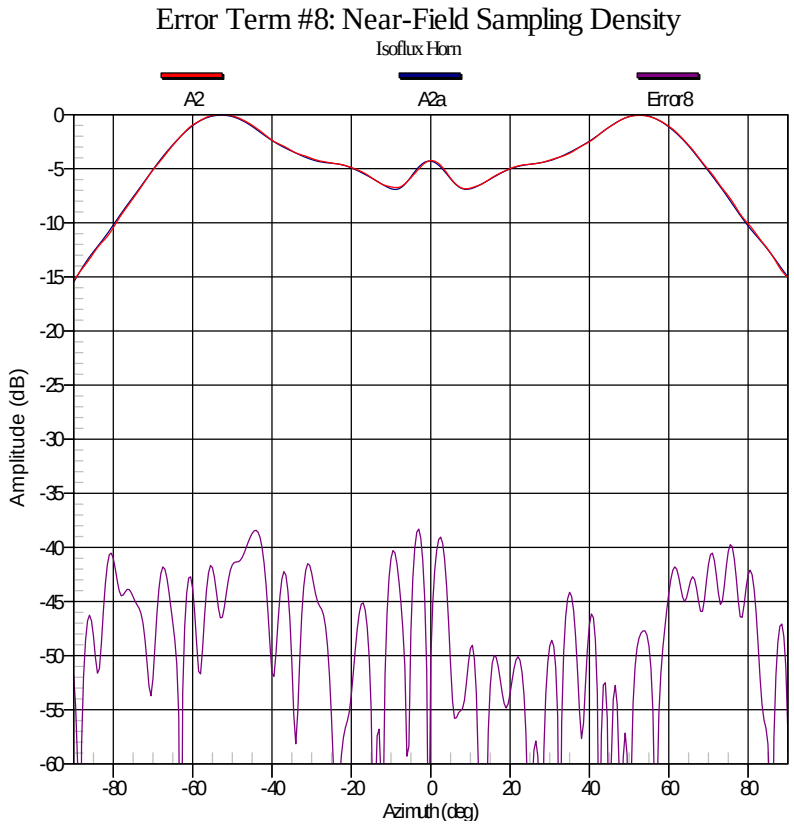


**Figure 4-13: Evaluation of Error Term #8 for the Isoflux Horn After Correcting for $\theta$ / $\phi$-Axis Non-Intersection Errors in $A_2$**

## 4.9 ERROR TERM #9: NEAR-FIELD MEASUREMENT TRUNCATION

### 4.9.1 Standard Gain Horn

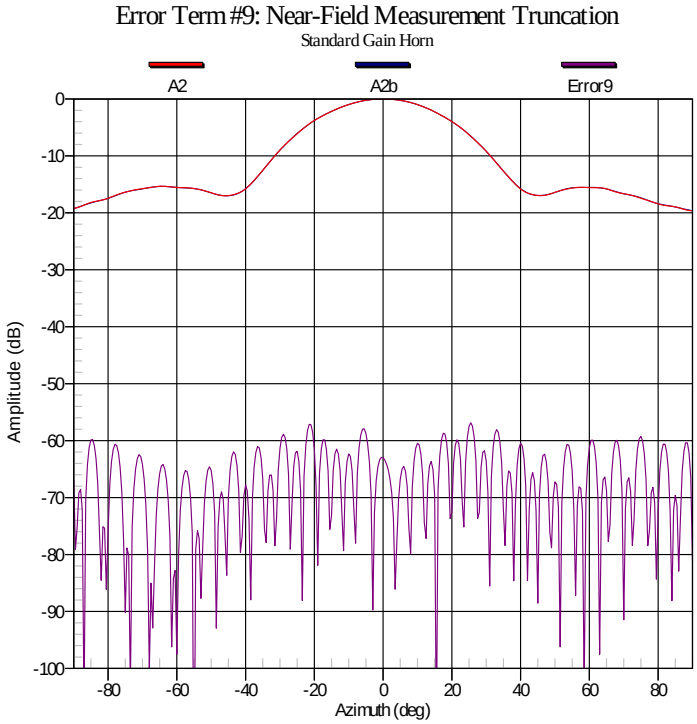


**Figure 4-14: Evaluation of Error Term #9 for the Standard Gain Horn with 12.5% Truncation in the Near-Field θ-Span**

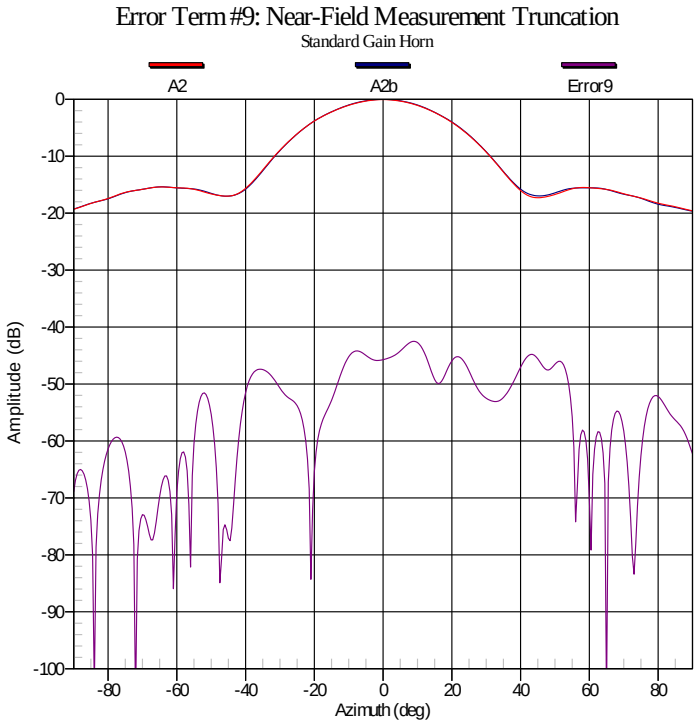


**Figure 4-15: Evaluation of Error Term #9 for the Standard Gain Horn with 25% Truncation in the Near-Field θ-Span**

### 4.9.2 Microstrip Patch

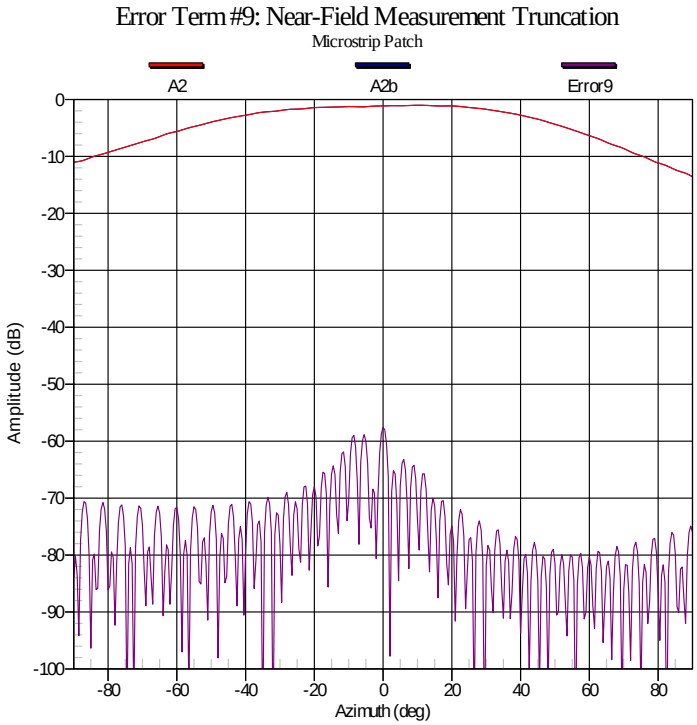


**Figure 4-16: Evaluation of Error Term #9 for the Microstrip Patch with 12.5% Truncation in the Near-Field θ-Span**

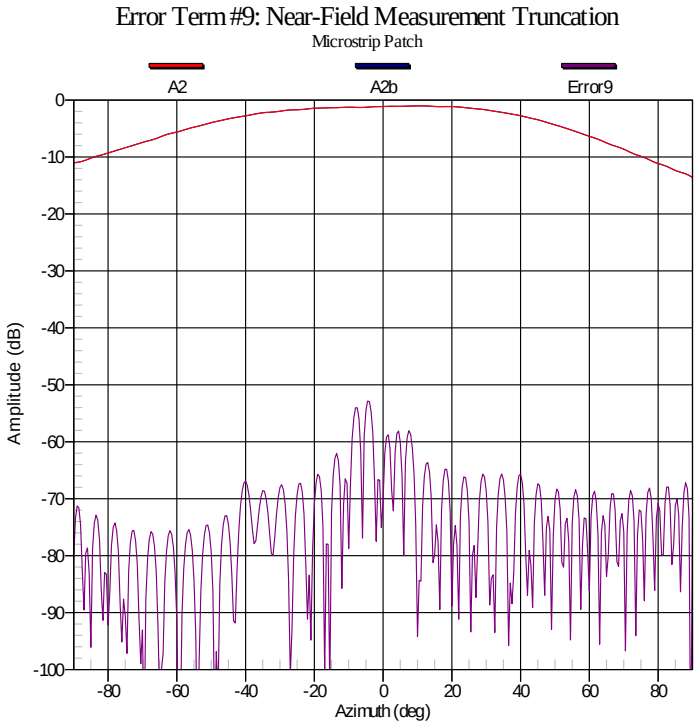


**Figure 4-17: Evaluation of Error Term #9 for the Microstrip Patch with 25% Truncation in the Near-Field θ-Span**

### 4.9.3 Slotted Waveguide Array

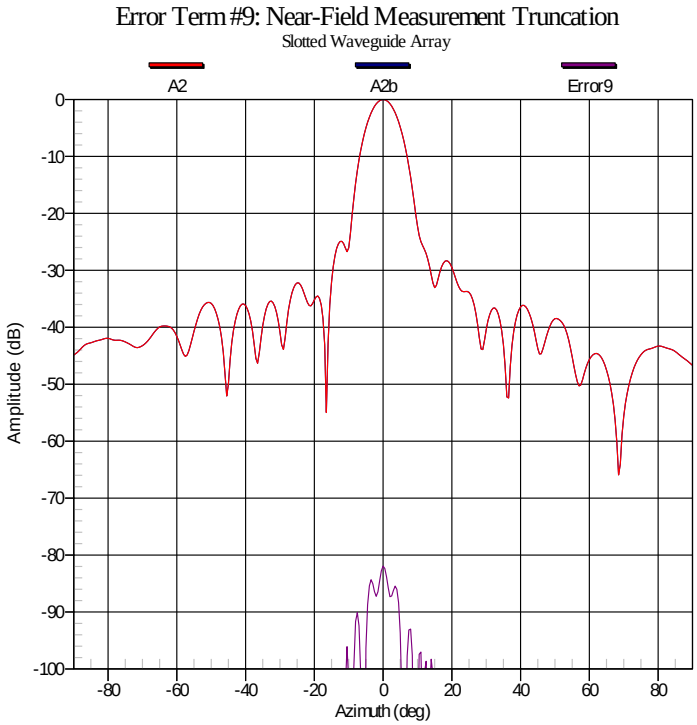


**Figure 4-18: Evaluation of Error Term #9 for the Slotted Waveguide Array with 12.5% Truncation in the Near-Field θ-Span**

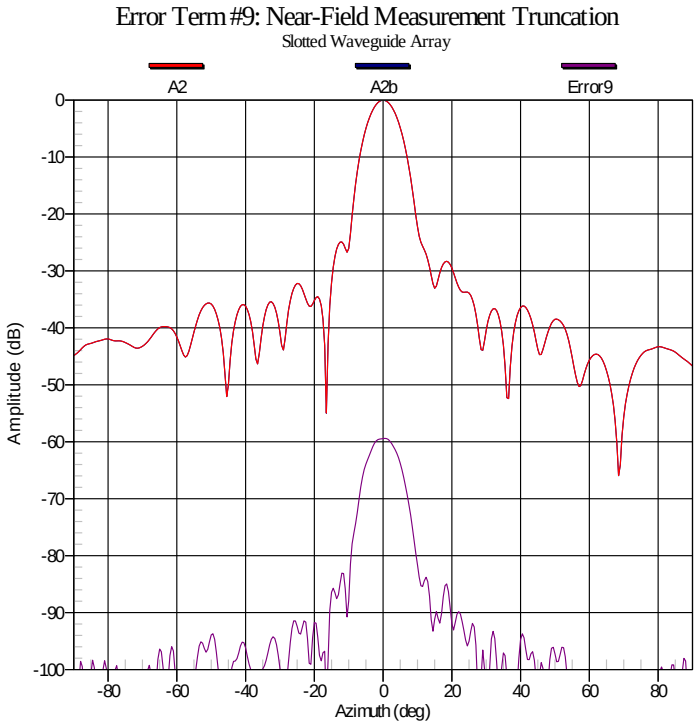


**Figure 4-19: Evaluation of Error Term #9 for the Slotted Waveguide Array with 25% Truncation in the Near-Field θ-Span**

### 4.9.4 Isoflux Horn

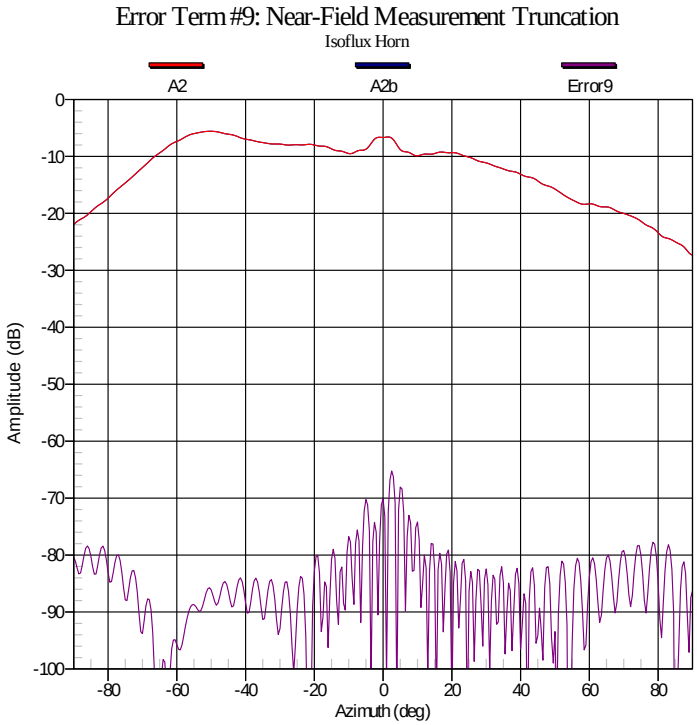


**Figure 4-20: Evaluation of Error Term #9 for the Isoflux Horn with 12.5% Truncation in the Near-Field θ-Span**

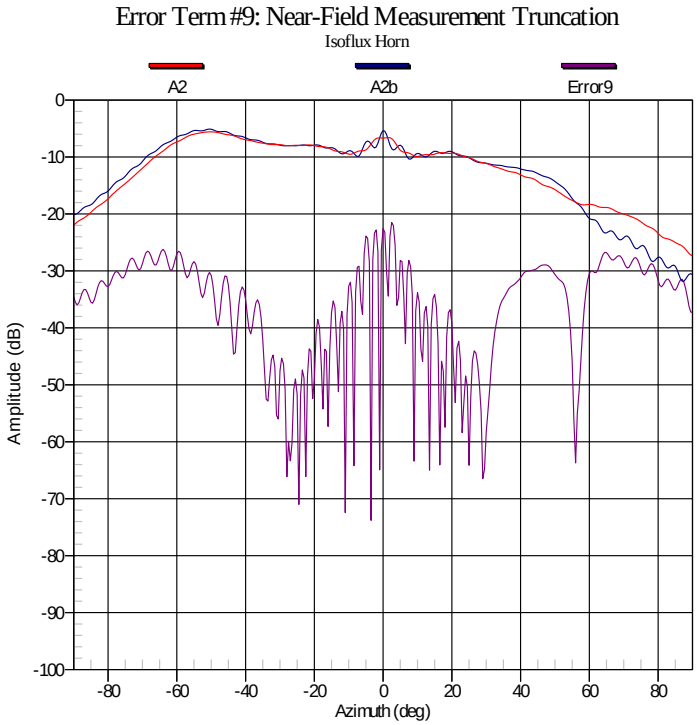


**Figure 4-21: Evaluation of Error Term #9 for the Isoflux Horn with 25% Truncation in the Near-Field θ-Span**

### 4.9.5 Discussion of Error Term #9

In Section 3.3.9 it was shown that this term will typically not appear in total uncertainty budgets since data is usually acquired over a closed scan surface (a complete sphere) in spherical near-field measurements. However, an analysis of the effects of truncating the near-field measurement region is included for completeness.

Figure 4-14 shows $Error_9(\theta,0)$ for the standard gain horn when the near-field $\theta$-span is truncated by 12.5%, where the truncation method outlined in Section 2.5.9 is applied to the near-field data. Likewise, Figure 4-15 shows the results when the measurement $\theta$-span is truncated by 25%. As expected, the resulting error signal increases as the amount of near-field data being truncated is increased.

The remaining figures show the results for the same analysis as described above for the microstrip patch, slotted waveguide array and isoflux horn, respectively. Figures 4-17 and 4-21 confirm that lower gain antennas are more heavily affected by near-field data

truncation than higher gain antenna types. This agrees well with the concept that planar near-field systems are ideal for higher gain antennas since the inherent truncation in this type of system will introduce errors in pattern results for lower gain antennas, such as the microstrip patch and isoflux horn tested here. Similar to the discussion for error term #9, it was found that by correcting for error term #11 prior to performing this analysis, one may isolate the analysis of this term to produce results for measurement truncation alone, as shown in Figure 4-22 below.

It should be restated that while the effects of truncation have a significant impact on far-field patterns, one may simply acquire data over a closed surface to remove these effects entirely, as is being done in the final uncertainty budgets presented in Section 4.19.

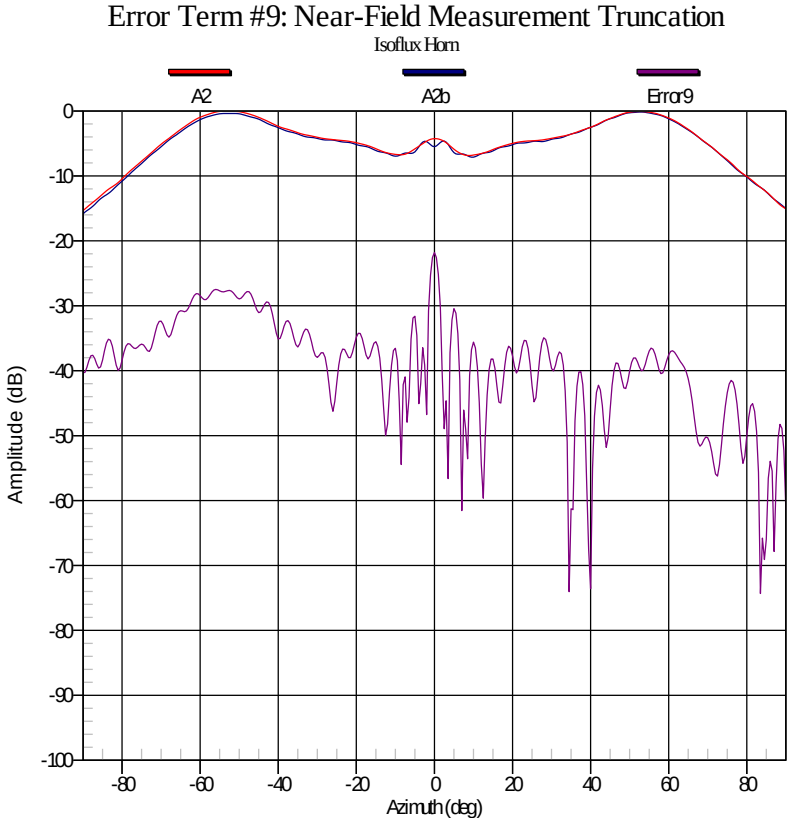


**Figure 4-22: Evaluation of Error Term #9 for the Isoflux Horn with 25% Truncation in the Near-Field θ-Span After Correcting for $\theta$ / $\phi$-Axis Non-Intersection Errors in $A_2$**

## 4.10 ERROR TERM #10: SPHERE RADIUS ERRORS

### 4.10.1 Standard Gain Horn

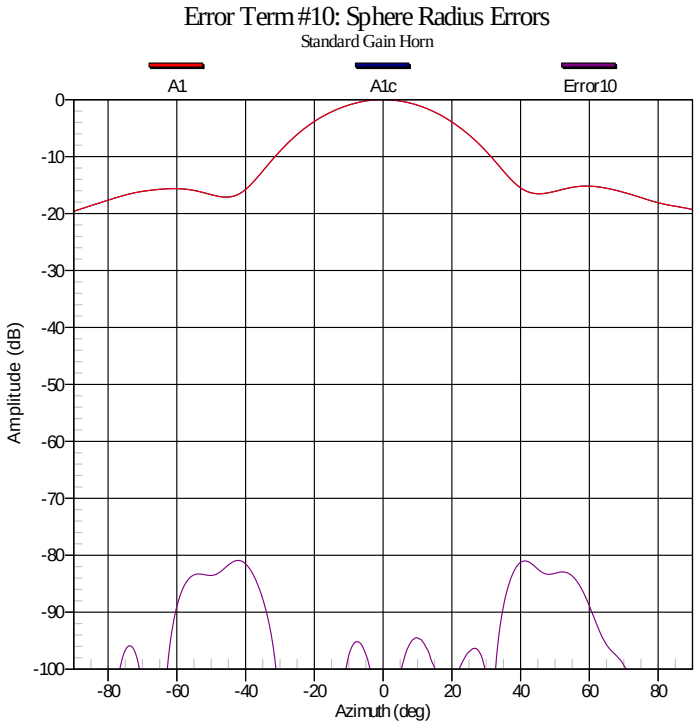


**Figure 4-23: Evaluation of Error Term #10 for the Standard Gain Horn with a 1 cm Simulated Change in the Near-Field Measurement Sphere Radius**

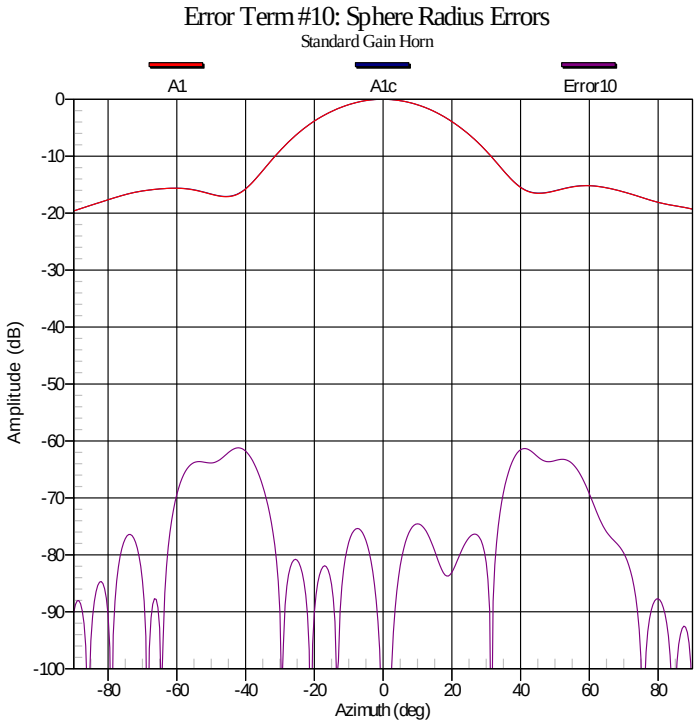


**Figure 4-24: Evaluation of Error Term #10 for the Standard Gain Horn with a 10 cm Simulated Change in the Near-Field Measurement Sphere Radius**

### 4.10.2 Microstrip Patch

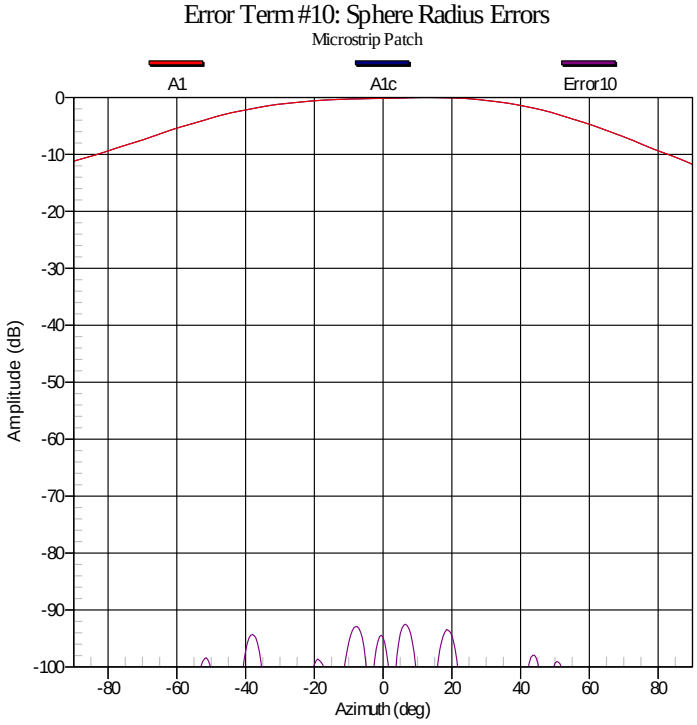


**Figure 4-25: Evaluation of Error Term #10 for the Microstrip Patch with a 1 cm Simulated Change in the Near-Field Measurement Sphere Radius**

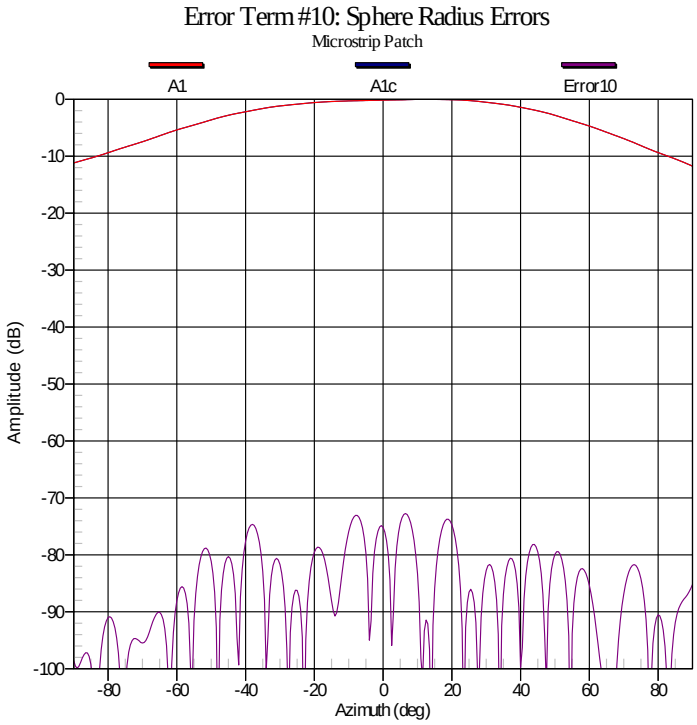


**Figure 4-26: Evaluation of Error Term #10 for the Microstrip Patch with a 10 cm Simulated Change in the Near-Field Measurement Sphere Radius**

### 4.10.3 Slotted Waveguide Array

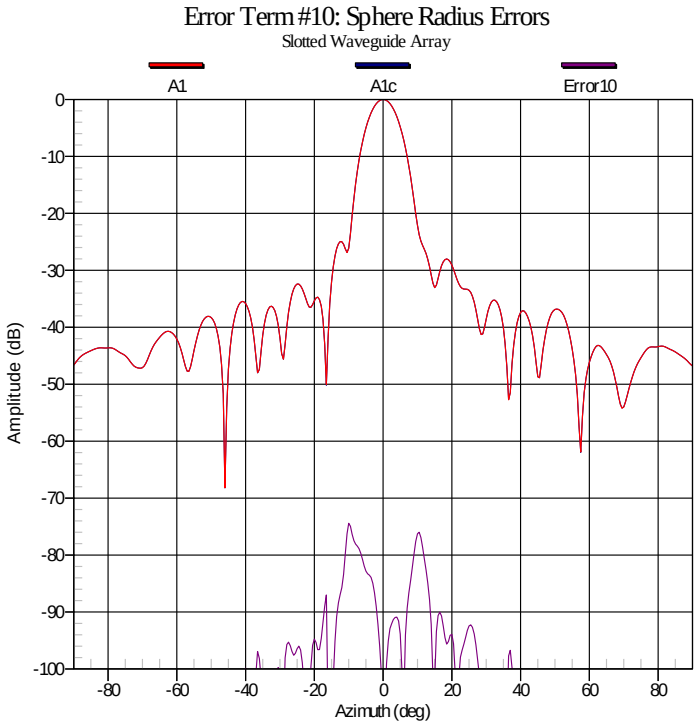


**Figure 4-27: Evaluation of Error Term #10 for the Slotted Waveguide Array with a 1 cm Simulated Change in the Near-Field Measurement Sphere Radius**

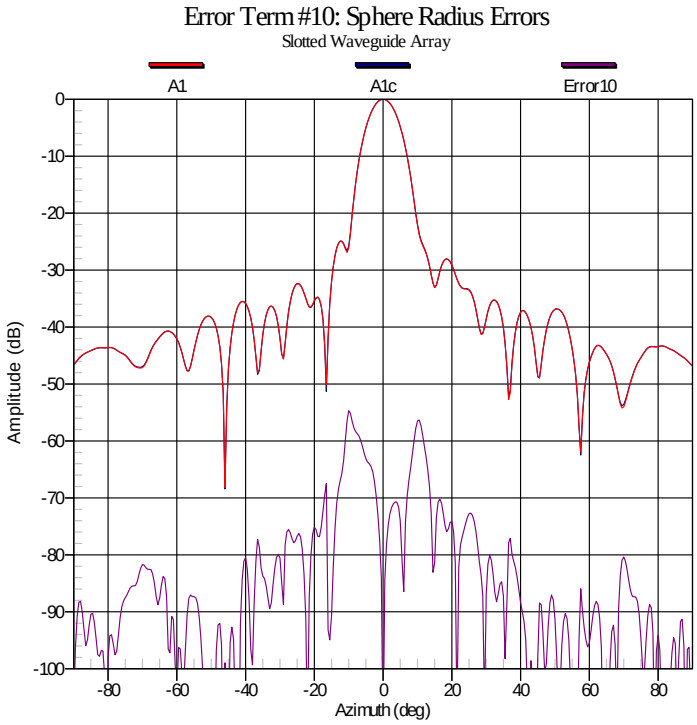


**Figure 4-28: Evaluation of Error Term #10 for the Slotted Waveguide Array with a 10 cm Simulated Change in the Near-Field Measurement Sphere Radius**

### 4.10.4 Isoflux Horn

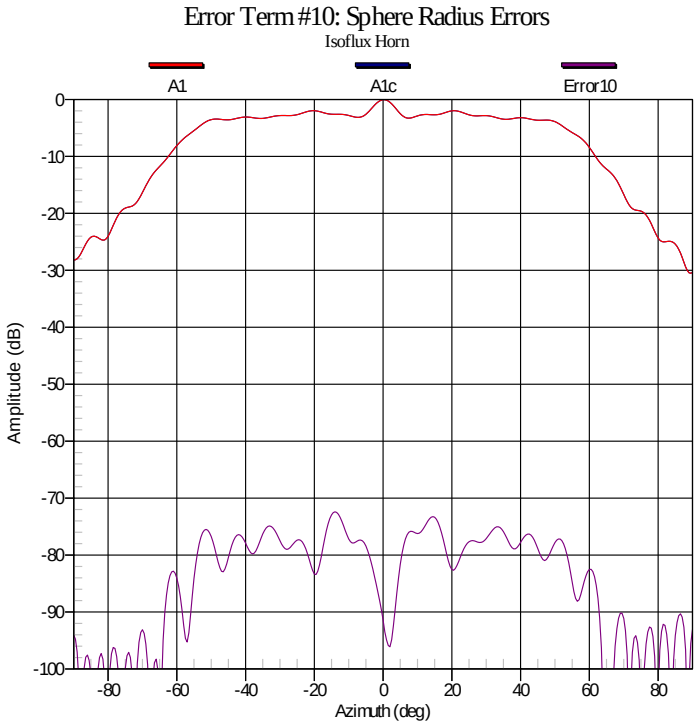


**Figure 4-29: Evaluation of Error Term #10 for the Isoflux Horn with a 1 cm Simulated Change in the Near-Field Measurement Sphere Radius**

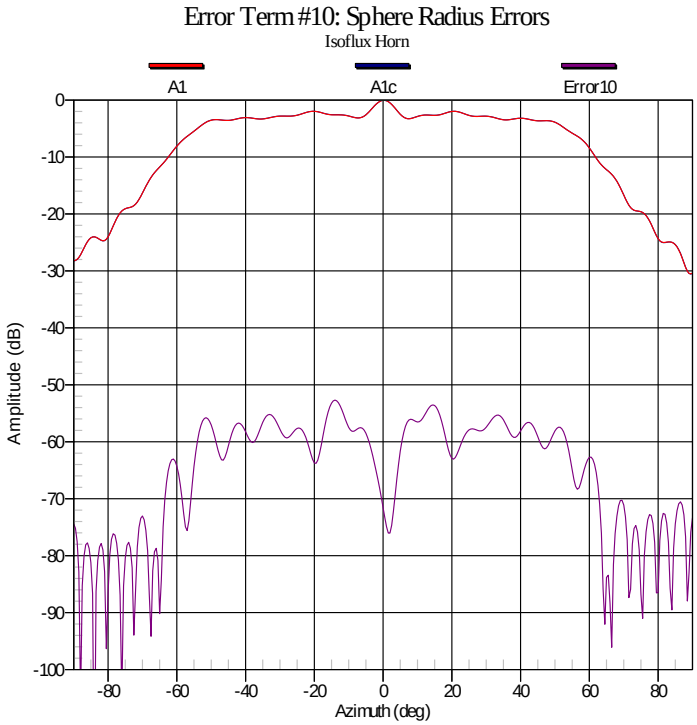


**Figure 4-30: Evaluation of Error Term #10 for the Microstrip Patch with a 10 cm Simulated Change in the Near-Field Measurement Sphere Radius**

### 4.10.5 Discussion of Error Term #10

In order to estimate the amplitude uncertainty due to uncertainty in the value of the measured SNF scan sphere radius, the method proposed in Section 2.5.10 was used. First, in Figure 4-23 the quoted AUT radiation pattern of the standard gain horn, $A_1$ is compared to $A_{1c}$, as explained in Section 3.3.10. The value of the SNF scan sphere radius was changed by 1 cm in the near-field to far-field transformation. The difference between these two patterns will produce an error signal $Error_{10}$. Figure 4-24 shows a similar analysis with a 10 cm change introduced to the value of the SNF scan sphere radius. For this antenna, an on-axis signal-to-noise ratio of roughly -90 dB is found for the worst-case example shown in Figure 4-24. A signal-to-noise ratio of -90 dB produces a negligible amplitude uncertainty. Since one can typically measure the SNF scan sphere radius with accuracy better than 10 cm, this error term should not be of great concern.

Figures 4-25 through 4-30 show the same results explained above for the microstrip patch, slotted waveguide array and isoflux horn. The resulting error signals for error term

#10 indicate that the effects of sphere radius uncertainty should not have a large impact on the overall uncertainty budget, even using the worst-case comparison. For the total uncertainty budgets presented in the final sections of this chapter, the worst-case examples shown above will be used.

## 4.11 ERROR TERM #11: SPHERE THETA/PHI ERRORS

### 4.11.1 Standard Gain Horn

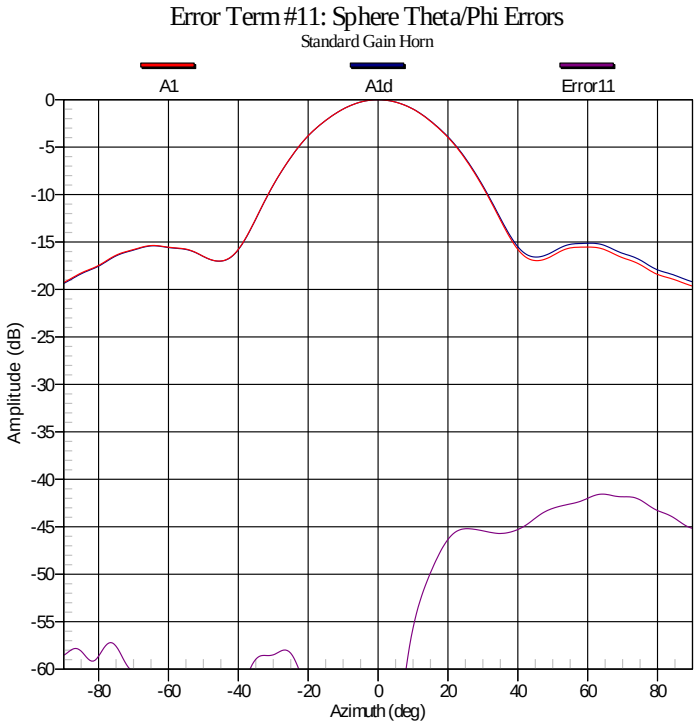


**Figure 4-31: Evaluation of Error Term #11 for the Standard Gain Horn**

### 4.11.2 Microstrip Patch

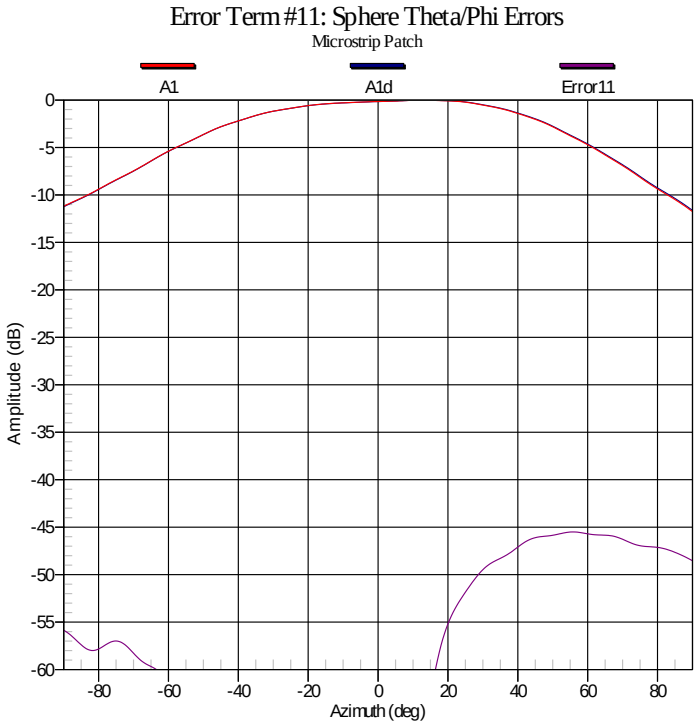


**Figure 4-32: Evaluation of Error Term #11 for the Microstrip Patch**

### 4.11.3 Slotted Waveguide Array

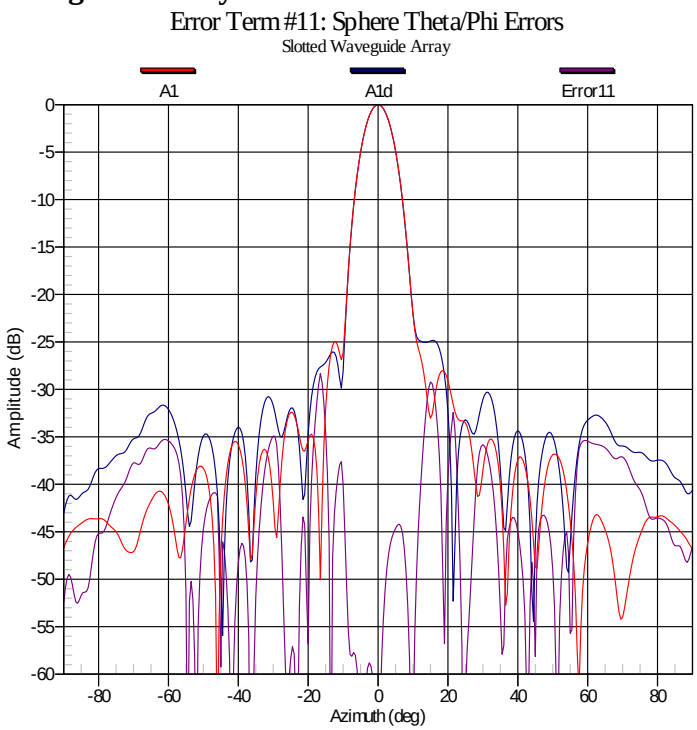


**Figure 4-33: Evaluation of Error Term #11 for the Slotted Waveguide Array**

### 4.11.4 Isoflux Horn

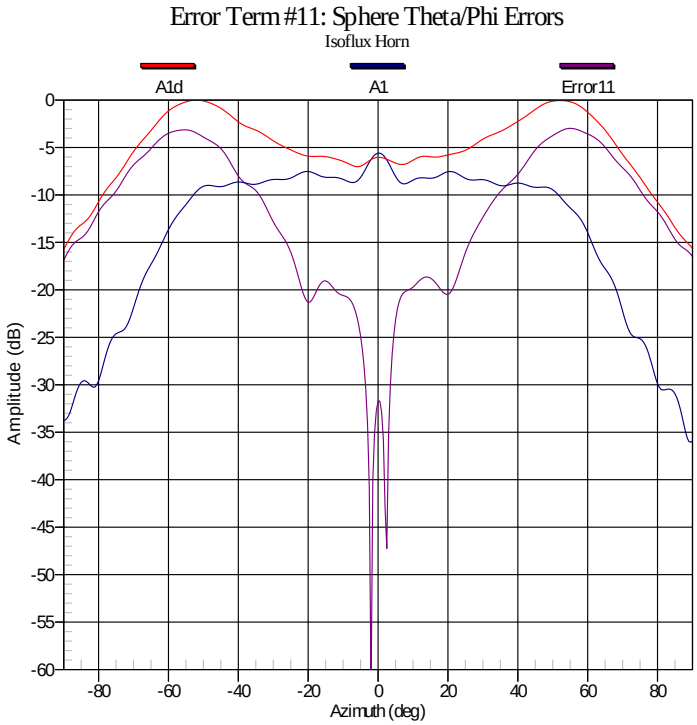


**Figure 4-34: Evaluation of Error Term #11 for the Isoflux Horn**

### 4.11.5 Discussion of Error Term #11

In Section 3.3.11, the reader was presented with the details required to estimate the effects of $\theta/\phi$-axis non-intersection by comparing the amplitude patterns $A_1$ and $A_{1d}$ to estimate the error signal due to this term.

Figure 4-31 shows the results obtained using this comparison for the standard gain horn. Since the on-axis error level is quite low, this source of error will have a negligible effect on the far-field gain uncertainty budgets. While the error level does rise to nearly -40 dB, this occurs in the region of the AUT's sidelobe, where amplitude uncertainty is expected to be higher than for the AUT's main beam. For this reason, this error level should not be a cause of major concern.

Next, in Figure 4-32 the same test has been done for the microstrip patch and appears to produce very similar results. Figure 4-33 shows the results obtained using this method on the slotted waveguide array. In that figure the error level peaks higher than it does for the

previous two antennas discussed. For a high gain antenna such as this, the method proposed in Section 2.5.11 may not be appropriate. Since this $\theta/\phi$-axis non-intersection correction method will make use of very low amplitude values when performing the correction discussed in Section 2.5.11 for this type of antenna, the results it produces may, in fact, not be a true correction for $\theta/\phi$-axis non-intersection errors. As discussed in Section 2.4, another (albeit crude) approach to estimate the effects of errors in the SNF scan sphere is to compare a redundant measurement taken at slow scan speed ($M_1$) to a 360-Phi measurement taken at regular scan speed, $M_3$. Figure 4-35 was included as it appears to provide a more reasonable error level associated with this term.

Lastly, error term #11 was estimated for the isoflux horn, as shown in Figure 4-34. At this point, the reader should not be shocked by the extremely high error signal level, since a major $\theta/\phi$-axis non-intersection error was already stated to be present in this antenna's radiation pattern in Section 3.5. Once again, the crude approach outlined in Section 2.4 was also used for comparison with the resulting error signal found in Figure 4-34. The error signal found using this approach, as shown in Figure 4-36, agrees very well with the error signal found in Figure 4-34. This provides confidence that the error signal evaluated using the crude approach for the slotted waveguide array provides reasonably accurate results. It is recommended that one uses the methods outlined in Section 2.5.11 to evaluate this error term for all antenna types. However, one should verify the validity of the results by comparing them to the results obtained using the approach discussed in Section 2.4.

It is also evident that while the error levels shown in Figures 4-33 and 4-34 appear mostly symmetric, this is not the case for the results presented in Figures 4-31 and 4-32. While the exact reason for the varying results is unknown, it is suspected that a change in system alignment was made after the microstrip patch was measured. However, without accurately determining the $\theta/\phi$-axis non-intersection of the SNF system using precision optical tools for each AUT setup, it is difficult to determine the exact cause of the deviation.

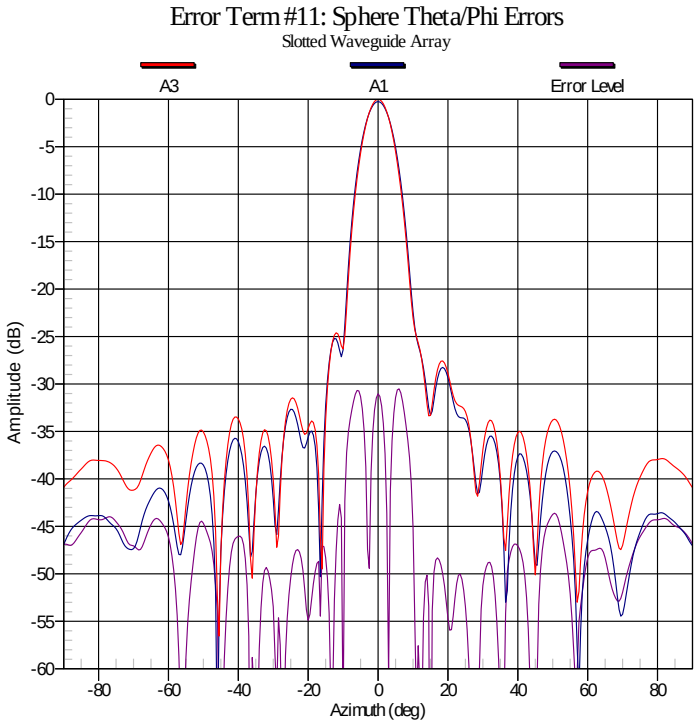


**Figure 4-35: Evaluation of Error Term #11 for the Slotted Waveguide Array Using the Crude Approach Discussed in Section 2.4**

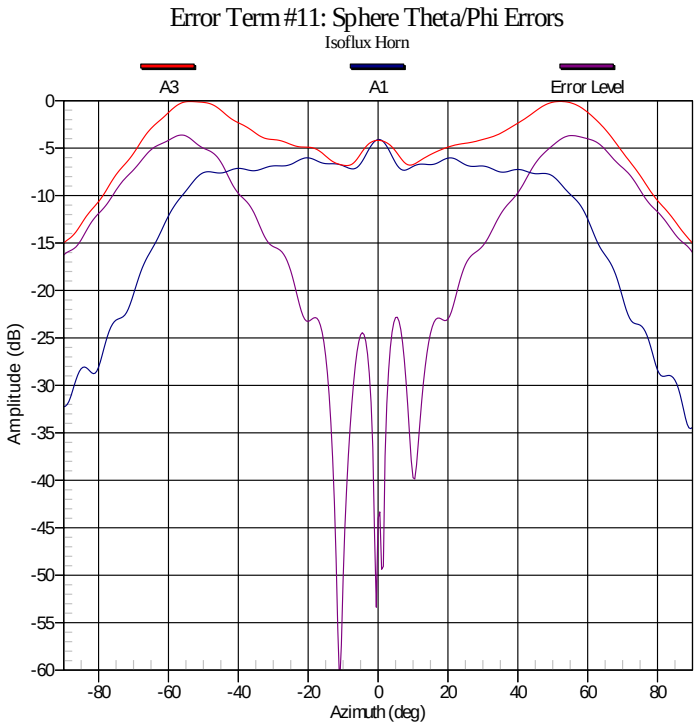


**Figure 4-36: Evaluation of Error Term #11 for the Isoflux Horn Using the Crude Approach Discussed in Section 2.4**

## 4.12 ERROR TERM #12: HIGHER ORDER COUPLING

### 4.12.1 Standard Gain Horn

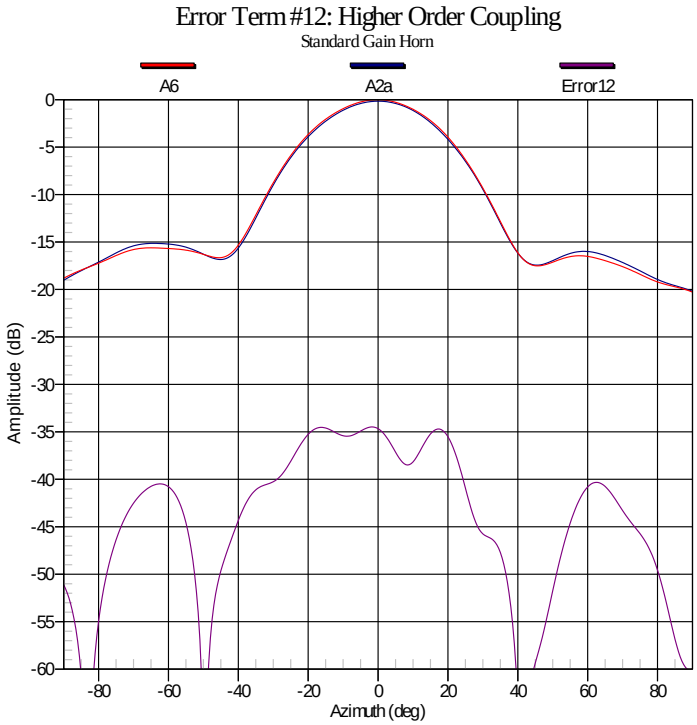


**Figure 4-37: Evaluation of Error Term #12 for the Standard Gain Horn**

### 4.12.2 Microstrip Patch

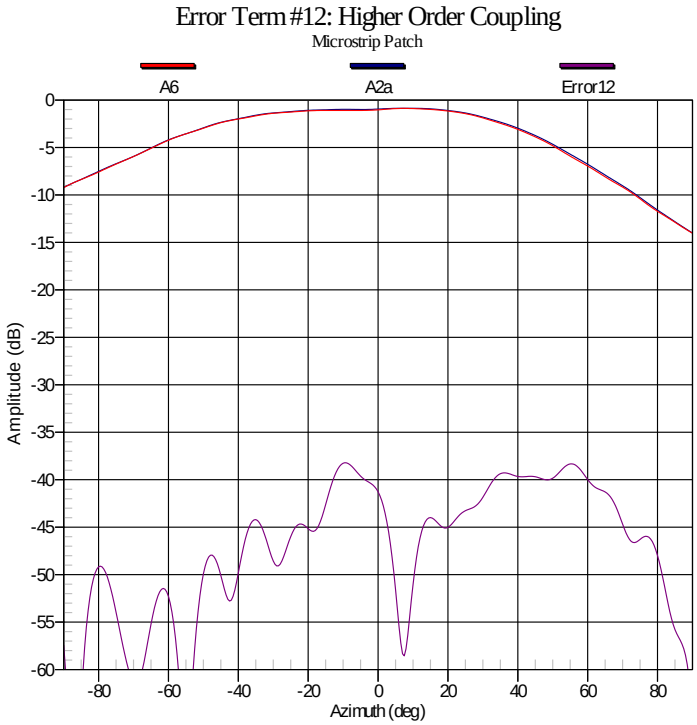


**Figure 4-38: Evaluation of Error Term #12 for the Microstrip Patch**

### 4.12.3 Slotted Waveguide Array

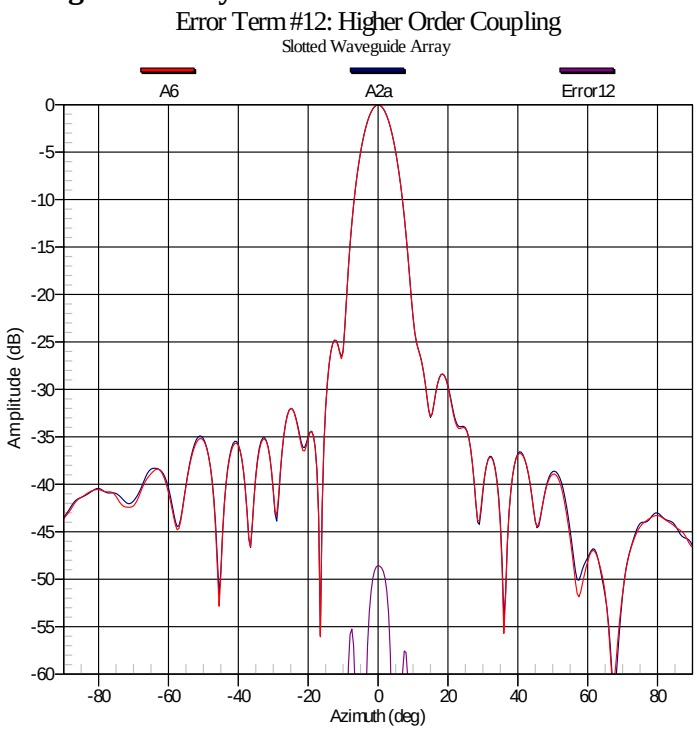


**Figure 4-39: Evaluation of Error Term #12 for the Slotted Waveguide Array**

### 4.12.4 Isoflux Horn

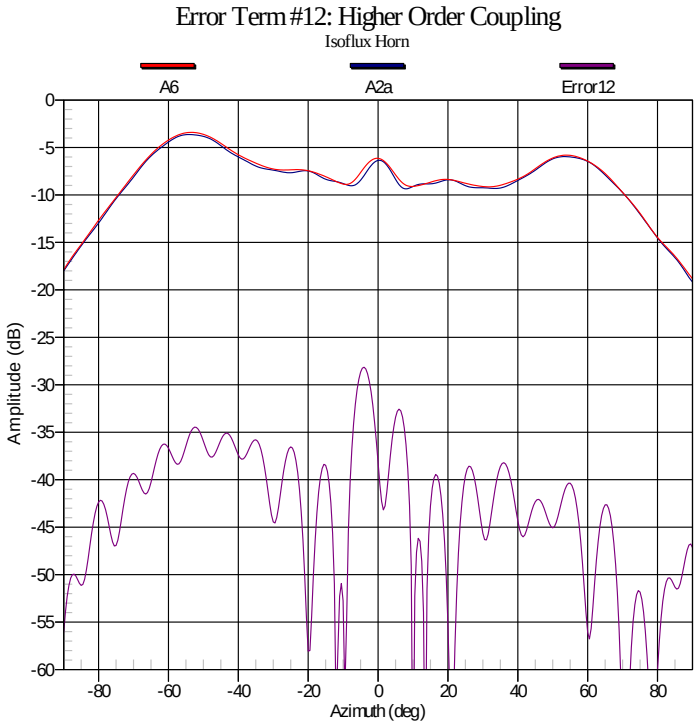


**Figure 4-40: Evaluation of Error Term #12 for the Isoflux Horn**

### 4.12.5 Discussion of Error Term #12

As outlined in Sections 2.5.12 and 3.3.12, the effects of higher order coupling between the probe and AUT can be estimated by comparing the far-field patterns computed using two sets of data acquired with a λ/4 difference in probe-to-AUT separations. The far-field pattern amplitudes used to estimate $Error_{12}$ here are $A_{2a}$ and $A_6$, as Table 3-2 outlines.

First, Figure 4-37 shows the estimation of error term #12 for the standard gain horn. With an on-axis error-to-signal ratio of roughly -34 dB, this error term will have a noticeable impact on pattern peak and gain budgets for this antenna. One also sees significant amplitude variation between $A_{2a}$ and $A_6$ around the antenna pattern's sidelobe region, which will increase the total uncertainty of the measured amplitude for this antenna's sidelobe.

Next, Figure 4-38 shows the same comparison that was outlined above for the microstrip patch antenna. Since this antenna radiates (or receives) energy over a wide angular sector,

the effects of higher order coupling between the probe and AUT have a similar effect across this wide sector. Thus, the error-to-signal ratio remains fairly constant for all $\theta$ values shown in this figure. In contrast, we found that the error-to-signal ratio increased in the standard gain horn's sidelobe region.

For the case of the slotted waveguide array, the error signal for this term remains fairly low in the region of the radiation pattern's main beam, as shown in Figure 4-39. Since this antenna has a high directivity, the pattern amplitude drops off quickly away from the main beam. As the pattern amplitude approaches the noise floor, the concept of amplitude uncertainty loses significance since many factors can easily change the amplitude in this region by a large amount. As such, the error-to-signal ratio isn't of great concern in this region and details of $Error/S_{12}$ away from the main beam are not presented here.

Finally, the results for this error term are shown for the isoflux antenna in Figure 4-40. Since the error signal associated with higher order coupling is significant for this antenna, one can speculate that this chamber has poor performance at roughly 14 GHz[2]. Another possible cause for the fairly high error signal in this figure is that since the operating frequency is over 14 GHz, this antenna will be very susceptible to alignment errors introduced during the AUT translation performed before measurement $M_6$. With such a high frequency, small misalignments may be electrically large and could have a noticeable impact on the error signal associated with this term.

[2] Although the SNF chamber used for all measurement results presented in this thesis is equipped to perform measurements up to 20 GHz it has normally not been used at the higher frequency end, and so its performance quality there is unknown.

## 4.13 ERROR TERM #13: RECEIVER AMPLITUDE NON-LINEARITY

### 4.13.1 Standard Gain Horn

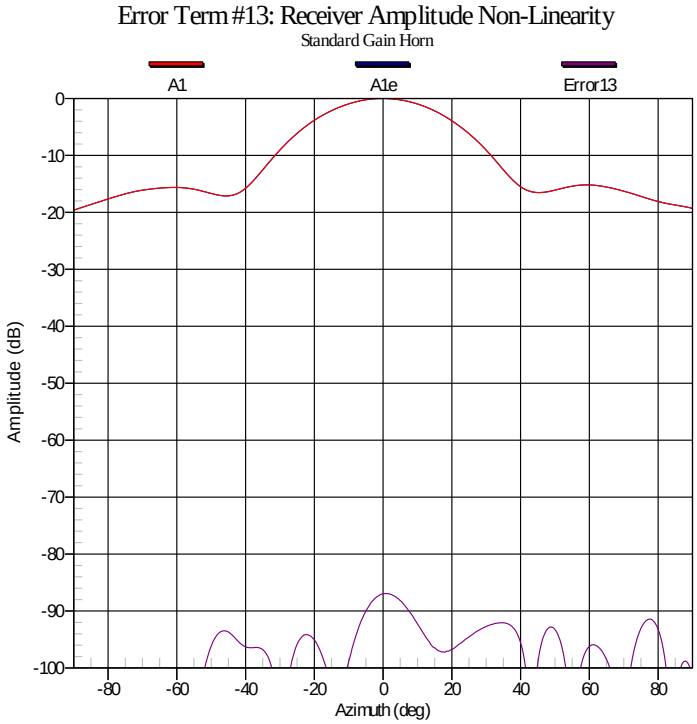


**Figure 4-41: Evaluation of Error Term #13 for the Standard Gain Horn**

### 4.13.2 Microstrip Patch

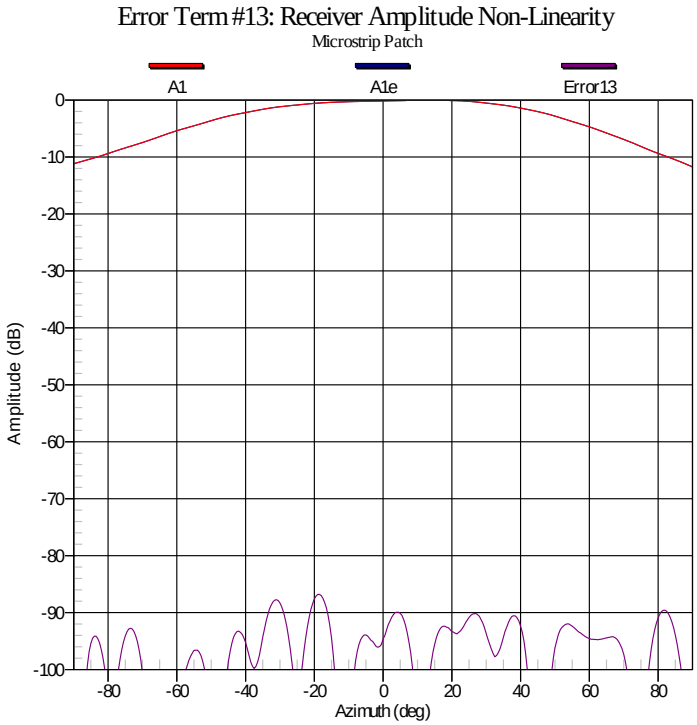


**Figure 4-42: Evaluation of Error Term #13 for the Microstrip Patch**

### 4.13.3 Slotted Waveguide Array

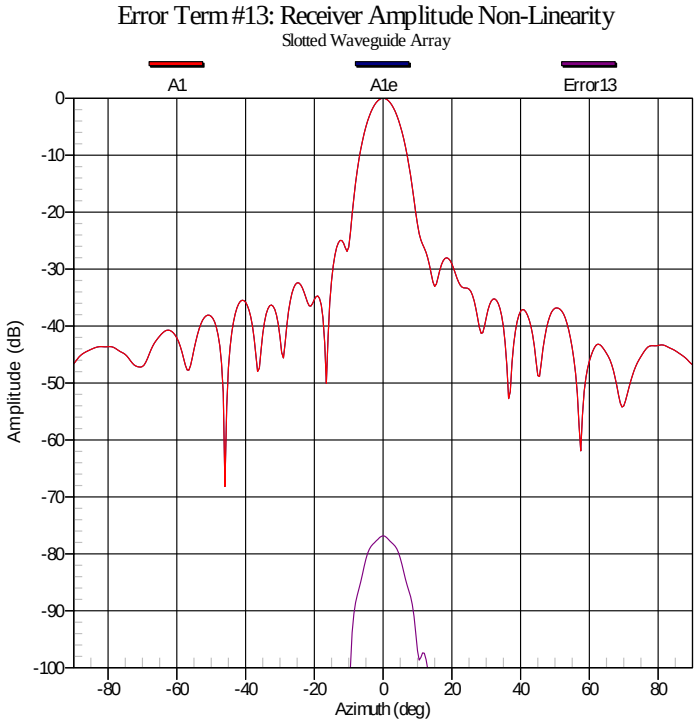


**Figure 4-43: Evaluation of Error Term #13 for the Slotted Waveguide Array**

### 4.13.4 Isoflux Horn

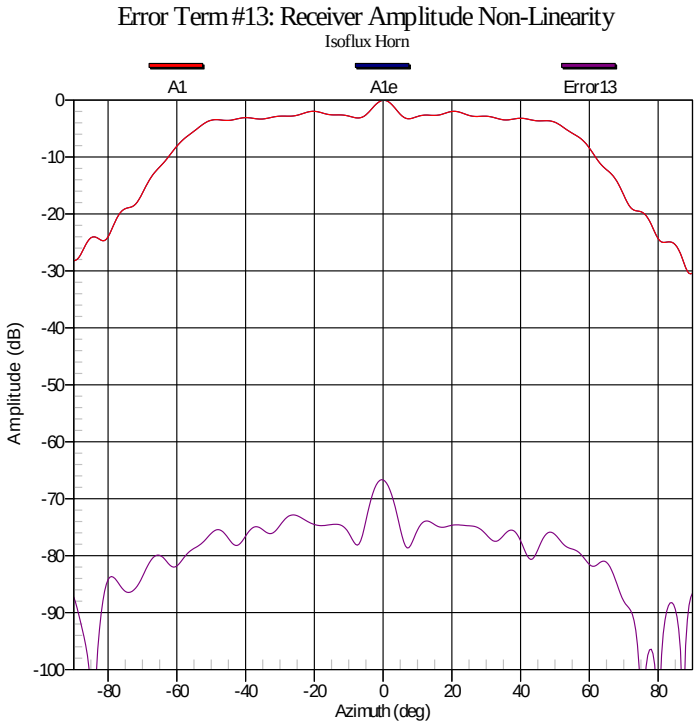


**Figure 4-44: Evaluation of Error Term #13 for the Isoflux Horn**

### 4.13.5 Discussion of Error Term #13

The results of Figures 4-41 through 4-44 were acquired using the error signal evaluation method outlined in Section 2.5.13. By comparing the quoted AUT radiation pattern, $A_1$, with a version of this pattern that has had linearity corrections performed on its near-field data ($A_{1c}$) one may estimate the error level associated with this term. The non-linearity profile used had been previously measured for the specific receiver used to make the near-field measurements and the corrections outlined below were applied to the measured near-field amplitudes.

- -10 dBm to -15 dBm, +0.16 dB to measured amplitude
- -15 dBm to -20 dBm, +0.06 dB to measured amplitude
- -20 dBm to -40 dBm, +0.01 dB to measured amplitude
- -40 dBm to -60 dBm, +0.06 dB to measured amplitude
- -60 dBm to -80 dBm, +0.09 dB to measured amplitude
- -80 dBm to -100 dBm, +0.12 dB to measured amplitude

- -100 dBm to -120 dBm, +0.20 dB to measured amplitude
- <-120 dBm, -0.26 dB to measured amplitude

In Figures 4-41 and 4-42 it is difficult to spot any trend in the shape of the error signal estimated using the method outlined above since the error signal is very low. These errors are very low with respect to the AUT's pattern amplitude so the effects of receiver amplitude non-linearity are negligible for these antennas.

While the resulting error signal is higher for the slotted waveguide array and isoflux antenna than for the other two AUTs, the amplitude of $Error_{13}$ is still sufficiently below the quoted pattern amplitude. As such, this error term will not have a large contribution to the overall uncertainty budget. Since the error signal associated with receiver amplitude non-linearity has the same general shape as the AUT pattern amplitude for these two cases, one has confidence that the results presented are, in fact, due to receiver amplitude non-linearity. As discussed in Section 2.5.13, amplitude non-linearity becomes more evident for higher power levels, as Figures 4-43 and 4-44 show.

## 4.14 ERROR TERM #14: SYSTEM PHASE ERRORS

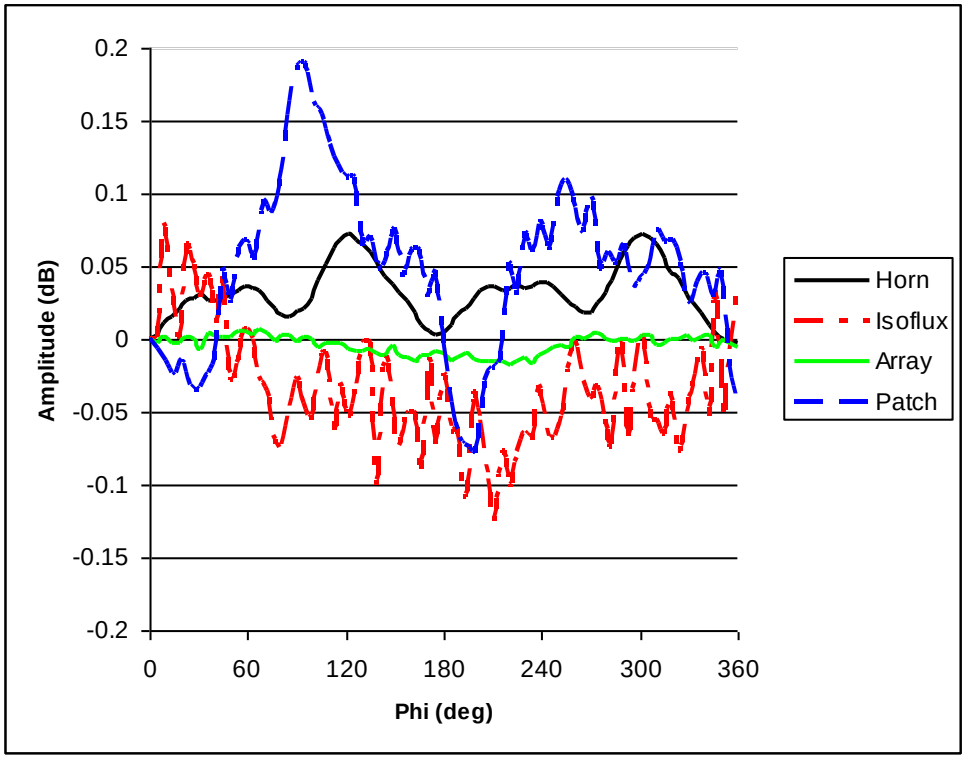


**Figure 4-45: Near-Field Amplitude Variation during Measurement $M_5$ (Self-Normalized to $A_5(0)$)**

As discussed in Section 3.3.14, the amplitude uncertainty due to system phase errors is set to the near-field peak-to-peak amplitude of measurement $M_5$. By rotating the AUT's phi axis and the probe simultaneously, one expects constant amplitude throughout the measurement. However, imperfections in the rotary joints of these two axes of motion will introduce some variation to the measured amplitude. Figure 4-45 shows the results for measurement $M_5$ for the four antennas being discussed here. The measured amplitudes have all been self-normalized to the value at $\phi = 0^{\circ}$, namely $A_5(0)$. The resulting peak-to-peak amplitudes have been summarized in Table 4-3 below.

Table 4-3 appears to indicate that the method used to evaluate this error term produces results that are highly dependent on the AUT's directivity. If this is the case, one can speculate that errors caused by misalignment or on-axis room scattering are contributing to this term, since such errors are highly dependent on the antenna's directivity.

While not required for the analysis of this error term, the phase variation throughout measurement $M_5$ was also included in Figure 4-46 for the benefit of the reader. This plot also leads one to speculate that the results for this error term are dependent on the AUT's directivity, since the phase variation increases as the AUT's directivity drops.

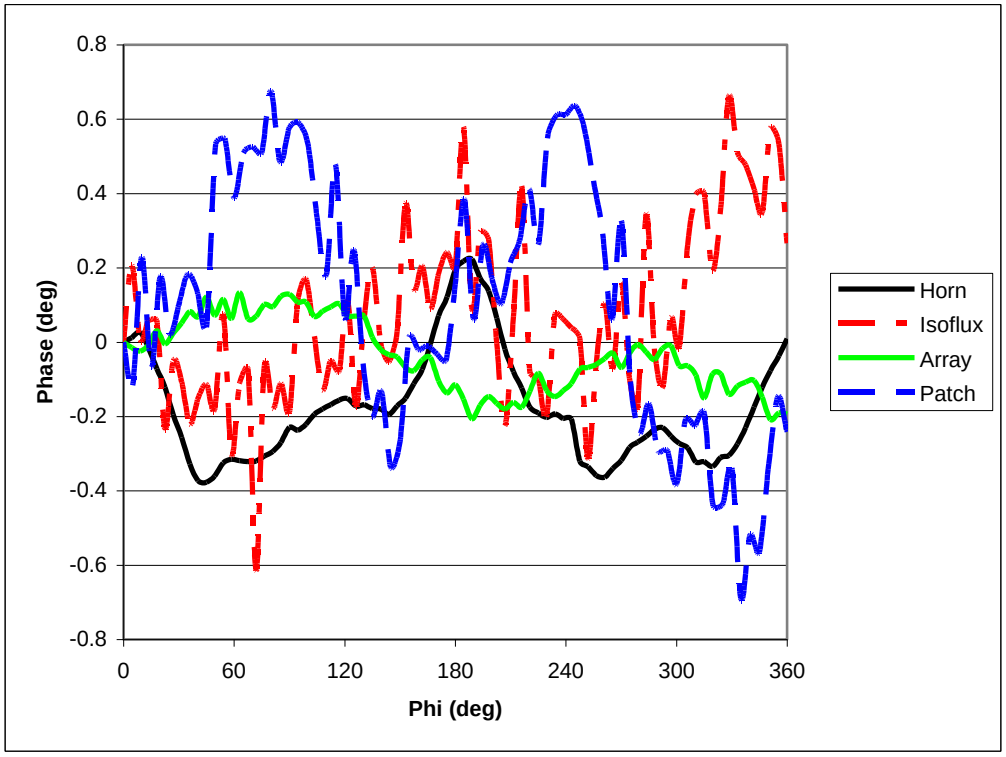


**Figure 4-46: Near-Field Amplitude Variation during Measurement $M_5$ (Self-Normalized to the Measured Phase at $\phi = 0^{\circ}$)**

**Table 4-3: Summary of Results for Measurement $M_5$**

| AUT | Peak-to-Peak Field Variation During $M_5$ (dB) | Near-Field Phase Variation During $M_5$ |
|---|---|---|
| Standard Gain Horn | 0.075 | 0.600 ˚ |
| Microstrip Patch | 0.267 | 1.368 ˚ |
| Slotted Waveguide Array | 0.025 | 0.341 ˚ |
| Isoflux Horn | 0.204 | 1.279 ˚ |

## 4.15 ERROR TERM #15: RECEIVER DYNAMIC RANGE

In Sections 2.5.15 and 3.3.15 it was stated that the measured on-axis SNR can be used to estimate the noise floor level relative to the far-field pattern's peak. Since the validity of all data acquired at the noise floor is questionable, one can consider this value of the error signal as being due to the receiver's limited dynamic range. Table 4-4 below summarizes the measured on-axis SNR values for the four antennas tested to verify this process. In order to to estimate the on-axis SNR, the amplitude and phase are recorded 10, 000 times and averaged. As the number of averages is increased, the confidence of the recorded signal level increases and the SNR is increased.

For the standard gain horn and slotted waveguide array antennas, the on-axis SNR was high enough that the receiver's limited dynamic range will not introduce a noticeable error on far-field patterns. For the microstrip patch, the on-axis SNR of roughly 55 dB means that the receiver's limited dynamic range may have a very minor effect on the far-field pattern. Similarly, the SNR of 45 dB for the isoflux antenna will introduce a noticeable pattern amplitude uncertainty into the quoted AUT radiation pattern for this antenna. With a limited dynamic range such as this, one can expect other error terms to be dominated by the high amplitude noise floor, as will be seen in Sections 4.17 and 4.18.

**Table 4-4: Recorded On-Axis SNR for Error Term #15**

| AUT | On-Axis SNR (dB) |
|---|---|
| Standard Gain Horn | 71.495 |
| Isoflux Horn | 45.047 |
| Slotted Waveguide Array | 65.071 |
| Microstrip Patch | 54.813 |

## 4.16 ERROR TERM #16: ROOM SCATTERING

In Section 2.5.16, reasons were discussed as to why this particular evaluation method will grossly over-estimate the errors associated with room scattering. Therefore, only the results obtained using Possibility #2 and #3 from Section 3.3.16 will be presented here.

### 4.16.1 Standard Gain Horn

#### *A. Possibility #2*

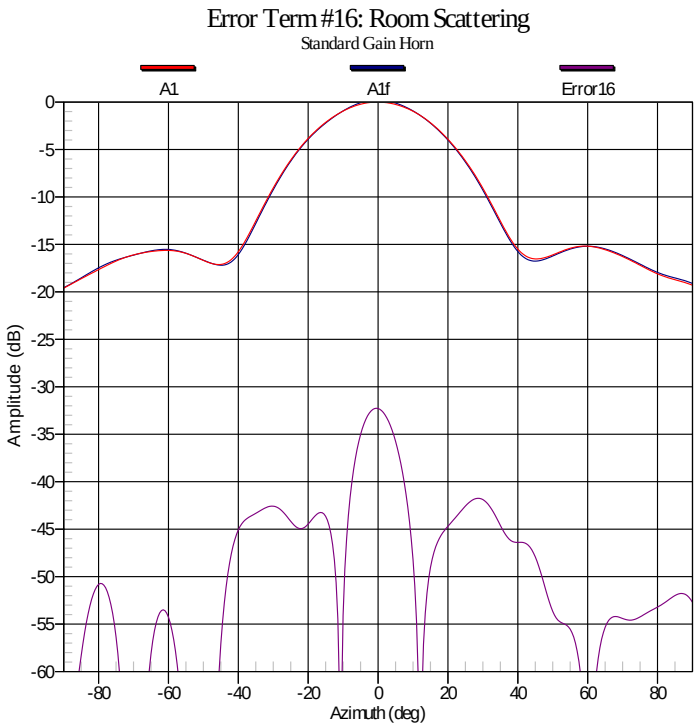


**Figure 4-47: Evaluation of Error Term #16 for the Standard Gain Horn using *Possibility #2* from Section 3.3.16**

### *B. Possibility #3*

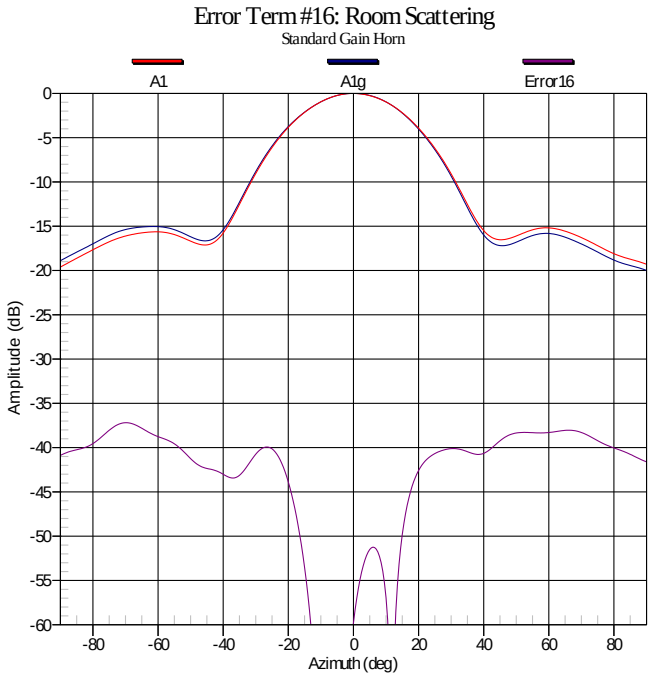


**Figure 4-48: Evaluation of Error Term #16 for the Standard Gain Horn using *Possibility #3* from Section 3.3.16**

## 4.16.2 Microstrip Patch

### *A. Possibility #2*

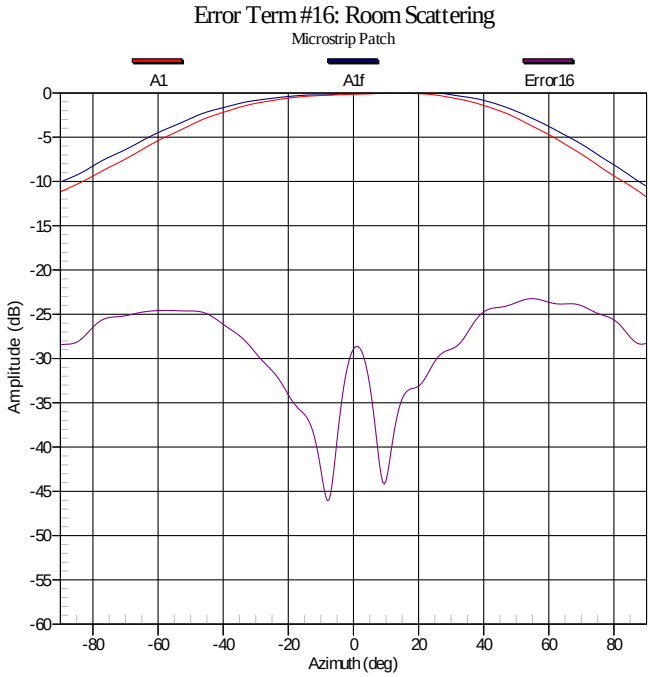


**Figure 4-49: Evaluation of Error Term #16 for the Microstrip Patch using *Possibility #2* from Section 3.3.16**

### *B. Possibility #3*

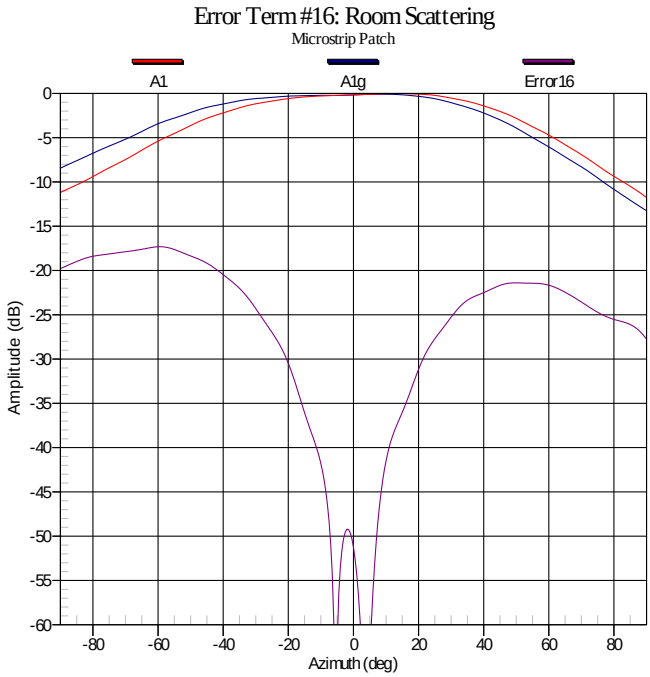


**Figure 4-50: Evaluation of Error Term #16 for the Microstrip Patch using *Possibility #3* from Section 3.3.16**

## 4.16.3 Slotted Waveguide Array

### *A. Possibility #2*

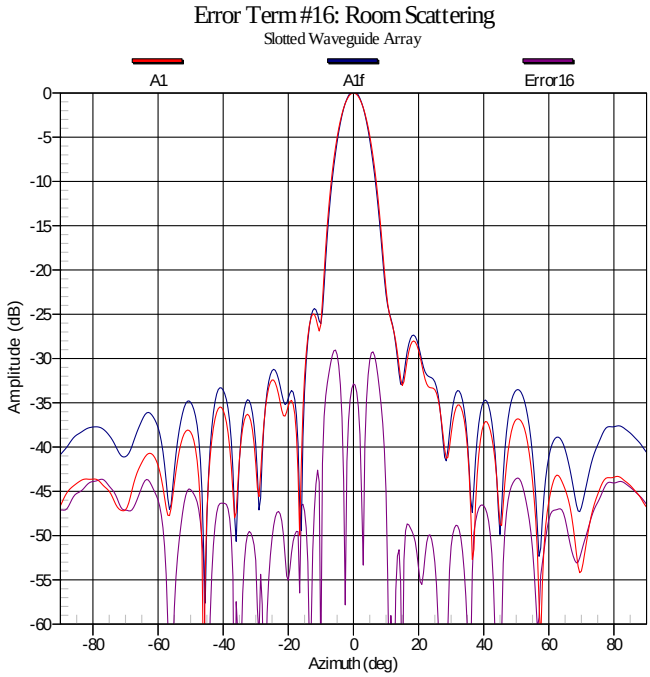


**Figure 4-51: Evaluation of Error Term #16 for the Slotted Waveguide Array using *Possibility #2* from Section 3.3.16**

### *B. Possibility #3*

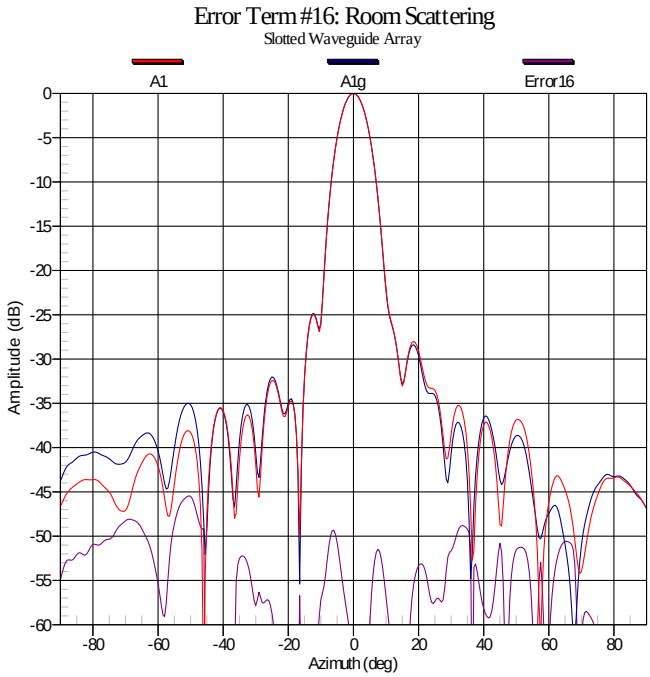


**Figure 4-52: Evaluation of Error Term #16 for the Slotted Waveguide Array using *Possibility #3* from Section 3.3.16**

## 4.16.4 Isoflux Horn

### *A. Possibility #2*

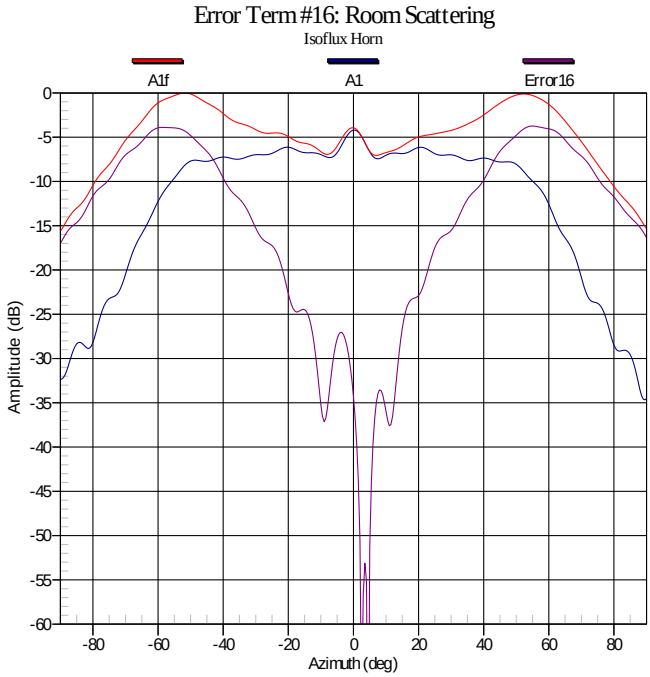


**Figure 4-53: Evaluation of Error Term #16 for the Isoflux Horn using *Possibility #2* from Section 3.3.16**

***B. Possibility #3***

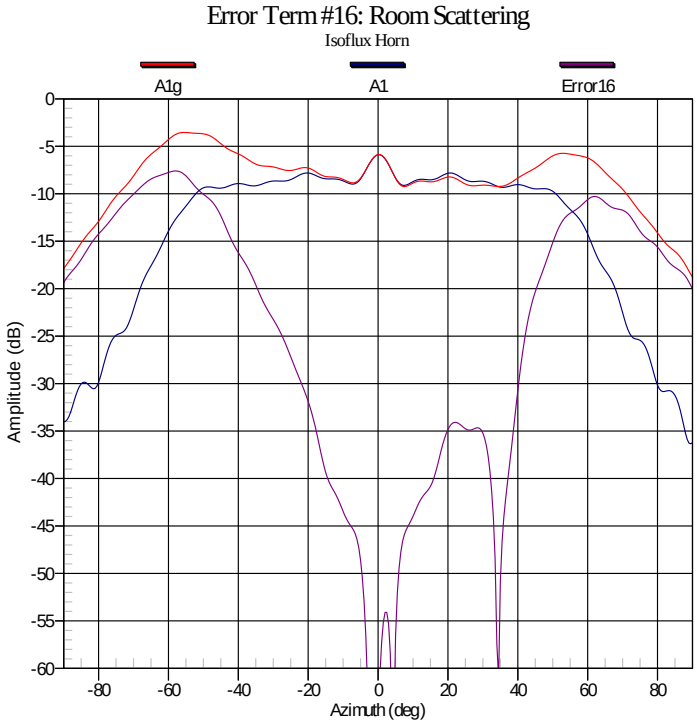


**Figure 4-54: Evaluation of Error Term #16 for the Isoflux Horn using *Possibility #3* from Section 3.3.16**

### 4.16.5 Discussion of Error Term #16

In this section, the results for error term #16 were presented using two different evaluation methods. Recall from Section 2.3.1 that the chosen sampling strategy (180-Phi, 360-Phi, theta/phi redundant) will influence the amount of room scattering in an SNF measurement. Figures 4-47 through 4-54 appear to show that *Possibility #3*, as outlined in Section 3.3.16, produce lower on-axis room scattering results. Since this comparison makes use of the quoted AUT radiation pattern, $A_1$, the effects of room scattering are already somewhat averaged out, as explained in Section 3.2.1. As such, one can expect that the use of either *Possibility #2* or *Possibility #3* will over-estimate the effects of room scattering. However, since on-axis uncertainty (including gain uncertainty) budgets are typically of greater interest than sidelobe budgets, the use of *Possibility #3* would be considered ideal since the over-estimation of on-axis room scattering is less severe than for the other option. On the other hand, if one were interested in sidelobe budgets, the other option may produce more realistic room scattering results.

Figures 4-49 and 4-50 show that the microstrip patch was very sensitive to room scattering. This was verified in the chamber through a course of several measurements, where absorber was continually added and removed to determine the sensitivity to scattering.

Figures 4-53 and 4-54 show, as expected, that the comparison of measurements acquired using different sampling strategies yield erroneous results for the isoflux antenna, since the effects of $\theta/\phi$-axis non-intersection errors dominate this term. Using pre-compensated plots for this comparison, similar to what was done in Sections 4.8 and 4.9 can help to provide more reasonable estimates of room scattering.

## 4.17 ERROR TERM #17: CABLE LEAKAGE

### 4.17.1 Standard Gain Horn

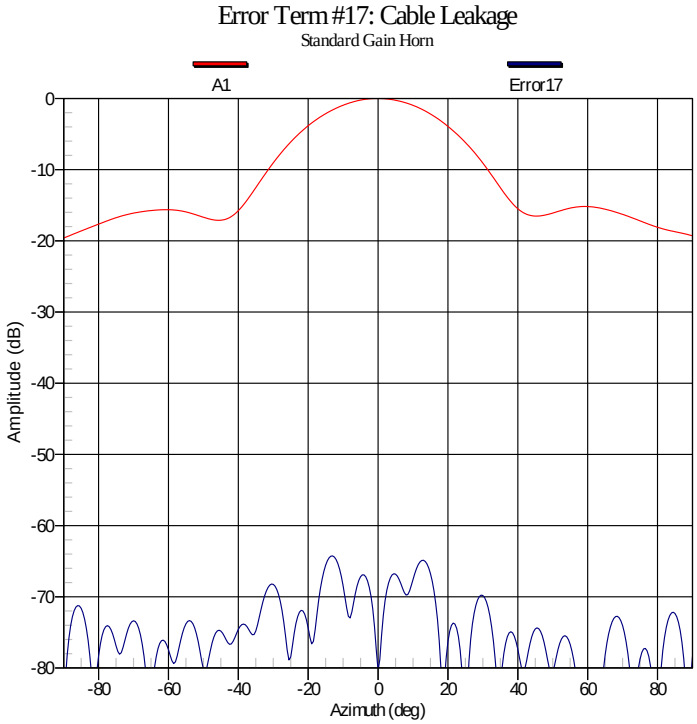


**Figure 4-55: Evaluation of Error Term #17 for the Standard Gain Horn**

### 4.17.2 Microstrip Patch

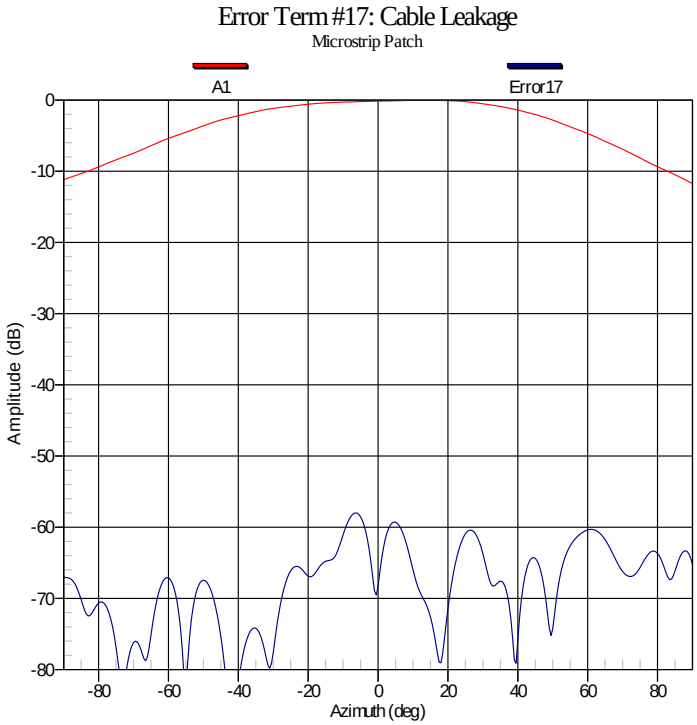


**Figure 4-56: Evaluation of Error Term #17 for Microstrip Patch**

### 4.17.3 Slotted Waveguide Array

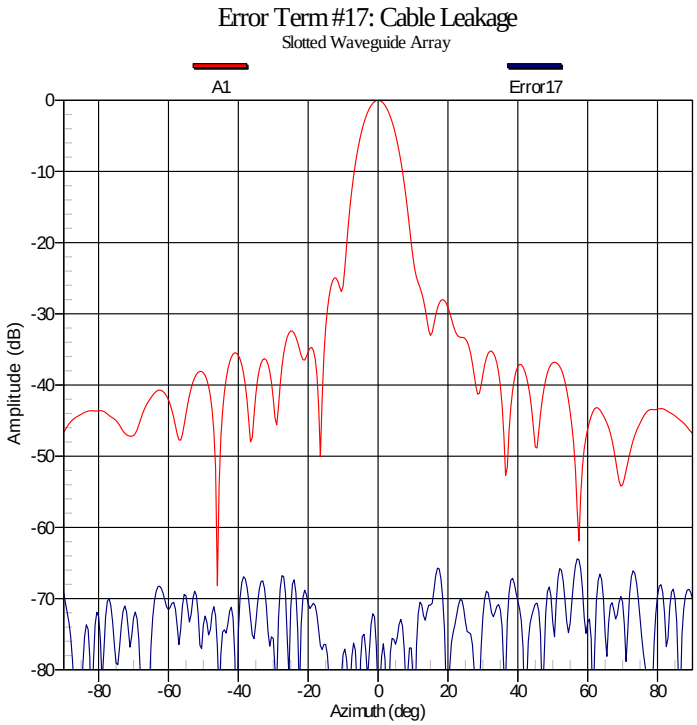


**Figure 4-57: Evaluation of Error Term #17 for the Slotted Waveguide Array**

### 4.17.4 Isoflux Horn

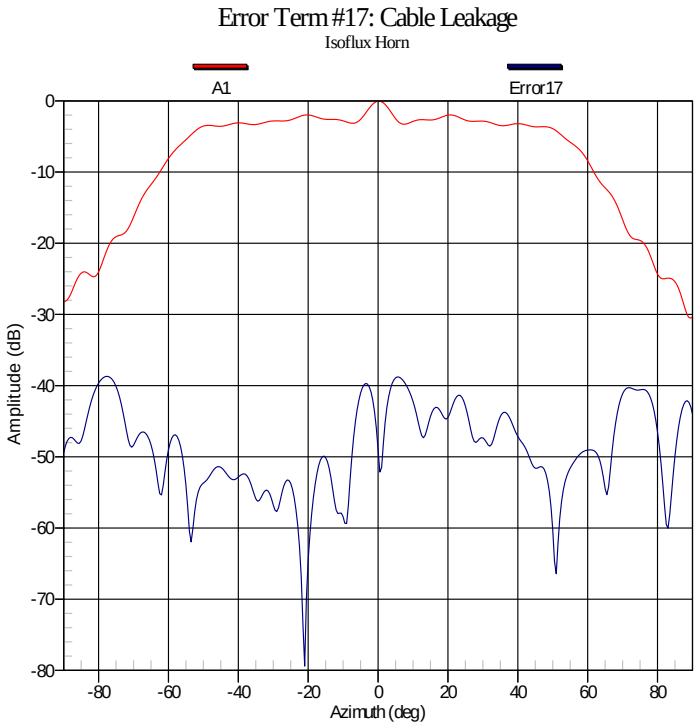


**Figure 4-58: Evaluation of Error Term #17 for the Isoflux Horn**

### 4.17.5 Discussion of Error Term #17

To estimate the impact that cable radiation has on the quoted AUT radiation pattern, the cable leakage analysis presented in Section 2.5.17 was used for all four antennas. First, Figure 4-55 shows the quoted AUT pattern amplitude, $A_1$, for the standard gain horn along with the error level due to cable leakage for this antenna (at this test frequency). With a leakage signal roughly 75 dB below the AUT pattern peak, the effects of cable leakage will not have a noticeable impact on the quoted AUT radiation pattern.

Next, Figures 4-56 and 4-57 show the results of the same analysis for the microstrip patch and slotted waveguide array, respectively. As these figures show, the resulting error signal levels due to cable leakage are once again sufficiently low that they will not greatly impact the shape of the far-field pattern.

Finally, Figure 4-58 shows the error signal level due to cable leakage for the isoflux antenna. While one may immediately assume that there is significant cable leakage

present in the quoted AUT radiation pattern for this antenna, this high error level may be due to the isoflux antenna's limited signal-to-noise ratio. With an SNR of roughly 45 dB, one cannot expect to measure cable leakage levels below this, since the noise floor for this test setup was roughly 45 dB below the AUT pattern's peak. Therefore, this error term appears to be dominated by the low SNR when performing the isoflux measurements.

## 4.18 ERROR TERM #18: RANDOM ERRORS AND REPEATABILITY

### 4.18.1 Standard Gain Horn

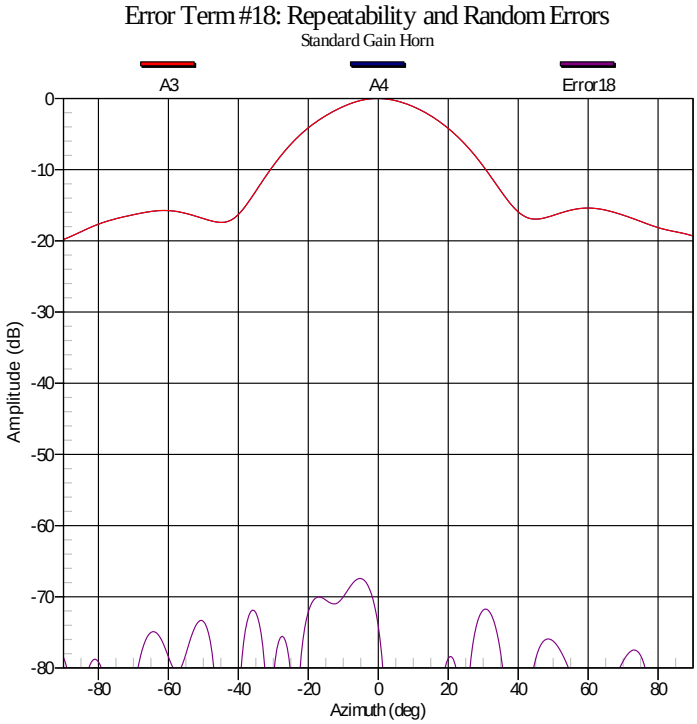


**Figure 4-59: Evaluation of Error Term #18 for the Standard Gain Horn**

### 4.18.2 Microstrip Patch

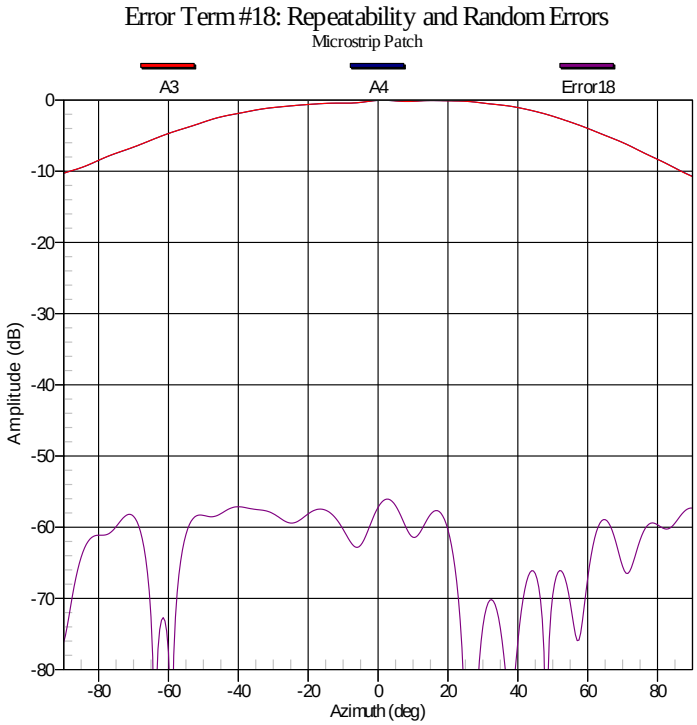


**Figure 4-60: Evaluation of Error Term #18 for the Microstrip Patch**

### 4.18.3 Slotted Waveguide Array

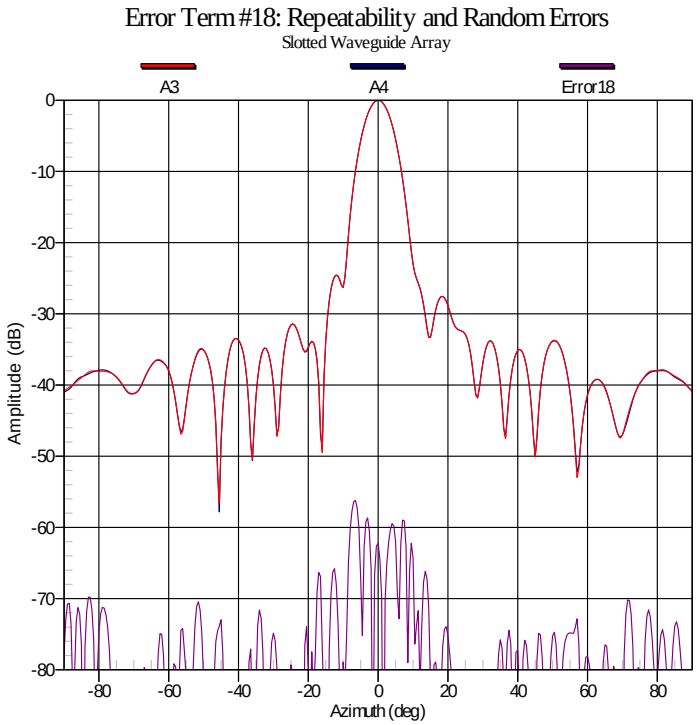


**Figure 4-61: Evaluation of Error Term #18 for the Slotted Waveguide Array**

### 4.18.4 Isoflux Horn

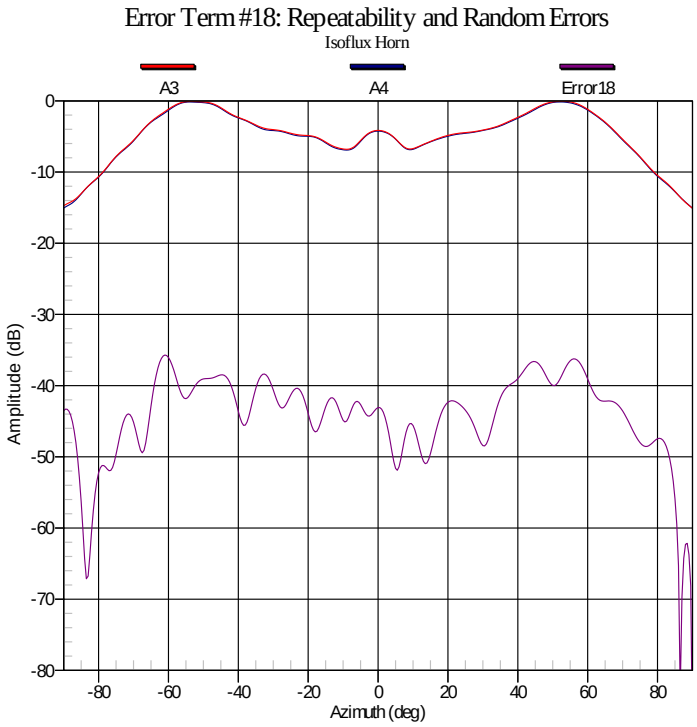


**Figure 4-62: Evaluation of Error Term #18 for the Isoflux Horn**

### 4.18.5 Discussion of Error Term #18

In Section 2.5.18 a simple method was proposed to determine the uncertainty due to the SNF system's repeatability and susceptibility to random errors. By comparing the far-field patterns computed using two identical measurements acquired one immediately after the other, a measure of the system's repeatability can be determined.

Figure 4-59 shows the resulting error signal level determined using the method described above for the standard gain horn. With an error signal level more than 65 dB below the AUT pattern peak, this system repeatability is quite good and will not have a noticeable impact on the resulting far-field pattern. Figures 4-60 and 4-61 confirm that this error term will also not be of concern for the microstrip patch and slotted waveguide array.

Lastly, Figure 4-62 shows the error signal level due to error term #18 for the isoflux antenna. Similar to the analysis of error term #17 for this antenna, one may immediately assume that the system repeatability is poor for this setup. However, this high error level

may once again be due to the isoflux antenna's limited signal-to-noise ratio. Therefore, this error term appears to be dominated by the low SNR when performing the isoflux measurements.

## 4.19 ACCUMULATED ERROR BUDGETS

At this point, individual error term analysis for all error terms has been presented for the four antennas outlined in Section 3.6. Once all automated measurements have been completed as outlined in the flow chart of Figure 3-1, the error assessment operator uses the interface shown in Figure 3-2 to select how he/she wishes to visualize the uncertainty associated with a particular antenna's radiation pattern.

In Section 4.19.1, the reader will find pattern cuts showing upper and lower bounds due to total uncertainty. These plots are automatically generated for the operator once the automated error assessment process is complete.

Next, in Section 4.19.2, the reader is presented with tabulated budgets outlining the contribution of the eighteen error terms to the total uncertainty. Once again, this type of budget is automatically generated by the error assessment procedure once all error terms have been evaluated. While gain/pattern peak budgets are generated by the software automatically, the user also has the option to output tabulated uncertainty budgets for sidelobes, as will be seen.

Full sphere uncertainty data such as those found in Section 4.19.3 can also be generated.

### 4.19.1 Pattern Cuts Showing Upper and Lower Bounds due to Total Uncertainty

In this section, un-normalized $\phi = 0^{\circ}$ azimuth-cuts of the quoted AUT radiation pattern (red curves) are shown for all four antennas used to test the assessment process. To provide a measure of uncertainty in these quoted AUT radiation patterns, the upper and lower bounds of $A_1$ due to the total computed uncertainty are shown as dashed lines (blue and purple, respectively). These plots are generated automatically by the automated error assessment procedure. In order to compute these upper/lower bounds due to total amplitude uncertainty, the total uncertainty computed using (3.2-8) at each $(\theta, \phi)$ position is added/subtracted to/from the far-field radiaiton pattern amplitude at the same $(\theta, \phi)$ position. While measurement errors do not typically have equal weight in the upper and lower bounds, it was assumed that these two uncertainties were equal for this thesis to reduce computational complexity and processing time. Many of the error terms would also need additional measurements to make the distinction between the upper and lower amplitude uncertainty values.

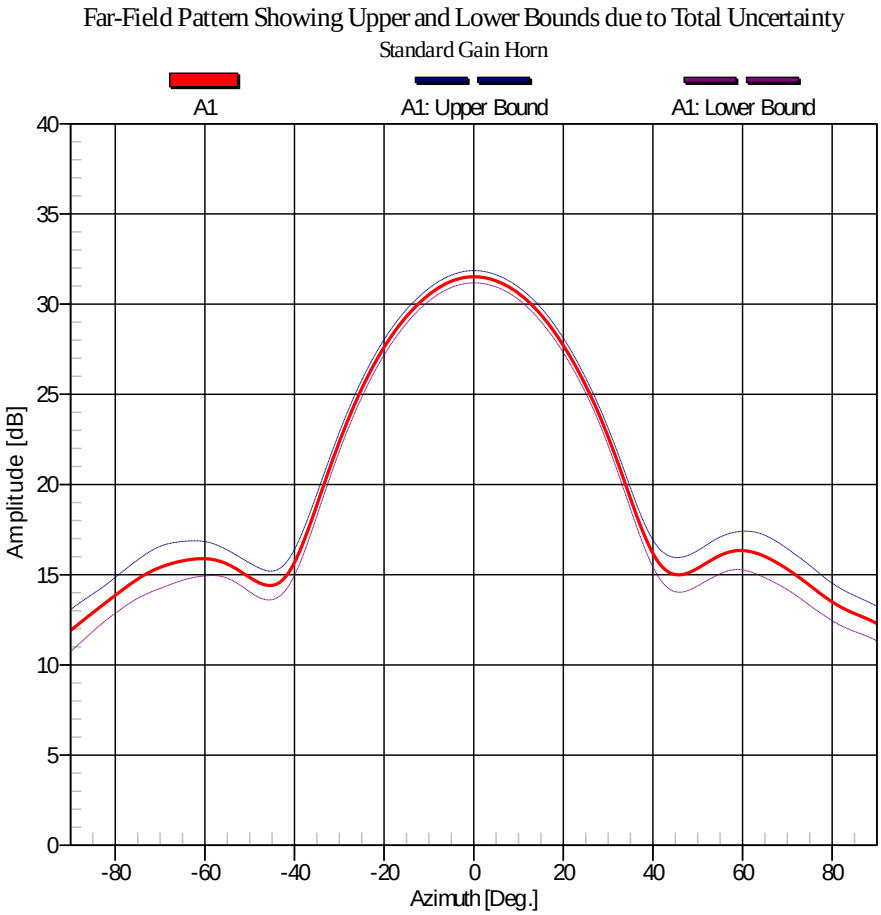


**Figure 4-63: Quoted Far-Field Radiation Pattern for the Standard Gain Horn (——) Showing Upper (— —) and Lower (— —) Bounds due to Total Uncertainty**

Figure 4-63 above shows the pattern cut described above for the standard gain horn, as it was generated by the software. This plot shows that the uncertainty in the region of the AUT's main beam is reasonable and tends to increase as the far-field pattern amplitude decreases.

Next, Figure 4-64 shows the same information as it was generated by the software for the slotted waveguide array. Notice that this plot only shows an azimuth span of 70˚, rather than the usual 180˚ span used for plotting. Since the slotted waveguide array has a high directivity, the amplitude outside of the region shown in Figure 4-64 drops off very quickly. As the pattern amplitude approaches the noise floor, the idea of determining amplitude uncertainty loses its meaning. For this reason, the computed uncertainty in these regions may be very large, but determining the accuracy of measured amplitudes at

such low power levels is nearly impossible and in fact of little use. Again, this plot provides an excellent depiction the pattern uncertainty for this particular antenna.

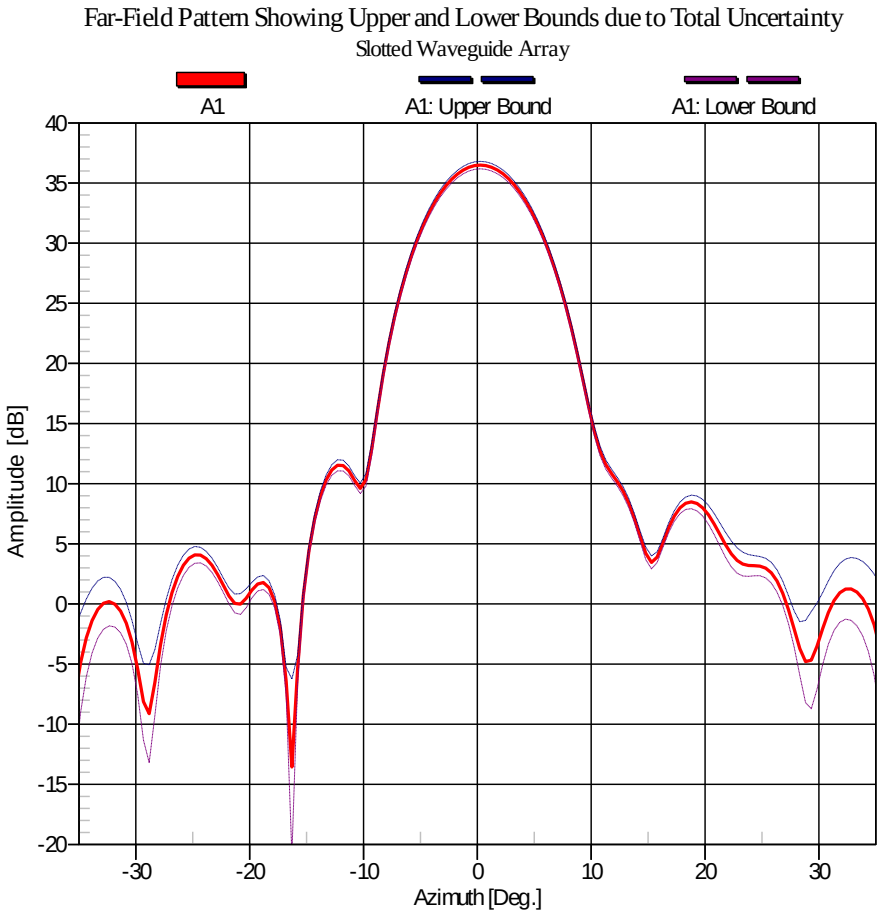


**Figure 4-64: Quoted Far-Field Radiation Pattern for the Slotted Waveguide Array (——) showing Upper (— —) and Lower (— —) Bounds due to Total Uncertainty**

Figure 4-65 presents the same type of data generated for the microstrip patch. One immediately sees that the upper and lower bounds due to total uncertainty for this antenna deviate greatly from the quoted AUT radiation pattern. However, since the purpose of this thesis is to simply identify and quantify the contributions of the various error terms, this data can be very useful. If an operator were to obtain such a result for an antenna, the error assessment process under discussion would be used to identify the dominant error contributions, and steps should be taken to correct for some of the most significant sources of error. If these steps are chamber related, the antenna would be retested and the

error assessment redone prior to providing results to a client (with smaller uncertainty). If the steps taken involve post-processing of the acquired data to correct for certain chamber imperfections, the procedure described in the next paragraph would be used.

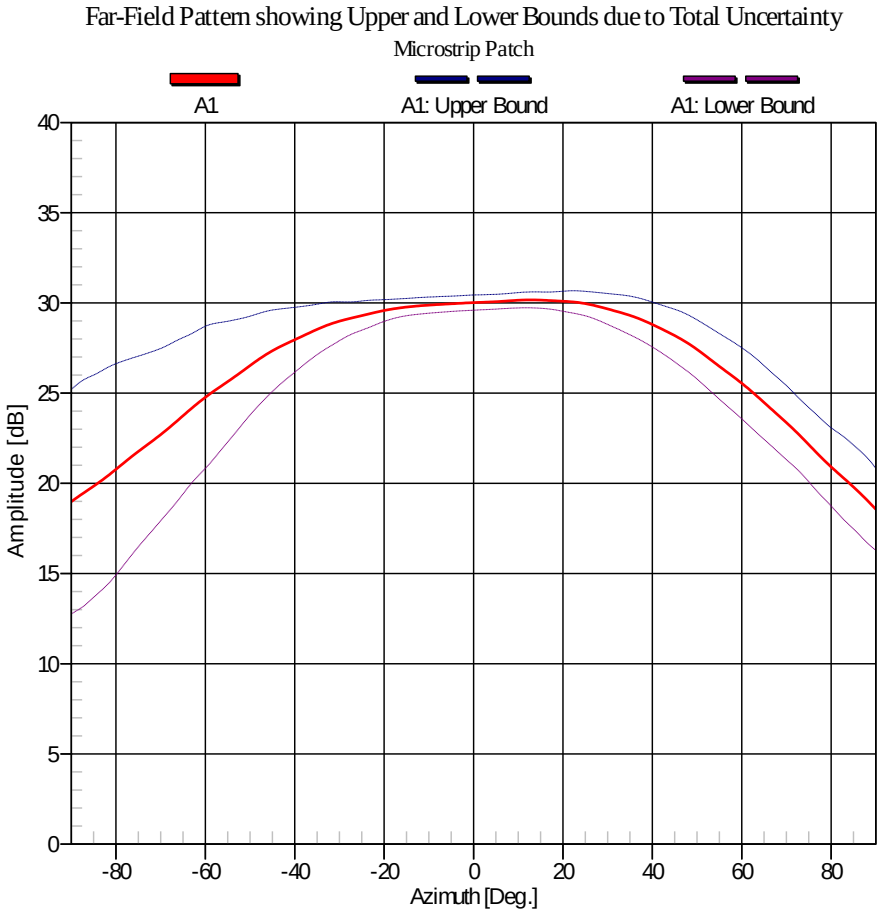


**Figure 4-65: Quoted Far-Field Radiation Pattern for the Microstrip Patch (——) showing Upper (— —) and Lower (— —) Bounds due to Total Uncertainty**

In Figure 4-66, the uncertainty data is once again shown for the microstrip patch. However, some corrections and compensations have been done on the quoted AUT radiation pattern prior to performing the 18-term error assessment analysis this time. Namely, the reflection suppression algorithm discussed in [2] has been applied to dataset $A_1$ to minimize the effects of room scattering. Additionally, the radiation pattern was compensated to remove the effects of error term #11. If this type of compensated data is used as the quoted radiation pattern, the uncertainty budget would be updated to reflect this. When quoting uncertainty information for this antenna, one must now assume there

are no errors due to room scattering or $\theta / \phi$-axis non-intersection, since the compensation process itself would have used the assessed uncertainty term as part of its post-processing algorithm. Nevertheless, compensated plots showing upper and lower bounds such as this are extremely valuable.

Figure 4-67 shows the same type of uncertainty information as it was computed for the isoflux horn without compensation for any error terms. Since the effects of error term #11 were so severe for this antenna, as explained throughout this chapter, one would expect the resulting overall uncertainty to also be severe. While the general trend of the upper and lower bounds do not provide any actual insight into the specific uncertainty values for this antenna, the error assessment operator would immediately realize that there are some chamber-related problems that should be accounted for. By viewing individual error term results using the software presented in Section 3.6, one can determine which sources of error are of greatest concern. By compensating for the effects of error terms #11 and #16, the results of Figure 4-68 were obtained. If correcting for known chamber-related errors is not a possibility, one should use compensated data when using this error assessment software.

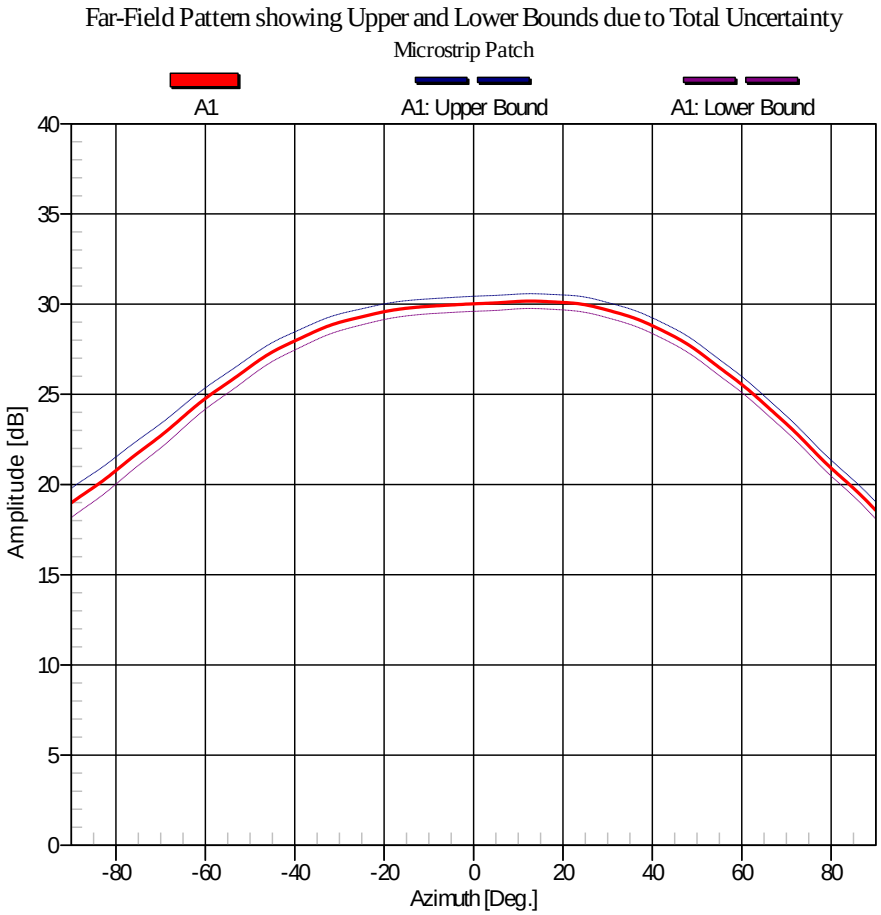


**Figure 4-66: Quoted Far-Field Radiation Pattern for the Microstrip Patch (——) showing Upper (– –) and Lower (– –) Bounds due to Total Uncertainty after Compensating for Various Error Terms**

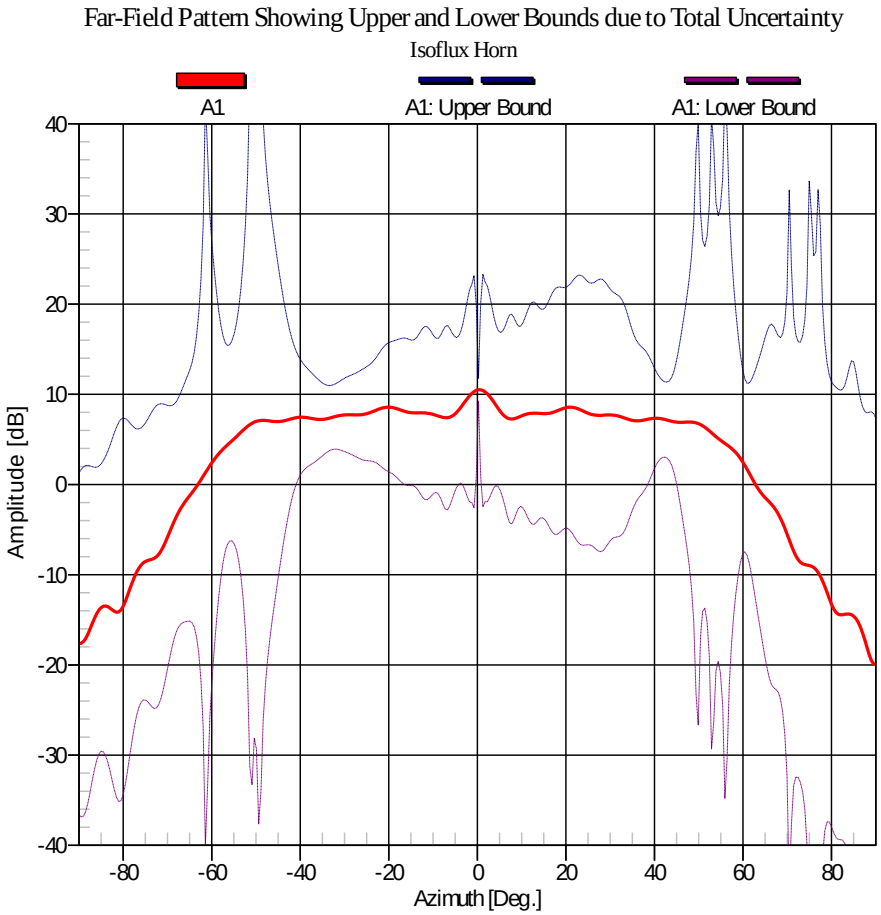


**Figure 4-67: Quoted Far-Field Radiation Pattern for the Isoflux Horn (——) showing Upper (– –) and Lower (– –) Bounds due to Total Uncertainty**

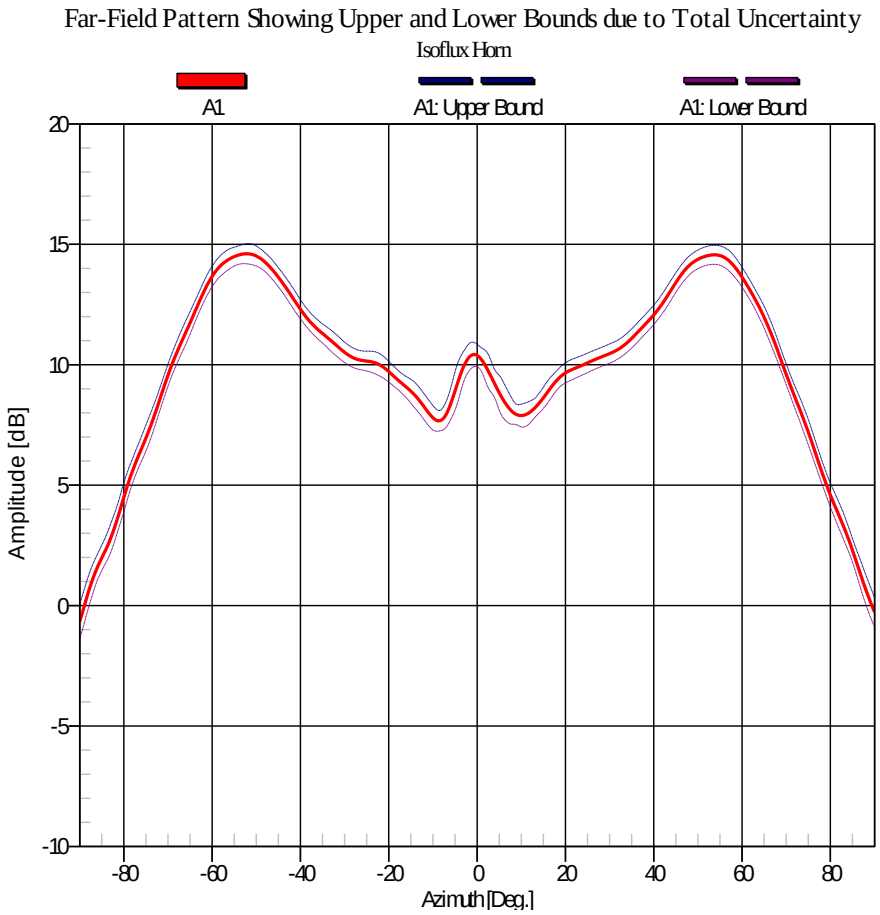


**Figure 4-68: Quoted Far-Field Radiation Pattern for the Isoflux Horn (——) showing Upper (— —) and Lower (— —) Bounds due to Total Uncertainty after Compensating for Various Error Terms**

### 4.19.2 Tabulated 18-Term Error Assessment Budgets

In this section, the reader is presented with a variety of tabulated uncertainty budgets for all four antennas used to test this automated error assessment procedure. This is the format most typically used to present error assessment details for a particular antenna. The tables are included simply to indicate the format of the automatically generated data provided from the software written for this thesis research.

Table 4-5 shows the tabulated 18-term uncertainty budget for the standard gain horn's pattern peak (directivity) and gain. First, a "pattern peak total uncertainty" is computed by excluding error terms #3, #5 and #6 since they apply to gain measurements only. Next, a "gain total uncertainty" is computed using all of the terms. Tables 4-6, 4-7 and 4-8 show the same type of tabulated budgets for the microstrip patch, slotted waveguide array and isoflux horn, respectively. Finally, Table 4-9 shows a similar tabulated budget for a -15 dB sidelobe for the standard gain horn antenna. Recall that the error terms specific to gain measurements are excluded from this budget.

**Table 4-5: Pattern Peak and Gain Uncertainty Budget for the Standard Gain Horn**

| Pattern Peak/Gain Budget Error Term | Uncertainty |
|---|---|
| 1. Probe Relative Pattern: | 0.00 dB |
| 2. Probe Polarization (p' = 20 dB): | 0.00 dB |
| 4. Probe Alignment: | N/A |
| 7. AUT Alignment: | N/A |
| 8. Data Point Spacing: | 0.02 dB |
| 9. Data Truncation: | N/A |
| 10. Sphere Radius Errors (10 cm radial uncertainty in measurement sphere): | 0.00 dB |
| 11. Sphere Theta/Phi Errors: | 0.00 dB |
| 12. Higher Order Coupling | 0.11 dB |
| 13. Receiver Amplitude Non-Linearity: | 0.00 dB |
| 14. System Phase Errors: | 0.08 dB |
| 15. Receiver Dynamic Range: | 0.00 dB |
| 16. Room Scattering (Possibility #3): | 0.01 dB |
| 17. Cable Leakage: | 0.00 dB |
| 18. Repeatability and Random Errors: | 0.00 dB |
| **Pattern Peak Uncertainty (RSS):** | **0.14 dB** |
| 3. Calibrated Probe Gain: | 0.15 dB |
| 5. Normalization Constant | 0.03 dB |
| 6. AUT/SGH Impedance Mismatch | 0.06 dB |
| **Gain Total Uncertainty (RSS):** | **0.22 dB** |

**Table 4-6: Pattern Peak and Gain Uncertainty Budget for the Microstrip Patch**

| Pattern Peak/Gain Budget Error Term | Uncertainty |
|---|---|
| 1. Probe Relative Pattern: | 0.00 dB |
| 2. Probe Polarization (p' = 20 dB): | 0.13 dB |
| 4. Probe Alignment: | N/A |
| 7. AUT Alignment: | N/A |
| 8. Data Point Spacing: | 0.03 dB |
| 9. Data Truncation: | N/A |
| 10. Sphere Radius Errors (10 cm radial uncertainty in measurement sphere): | 0.00 dB |
| 11. Sphere Theta/Phi Errors: | 0.00 dB |
| 12. Higher Order Coupling | 0.05 dB |
| 13. Receiver Amplitude Non-Linearity: | 0.00 dB |
| 14. System Phase Errors: | 0.27 dB |
| 15. Receiver Dynamic Range: | 0.01 dB |
| 16. Room Scattering (Possibility #3): | 0.02 dB |
| 17. Cable Leakage: | 0.00 dB |
| 18. Repeatability and Random Errors: | 0.01 dB |
| **Pattern Peak Uncertainty (RSS):** | **0.31 dB** |
| 3. Calibrated Probe Gain: | 0.15 dB |
| 5. Normalization Constant | 0.07 dB |
| 6. AUT/SGH Impedance Mismatch | 0.06 dB |
| **Gain Total Uncertainty (RSS):** | **0.36 dB** |

**Table 4-7: Pattern Peak and Gain Uncertainty Budget for the Slotted Waveguide Array**

| Pattern Peak/Gain Budget Error Term | Uncertainty |
|---|---|
| 1. Probe Relative Pattern: | 0.00 dB |
| 2. Probe Polarization (p' = 20 dB): | 0.00 dB |
| 4. Probe Alignment: | N/A |
| 7. AUT Alignment: | N/A |
| 8. Data Point Spacing: | 0.02 dB |
| 9. Data Truncation: | N/A |
| 10. Sphere Radius Errors (10 cm radial uncertainty in measurement sphere): | 0.00 dB |
| 11. Sphere Theta/Phi Errors: | 0.01 dB |
| 12. Higher Order Coupling | 0.03 dB |
| 13. Receiver Amplitude Non-Linearity: | 0.00 dB |
| 14. System Phase Errors: | 0.03 dB |
| 15. Receiver Dynamic Range: | 0.00 dB |
| 16. Room Scattering (Possibility #3): | 0.01 dB |
| 17. Cable Leakage: | 0.00 dB |
| 18. Repeatability and Random Errors: | 0.00 dB |
| **Pattern Peak Uncertainty (RSS):** | **0.05 dB** |
| 3. Calibrated Probe Gain: | 0.15 dB |
| 5. Normalization Constant | 0.16 dB |
| 6. AUT/SGH Impedance Mismatch | 0.06 dB |
| **Gain Total Uncertainty (RSS):** | **0.23 dB** |

**Table 4-8: Pattern Peak and Gain Uncertainty Budget for the Isoflux Horn**

| Pattern Peak/Gain Budget Error Term | Uncertainty |
|---|---|
| 1. Probe Relative Pattern: | 0.00 dB |
| 2. Probe Polarization (p' = 20 dB): | 0.05 dB |
| 4. Probe Alignment: | N/A |
| 7. AUT Alignment: | N/A |
| 8. Data Point Spacing: | 0.03 dB |
| 9. Data Truncation: | N/A |
| 10. Sphere Radius Errors (10 cm radial uncertainty in measurement sphere): | 0.00 dB |
| 11. Sphere Theta/Phi Errors: | 0.22 dB |
| 12. Higher Order Coupling | 0.11 dB |
| 13. Receiver Amplitude Non-Linearity: | 0.00 dB |
| 14. System Phase Errors: | 0.20 dB |
| 15. Receiver Dynamic Range: | 0.05 dB |
| 16. Room Scattering (Possibility #3): | 0.00 dB |
| 17. Cable Leakage: | 0.02 dB |
| 18. Repeatability and Random Errors: | 0.06 dB |
| **Pattern Peak Uncertainty (RSS):** | **0.33 dB** |
| 3. Calibrated Probe Gain: | 0.15 dB |
| 5. Normalization Constant | 0.05 dB |
| 6. AUT/SGH Impedance Mismatch | 0.06 dB |
| **Gain Total Uncertainty (RSS):** | **0.37 dB** |

**Table 4-9: Pattern Sidelobe Uncertainty Budget for the Standard Gain Horn**

| Pattern Sidelobe Uncertainty Budget at (theta,phi) = (60,0) [15 dB SLL] | Uncertainty |
|---|---|
| 1. Probe Relative Pattern: | 0.00 dB |
| 2. Probe Polarization (p' = 20 dB): | 0.02 dB |
| 4. Probe Alignment: | N/A |
| 7. AUT Alignment: | N/A |
| 8. Data Point Spacing: | 0.16 dB |
| 9. Data Truncation: | N/A |
| 10. Sphere Radius Errors (10 cm radial uncertainty in measurement sphere): | 0.01 dB |
| 11. Sphere Theta/Phi Errors: | 0.40 dB |
| 12. Higher Order Coupling | 0.40 dB |
| 13. Receiver Amplitude Non-Linearity: | 0.00 dB |
| 14. System Phase Errors: | 0.08 dB |
| 15. Receiver Dynamic Range: | 0.00 dB |
| 16. Room Scattering (Possibility #3): | 0.64 dB |
| 17. Cable Leakage: | 0.00 dB |
| 18. Repeatability and Random Errors: | 0.05 dB |
| **Pattern Sidelobe Uncertainty (RSS):** | **0.87 dB** |

### 4.19.3 Full Sphere Uncertainty Data

Finally, using the software described in Section 3.6, the error assessment operator may output full sphere uncertainty data. Figure 4-69 shows the normalized amplitude of $A_1$ for the standard gain horn. Figure 4-70 was generated using full sphere uncertainty data for this antenna. In the region of the main beam and first sidelobes of the SGH's radiation pattern, one sees in Figure 4-70 that the uncertainty is reasonable. However, as the SGH's amplitude decays away from the main beam, the associated uncertainty rises. Since the amplitude outside of the SGH's main beam and sidelobe region is sufficiently low, however, one should expect to see high values of amplitude uncertainty. For this reason, one may simply wish to view this data for the main beam only, where amplitude uncertainty results have greater meaning.

The normalized amplitude of the SGH's main beam can be seen in Figure 4-71, while the associated amplitude uncertainty in this region is visualized in Figure 4-72. Figures 4-73 and 4-74 show the same type of data as discussed above for the microstrip patch antenna.

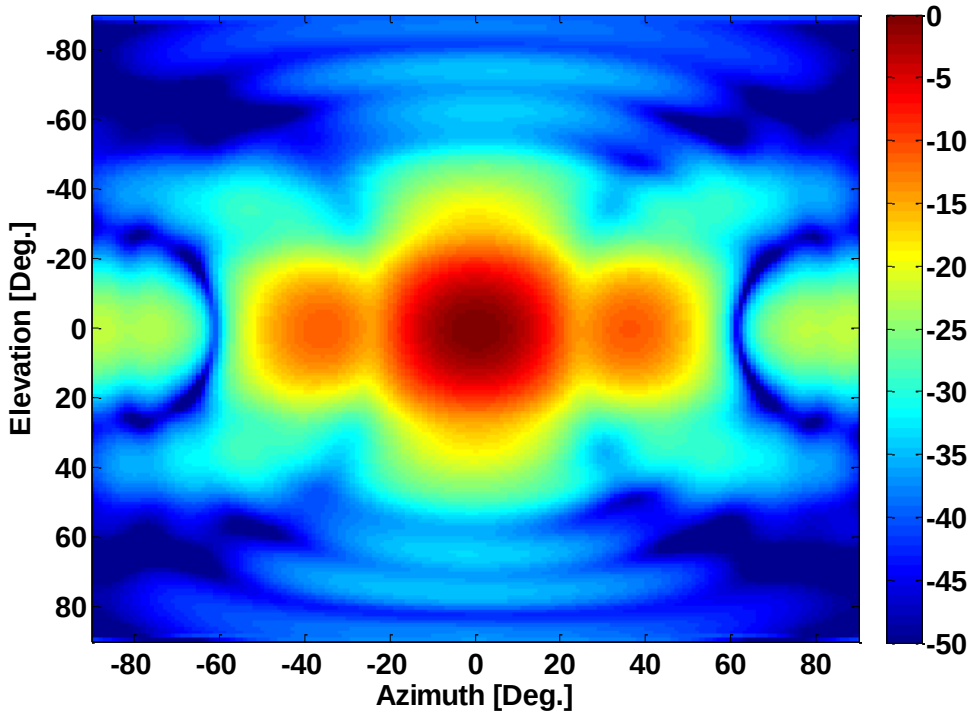


**Figure 4-69: Normalized Far-Field Amplitude, $A_1$, of the Standard Gain Horn in dB**

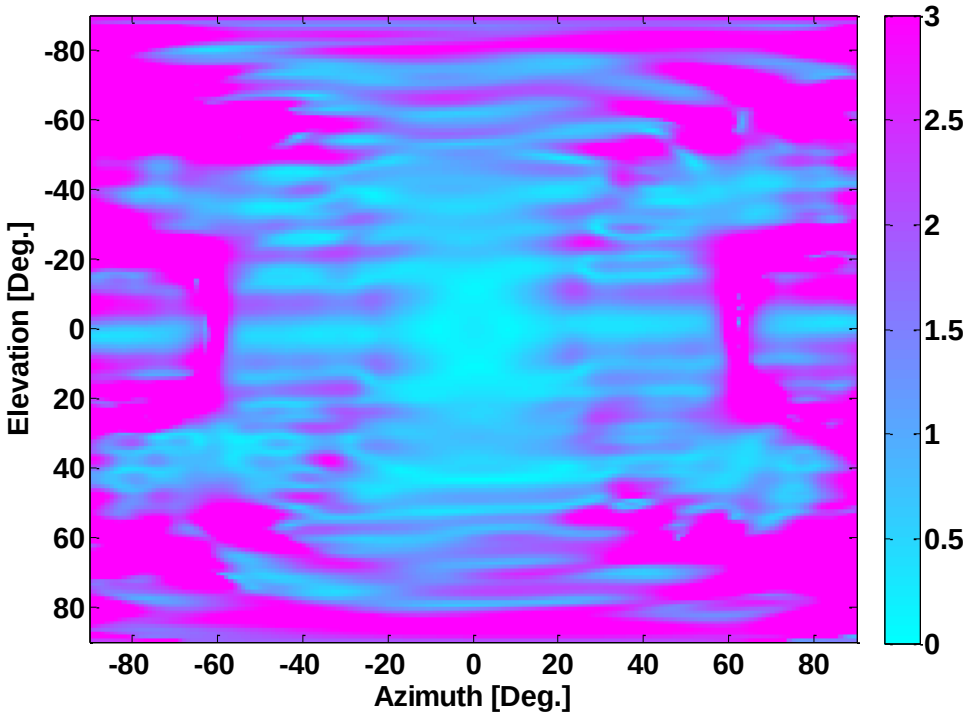


**Figure 4-70: Far-Field Amplitude Uncertainty, $U_{total,}$ for the Standard Gain Horn in dB**

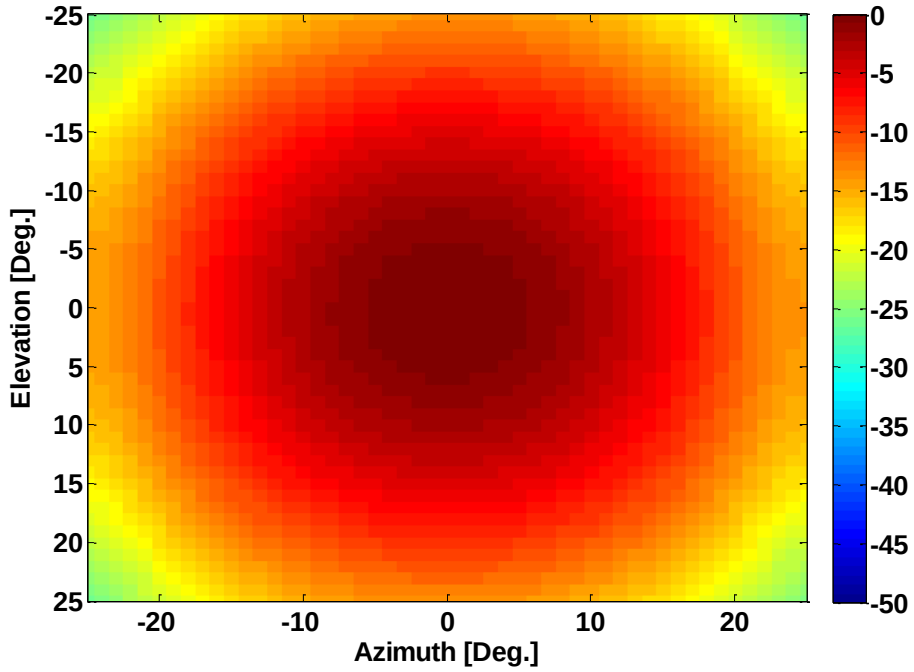


**Figure 4-71: Normalized Far-Field Amplitude, $A_1$, of the Standard Gain Horn in dB Showing Only the Main Beam**

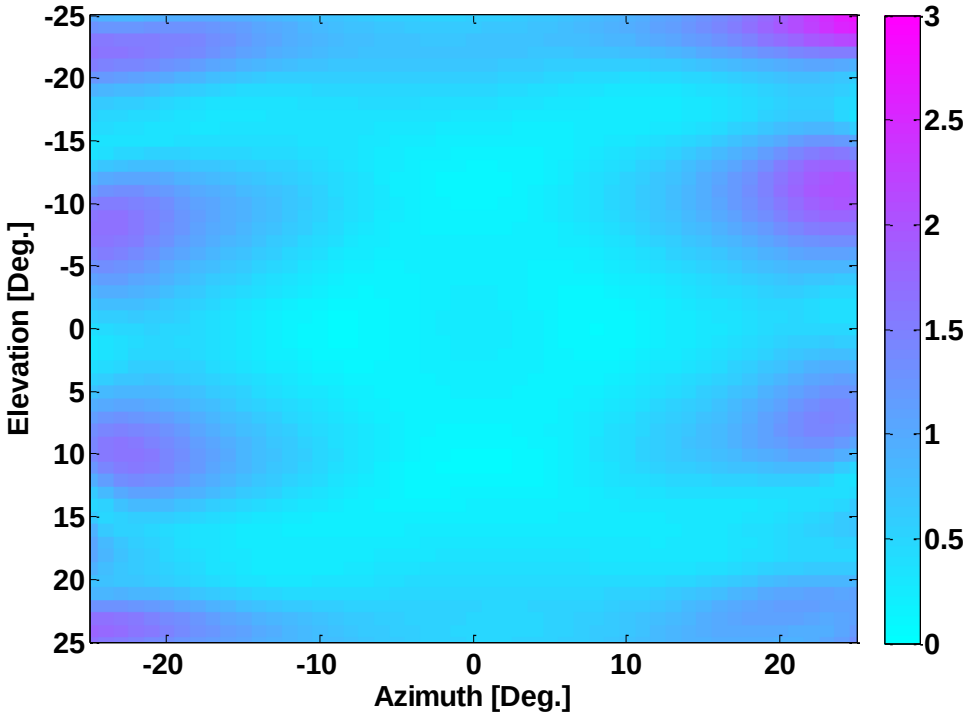


**Figure 4-72: Far-Field Amplitude Uncertainty, $U_{total,}$ for the Standard Gain Horn in dB Showing Only the Uncertainty in the Main Beam Region**

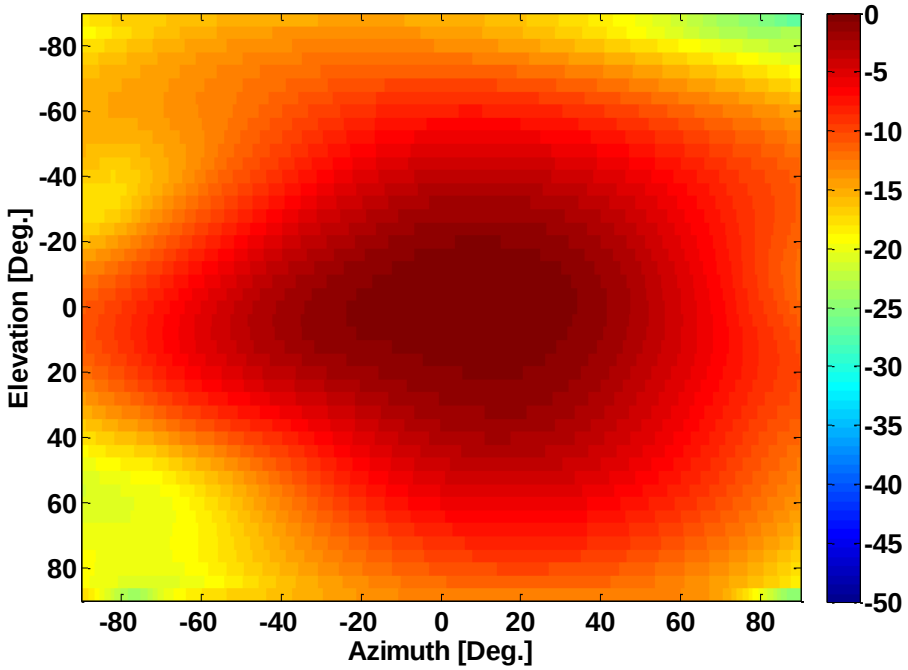


**Figure 4-73: Normalized Far-Field Amplitude, $A_1$, of the Microstrip Patch in dB**

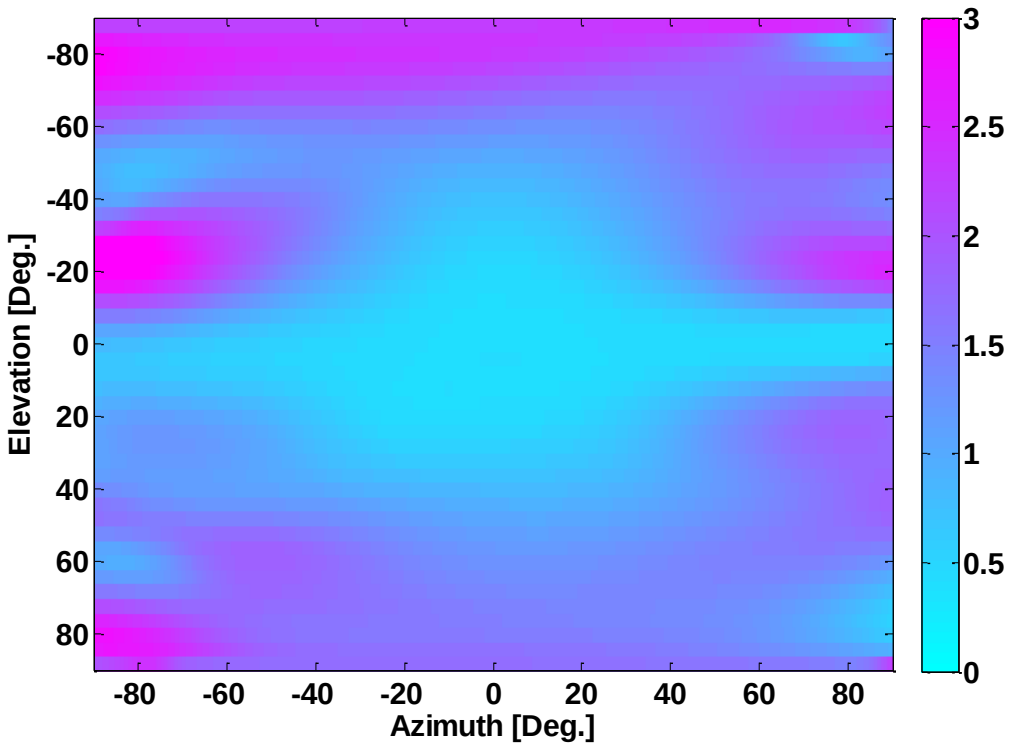


**Figure 4-74: Far-Field Amplitude Uncertainty, $U_{total,}$ for the Microstrip Patch in dB**

## 4.20 CONCLUDING REMARKS

In this chapter the automated error assessment process developed in previous chapters has been exercised on four selected antennas. The outcomes of these assessments, obtained using software-controlled implementation of the assessment process, have been discussed and interpreted.

## 4.21 REFERENCES FOR CHAPTER 4

1. A.D.Olver, P.J.B.Clarricoats, A.A.Kishk & L.Shafai, Microwave Horns and Feeds (IEE Series, 1994).

2. G. Hindman, A. Newell, "Mathematical Absorber Reflection Suppression (MARS) for Anechoic Chamber Evaluation and Improvement", Proc. Antenna Measurement Techniques Association (AMTA) Annual Symp., 2008. *(CD-Rom)*

# CHAPTER 5 : General Conclusions

The goal of this thesis was to develop a new measurement process that will permit an assessment of SNF measurement errors based on a set of practical tests that can be done on a routine basis as part of any SNF measurement. The assessment was to provide reasonable engineering estimates of the error in the quantities being measured, the purpose being to achieve a test system that would, in an automated fashion, derive error bars for measured radiation patterns. This has been achieved through the research conducted for the thesis. The principal contributions of this thesis are therefore as follows:

- Some terms in an existing 18-term error budget developed for planar near-field measurements, and later partially adapted by others to spherical near-field measurements, were refined so as to apply more "naturally" to SNF testing.
- A new set of specific measurements has been identified that can be carried out automatically on both an AUT and the test set-up, and used to evaluate the uncertainty contributed by the above error terms. The order of the measurements has been structured (and presented in the form of a flow chart detailing what actions are required in an automated process) to minimize the overall time to complete an error assessment. This has been achieved by so defining the set of required measurements that several data sets can simply be extracted as subsets of these key measurements and so need not be separately acquired. The correct ordering of the specific measurements was especially important to permit resumption of data set acquisition should any single step prove to be temporarily problematic.
- The complete error assessment process has been automated. The software that has been developed for this purpose (with appropriate user interfaces) consists of two parts, namely that for performing the automated data acquisition to gather all the data needed for the uncertainty assessment, and that for the automated

processing of the measured data to arrive at the actual uncertainty estimates (and the tabular and graphical presentation thereof). A similar system has not been available in the open literature or commercially. The generation of uncertainty estimates at all points on the radiation sphere (that is, in all pattern directions) appears to have been done here for the first time.

Some of the lesser contributions, although still useful, are as follows:

- Much of the detailed material on error assessment in antenna measurements is either only accessible in fragmented form in the literature or as part of the knowledge possessed by individuals (and not written down anywhere). This thesis has collected this information, much of it through direct experience gained as part of the research or through private communications with many experienced individuals, in a single document. Such a fairly complete treatment, with a uniform set of definitions and unambiguous expressions for the computation of uncertainty-related quantities, should serve as a useful resource for both future research and antenna SNF measurement practice.
- Several of the terms in the 18-term error budget that were already extant at the start of the present research, and have been adopted as is in the work of this thesis, had not been explained anywhere in the literature. These have now all been interpreted in Chapters 2 and 3 of the thesis and some more careful terminology selected in some instances.
- The method can also serve as a useful tool for routine SNF antenna test chamber maintenance.